Smart Reflection and Passive Communication: Synergizing Backscatter Communication and 6G Technologies for Future Wireless Networks

Sahar Idrees

April, 2024

A thesis submitted for the degree of Doctor of Philosophy
of The Australian National University

Dedication

Dedicated to my dearest mother Manzoor Fatima
and
my loving husband Saad
Everything I have accomplished in life is a testament to their unconditional love, unwavering support and constant prayers.

Declaration

The contents of this thesis are the results of original research and have not been submitted for a higher degree to any other university or institution.

The work in this thesis has been published or has been submitted for publication as journal papers or conference proceedings.

The research work presented in this thesis has been performed jointly with Prof. Salman Durrani (The Australian National University), Assoc. Prof. Xiangyun Zhou (The Australian National University), Prof. Dusit Niyato (Nanyang Technological University, Singapore), Dr. Xiaolun Jia (The Australian National University), Dr. Zhiwei Xu (The Australian National University) and Saud Khan (The Australian National University).

The substantial majority of this work is my own.

Sahar Idrees
Research School of Engineering,
College of Engineering, Computer Science and Cybernetics,
The Australian National University, Canberra, ACT 2601, AUSTRALIA.

Acknowledgments

First and foremost, all praise and gratitude to Allah Almighty, who has consistently provided me with guidance, patience, and the resilience to persevere. Furthermore, the completion of this work would have remained beyond reach without the unwavering support of numerous individuals. I wish to express my deepest appreciation and acknowledge each and every one of them for their invaluable contributions.

- I would like to extend my sincere and heartfelt gratitude to my supervisors and mentors Drs. Salman Durrani and Xiangyun Zhou for their unwavering guidance, support, and encouragement throughout my doctoral studies. Their mentorship has been instrumental in my academic journey, providing me with the freedom and flexibility to explore innovative ideas and new research avenues. Whenever I sought their counsel, they readily engaged in in-depth discussions, nurturing my enthusiasm for the work and helping me refine my research focus. Their meticulous review of my publication drafts and their guidance in honing various academic research skills have been invaluable. Furthermore, beyond the realm of research, they have been pillars of support, aiding me in acquiring teaching and supervision experience. Their assistance and guidance have extended to all aspects of my academic and personal development. I would also like to thank Prof. Parastoo Sadeghi for being on my supervisory panel and Assoc. Prof. Nan Yang for providing me tutorship opportunities.

- I would also like to thank my research collaborator, Prof. Dusit Niyato of Nanyang Technological University, Singapore for providing timely and insightful feedback on my first work.

- Special thanks to my collaborators and friends Drs. Xiaolun Jia and Zhiwei Xu for their valuable feedback and support in solving some critical issues in my research.

- It has been a rewarding experience to be a part of the Communication Research Group at the Research School of Engineering, College of Engineering, Computer

Science and Cybernetics. I would like to extend my gratitude to all the members of our research group for fostering a warm and conducive research atmosphere. I would also like to express my special appreciation to the dedicated administrative staff of the school for their support and assistance.

- I would also like to thank my professors and colleagues Drs. Asim Loan, K. M. Hasan and Muhammad Tahir at the department of Electrical Engineering, University of Engineering and Technology, Lahore, Pakistan and Dr. Muhammad Usman from CSIRO for inspiring and encouraging me to pursue PhD studies.

- Last but not the least, I am gratitude personified for my mother Manzoor Fatima, who inculcated the love of learning and hard work in me and whose constant encouragement and prayers have been the driving force behind my journey. Finally, I express immense appreciation for the love of my life, my husband Saad and our two beloved children Ahmed and Abdullah. Their unwavering support, love, encouragement, patience, and understanding have consistently motivated me to strive for excellence and push through the challenges of doctoral studies.

Abstract

Backscatter Communication (BackCom) has been envisioned as a key enabler for ubiquitous connectivity in the Internet of Things (IoT). It achieves this by passively modulating and reusing existing radio-frequency signals. To become a pivotal technology within the IoT framework, BackCom faces various challenges including limited coverage, inflexibility in deployment, low data rates, etc. This thesis is dedicated to tackling the inherent issues within BackCom. It does so by delving into a series of system configurations that expand the boundaries in terms of increased range and improved bit error rate (BER). Furthermore, it future-proofs BackCom by investigating how it can synergize with other emerging technologies like intelligent reflecting surfaces (IRS), wireless power transfer (WPT) and machine learning.

In the first system configuration which we present in chapter 2, we consider WPT from an energy transmitter (ET) employing retrodirective WPT using a large phased antenna array to an energy receiver (ER) capable of ambient backscatter. The advantage of retrodirective WPT is that no explicit channel estimation is needed at the ET and the use of ambient backscattering eliminates the need for active transmission at the ER. We propose a training sequence design, i.e., pattern of varying the reflection coefficient at the ER, to eliminate the direct-link interference from the ambient source. We show that when the ambient symbol duration is known, the ambient interference is fully cancelled by the proposed design. We analytically model the system and find the average harvested power at the ER considering Nakagami-m fading channels and non-linear energy harvesting model. Our results clearly show that the proposed solution is robust to a small timing offset mismatch at the correlator. When interference from undesired neighboring sources in the ambient environment is not significant, the ER can successfully harvest tens to hundreds of micro-watts of power, which is an important improvement for low-power IoT devices.

In chapter 3, we address a key issue in ambient BackCom viz. the weakness of backscatter signal in the presence of strong direct-link interference from the original RF source. This limits the bit error rate (BER) and hence the transmission rate and range

of ambient BackCom systems. Meanwhile, the IRS offers new degrees of freedom in enhancing a variety of systems by transforming their propagation media and signals. In this work, we devise a novel scheme to improve the detection performance of an ambient BackCom system using an IRS located in its proximity. The IRS augments the backscatter signal quality at the receiver by adjusting its phase shifts to balance signal strengths, ultimately improving the performance of energy detection at the receiver. Our results clearly show that an IRS of reasonable size can considerably improve the BER performance of ambient backscatter, which is an important improvement for low power IoT systems.

In chapter 4, we address the issue of limited range in monostatic BackCom systems by considering such a system assisted by an IRS and controlled seamlessly by data driven deep learning (DL) based approach. We propose a deep residual convolutional neural network (DRCNN) named *BackIRS-Net* that exploits the unique coupling between the IRS phase shifts and the beamforming at the reader, to jointly optimize these quantities in order to maximize the effective signal to noise ratio (SNR) of the backscatter signal received at the reader. We show that the performance of a trained BackIRS-Net is close to the conventional optimization based approach while requiring much less computational complexity and time, which indicates the utility of this scheme for real-time deployment. Our results show that an IRS of moderate size can significantly improve backscatter SNR, resulting in range extension by a factor of 4 for monostatic BackCom, which is an important improvement in the context of BackCom based IoT systems.

Contents

List of Publications

The work in this thesis has been published or has been submitted for publication as journal papers or conference proceedings. These papers are:

Journal Papers

J1. S. Idrees, X. Zhou, S. Durrani and D. Niyato, "Design of Ambient Backscatter Training for Wireless Power Transfer," in *IEEE Trans. Wireless Commun.*, vol. 19, no. 10, pp. 6316-6330, Oct. 2020.

J2. S. Idrees, X. Jia, S. Durrani and X. Zhou, "Design of Intelligent Reflecting Surface (IRS)-Boosted Ambient Backscatter Systems," in *IEEE Access*, vol. 10, pp. 65000-65010, 2022.

J3. S. Idrees, S. Durrani, Z.Xu, X. Jia, and X. Zhou, "Joint Active and Passive Beamforming for IRS-assisted Monostatic Backscatter Systems: An Unsupervised Learning Approach," in *IEEE Trans. Mach. Learn. Commun. Netw.*, Jan 2024.

Conference Papers

C1. S. Idrees, X. Zhou, S. Durrani and D. Niyato, "A Retrodirective Wireless Power Transfer Scheme for Ambient Backscatter Systems," in *Proc. IEEE Int. Conf. Commun. (ICC)*, Dublin, Ireland, 2020, pp. 1-6.

The following papers are also produced during my PhD study but not explicitly used in this thesis:

Conference Papers

C2. S. Idrees, X. Jia, S. Khan, S. Durrani and X. Zhou, "Deep Learning Based Passive Beamforming for IRS-Assisted Monostatic Backscatter Systems," in *Proc. IEEE Int. Conf. Acoustics, Speech and Sig. Process. (ICASSP)*, Singapore, 2022, pp. 8652–8656.

List of Acronyms

BackCom	Backscatter Communication
IoT	Internet of Things
WPT	Wireless Power Transfer
ER	Energy Receiver
ET	Energy Transmitter
RF	Radio Frequency
CSI	Channel State Information
MIMO	Multiple Input Multiple Output
BER	Bit error rate
DSSS	Direct Sequence Spread Spectrum
PN	Pseudo-Noise
IRS	Intelligent Reflecting Surface
BD	Backscatter Device
RX	Backscatter Receiver
ED	Energy Detector
DLI	Direct-link Interference
LOS	Line-of-sight
SINR	Signal-to-interference-noise ratio
UAV	Universal Aerial Vehicle
AO	Alternating Optimization
SDR	Semidefinite relaxation
MM	Minorization Maximization

ZFBF	Zero-forcing beamforming
EBF	Eigen-vector beamforming
GRCD	Generalized relative channel difference
ML	Machine Learning
DL	Deep Learning
DRL	Deep Reinforcement Learning
DRCNN	Deep Reinforcement Convolutional Neural Networks
SNR	Signal-to-noise ratio
RFID	Radio Frequency IDentification
MLP	Multi-layer Perceptron
ReLU	Rectified Linear Unit
RM	Residual Module
FC	Fully connected
MRT	Maximum Ratio Transmission
MRC	Maximum Ratio Combining

List of Notations

$\mathbb{R}$	Set of real numbers
$\mathbb{C}$	Set of complex numbers
$\mathbb{R}^n$, $\mathbb{C}^n$	Real and complex vector spaces of dimension n
$\mathbb{R}^{m\times n}$, $\mathbb{C}^{m\times n}$	Real and complex matrix spaces of dimension $m \times n$
j	Complex unit $\sqrt{-1}$
$*$	Complex Conjugate
$\lvert\cdot\rvert$	Absolute value
$\mathrm{Re}\{\cdot\}$	Real part of a complex number
$\mathrm{Im}\{\cdot\}$	Imaginary part of a complex number
$\mathbf{a}$	Vector quantity
$\mathbf{A}$	Matrix quantity
$\lVert\mathbf{a}\rVert$	Euclidean norm of vector a
$\mathbf{I}$	Identity matrix of variable size
$\mathbf{A}^T$	Transpose of matrix $\mathbf{A}$
$\mathbf{A}^H$	Hermitian of matrix $\mathbf{A}$
$\mathbf{A} \succeq 0$	Matrix $\mathbf{A}$ is positive semidefinite
$\mathrm{tr}(\mathbf{A})$	Trace of matrix $\mathbf{A}$
$\mathrm{rank}(\mathbf{A})$	Rank of matrix $\mathbf{A}$
$\mathbb{E}\{\cdot\}$	Expectation of a random variable
$\mathrm{Var}\{\cdot\}$	Variance of a random variable
$\Pr(\cdot)$	Probability of an event
$f_X(\cdot)$	Pdf of random variable X

$\mathcal{N}(\mu, \sigma^2)$	Gaussian random variable with mean μ and variance σ^2
$\mathcal{CN}(\mu, \sigma^2)$	Complex Gaussian random variable with mean μ and variance σ^2
∇	Gradient operator
$\text{diag}(\cdot)$	Diagonalisation operator
$O(\cdot)$	Big-O notation

List of Figures

List of Tables

Chapter 1

Introduction

The Internet of Things (IoT) is being vastly deployed, finding its applications in smart homes and cities, healthcare, agriculture, autonomous vehicles and fleet management [3]. This has led to the emergence of a large number of IoT devices that need to perform and stay connected. With the deployment of fifth generation (5G) cellular networks and active research on sixth-generation (6G) systems, the future envisions the ability to support an extensive user base concurrently, offering exceptionally high data rates and minimal latency across diverse scenarios. In parallel, there is a concerted effort to merge communication technologies with machines, not only to enhance industrial efficiency and automation but also to facilitate interactions with everyday devices, ultimately raising living standards.

The IoT framework not only facilitates communication between physical objects but also empowers them to sense their surroundings, perform computations, and establish connections or collaborations with other devices, thus endowing everyday objects with "smart" capabilities [4]. Anticipated IoT applications extend to industrial and healthcare settings, environmental monitoring, and disaster response situations. In these scenarios, where manual data collection proves highly inefficient, longer communication ranges, quality-of-service, and latency requirements come into play, further underscoring the growing relevance and importance of IoT.

IoT transmissions are typically characterized by their intermittent and short-packet nature. However, with the proliferation of IoT devices, significant challenges arise concerning the efficient management and maintenance of these individual devices. The physical layer challenges primarily revolve around device complexity, power consumption, and coverage. To establish seamless coverage and connectivity in specific geographic areas, such as metropolitan regions, 5G employs the strategy of deploying numerous small cells.

While massive Multiple-Input Multiple-Output (mMIMO) technology achieves notable energy efficiency, it's important to note that increasing the number of base stations (BSs) also escalates energy consumption, particularly in terms of computational power. Moreover, the global proliferation of billions of battery-powered devices and sensors joining the network poses formidable challenges in enhancing energy efficiency within communication networks. Therefore, adhering to stringent energy efficiency requirements remains a significant challenge in the era of Beyond 5G (B5G).

Looking ahead to 6G wireless networks, the anticipated objective is to achieve a connectivity density of 107 devices per square kilometer (107 devices/km^2) while realizing a substantial volumetric energy-spectral efficiency gain of 1000 times in terms of bits per second per Hertz per cubic meter per Joule ($bps/Hz/m^3/Joule$) [5]. Considering that the number of machine-type devices within IoT is growing rapidly, achieving satisfactory functionality in future IoT networks without excessive maintenance efforts calls for the exploration of new solutions. This exploration should focus on simplifying devices to reduce energy consumption while simultaneously preserving or enhancing their lifespan and coverage.

Naturally, all these developments have led to increased interest in communication technologies that keep energy consumption and radio frequency (RF) emissions in check. The existing technological landscape underscores the necessity for the widespread adoption of machine-type devices that operate with minimal power consumption and strike a balance between energy usage and communication range, with the aim of optimizing the cost-performance ratio. Backscatter communication (BackCom), an emerging wireless communication paradigm operating at microwatt power levels, is increasingly being recognized as a viable solution to achieve low power and green communications for future wireless networks. Unlike conventional machine-type devices that rely on active transmissions, BackCom enables passive communication using existing RF signals. It empowers devices to reduce their dependence on batteries while also partially mitigating upper-layer issues such as random access. In particular, BackCom devices or 'tags' communicate by reflecting existing RF signals, while modulating their own information upon the reflected signals via intentional impedance mistmatch, thereby eliminating the need of active circuitry. This makes them ideal to be deployed in IoT devices.

The pervasive information exchange arising from the aforementioned ubiquitous connectivity will inevitably lead to exponential increase in wireless data traffic, which has been estimated by ITU to approach a sizable amount of 5 zettabytes per month globally by the year 2030 [6]. Considering this enormous amount of data and its processing requirements, it is inevitable for future wireless networks to be data driven instead of

conventional model driven approach [7]. The rise of artificial intelligence (AI), specifically in the realm of machine and deep learning, has unlocked the potential for data driven end-to-end dynamic optimisation of communication systems through highly intelligent control. Especially with the recent breakthroughs in deep learning (DL), such approaches are being widely adopted to tackle various challenges of IoT enabling technologies.

The primary focus of this thesis is on BackCom, studying its key challenges, and enhancing its capabilities. In addition, there has been significant research progress in other 6G technologies like wireless power transfer, intelligent reflecting surfaces (IRS), multi-antenna systems and machine learning based techniques. We discuss innovative ways to integrate these technologies with BackCom in a holistic manner to address the challenges encountered in the context of IoT.

1.1 Theoretical Background

1.1.1 Backscatter Communication

Backscatter Communication has been envisioned as a promising technology with the potential to realize energy efficient ubiquitous connectivity among the large number of devices for the IoT. In BackCom systems, a tag or backscatter device (BD) leverages existing RF signals in its surroundings (generated from a dedicated RF source or from other RF sources in its surroundings like TV towers, Wi-Fi access points or a base stations from the cellular network) to convey its own information [1]. The backscatter device or tag modulates the backscattered signal by switching between the following two states: a backscattering state, when the tag antenna is short-circuited, and a transparent state, when the tag antenna is open-circuited [8]. These states correspond to bit '0' and bit '1'. Typically, an energy detector (ED) [9] is used at the backscatter receiver or reader to detect the BackCom symbols, by calculating the received power levels at the backscatter receiver (RX) and then mapping them to corresponding transmitted signals from the BD. Consequently, the BackCom system is energy efficient as it does not require active RF signal transmission. Moreover, such devices have simplified circuitry.

There are three main types of BackCom architectures as illustrated in Fig. 1.1 and described below:

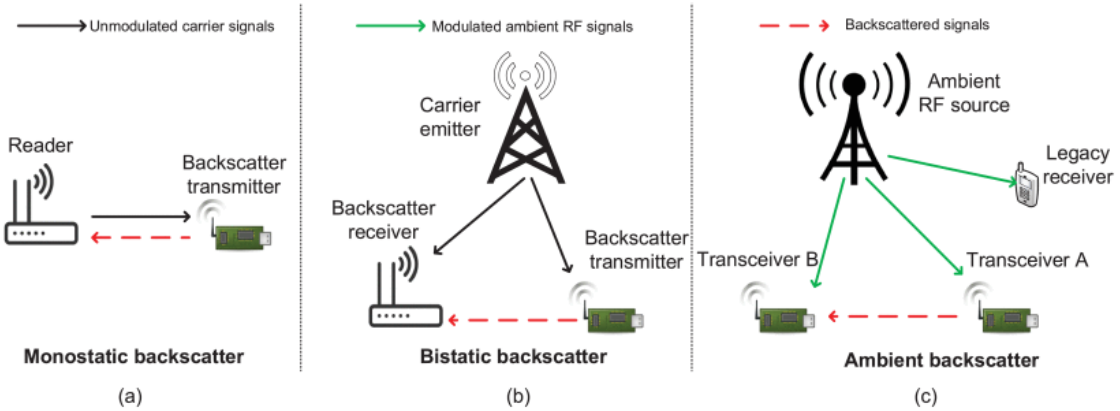

Figure 1.1: Three types of BackCom Architecture [1].

1.1.1.1 Monostatic Backscatter

Monostatic backscatter is the most classic mode of backscatter communication where the same antenna or transceiver is used for both transmitting and receiving signals. In monostatic backscatter systems, the transmitter sends out a signal, which interacts with a passive backscatter device or tag. This device then reflects or modulates the incoming signal to convey information, and the same antenna or transceiver used for transmission also captures the reflected signal for reception.

Monostatic BackCom systems have a relatively simple hardware setup since a single antenna or transceiver handles both transmission and reception. These systems are commonly found in applications like Radio-Frequency IDentification (RFID), where passive tags reflect signals back to the same reader device for data retrieval. Such can be energy-efficient, particularly when designed for low-power and battery-less operation. They are suitable for applications where power constraints are critical. Monostatic systems suffer from limitations like very short range, low achievable bit rate and challenges related to interference and noise, as the same antenna or transceiver is used for both transmission and reception, potentially leading to signal degradation.

1.1.1.2 Bistatic Backscatter

Bistatic backscatter is a specific mode of backscatter communication where two separate antennas or transceivers are employed—one for transmitting signals (carrier emitter) and another for receiving reflected or modulated signals (the receiver). In bistatic backscatter systems, the transmitter sends out a continuous wave (CW) or a modulated signal, which interacts with a passive backscatter device or tag. This device reflects or modulates the

incoming signal to convey information, and a separate receiver antenna or transceiver captures the reflected signal for reception.

Bistatic systems have a more complex hardware setup compared to monostatic systems since they use two separate antennas or transceivers—one for transmitting and one for receiving. The main premise of this architecture is to decouple the carrier emitter-to-tag and the tag-to-Sreader distances so as to achieve longer transmission range and better coverage. Moreover, the separate transmitter and receiver antennas provide greater flexibility in terms of antenna design and orientation, which can be advantageous in certain applications. A challenge faced by bistatic systems is the need for a dedicated carrier emitter and synchronization between the transmitter and receiver to ensure accurate signal reception, which can introduce complexity in some scenarios. Bistatic systems find applications in long-range RFID, remote sensing, and radar systems.

1.1.1.3 Ambient Backscatter

Ambient backscatter communication is the third and most novel BackCom architecture that harnesses existing RF signals in the environment as the carrier for data transmission. Unlike traditional communication systems that actively generate RF signals for data exchange, Ambient BackCom devices are passive and rely on backscattering ambient RF signals such as those from Wi-Fi routers, TV broadcasts, cellular towers, or other wireless transmitters, as carriers for communication. Such devices are extremely energy-efficient because they do not require power-hungry signal generation. Therefore, such devices are relatively simple and cost-effective to manufacture and deploy. They can operate on minimal power and are suitable for battery-less or energy-harvesting applications. However, their communication range is typically limited to the range of the ambient RF signals. The signal strength of the ambient RF source and the device's sensitivity influence the effective communication range. Moreover, Ambient BackCom suffers from the issue of direct-link interference, i.e., the weak BackCom signal gets over powered by the original ambient RF signal at the receiver.

Ambient BackCom is well-suited for applications where energy efficiency, simplicity, and low cost are essential. It finds applications in IoT sensor networks, asset tracking, smart agriculture, and environmental monitoring.

1.1.2 Intelligent Reflecting Surface

Another promising technology, intelligent reflecting surface (IRS) has recently emerged and is expected to revolutionize and transform future wireless networks [2, 10–13]. An

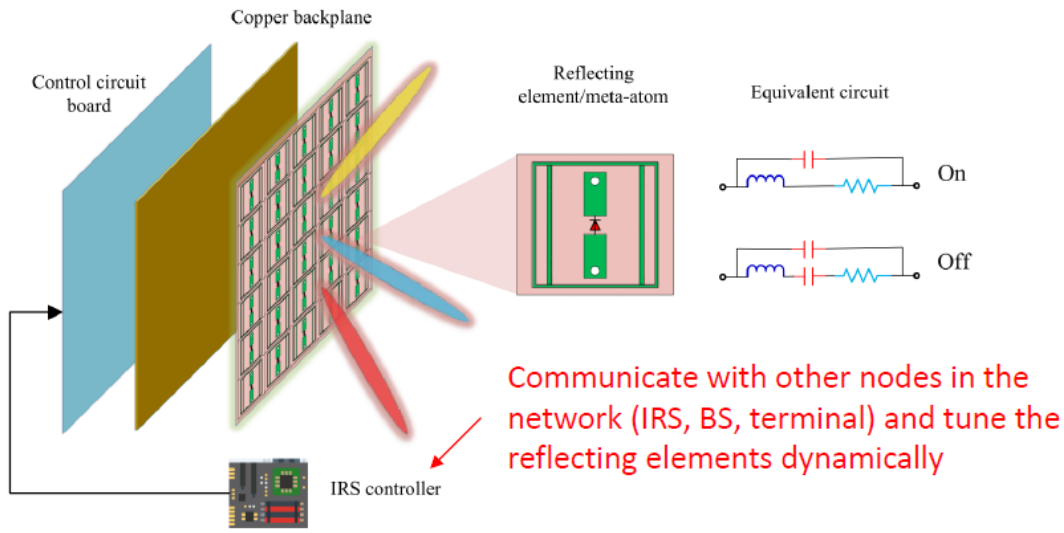

Figure 1.2: Intelligent Reflecting Surface [2]

IRS is an array of reconfigurable reflecting elements as shown in Fig. 1.2, that can interact directly with impinging signals in a controlled manner to apply a particular set of phase-shifts, thereby controlling the direction of reflection. Thus, the coordinated design of phase shifts for a large number of IRS reflectors allows reflected signals to be received constructively (or destructively) at a receiving node [14–16]. This allows the IRS to mitigate the inter-user interference or improve the signal quality at some specific and localized network locations. It is noteworthy, that the IRS technology is nearly passive, as it is completely based on the scattering of the electromagnetic waves. Therefore, the IRS can improve the signal reliability and overall efficiency and coverage of the network in a cost-effective and energy-efficient manner, without the need for additional densification of the network elements and/or active antennas at the transmitters and receivers [10].

It's important to note that BackCom devices and IRS have a shared characteristic in that they both enable incoming signals to be passively reflected with minimal energy consumption. In fact, when configured as an amplify and forward relay, a multi-antenna BackCom device behaves similarly to an IRS based on reconfigurable reflect-arrays. Nevertheless, the primary distinction between these two technologies arises when they are employed in a supporting role. In such cases, IRS typically refrains from signal processing and doesn't transmit its own data. Thus, assuming these two conditions hold, the primary role of the IRS is to serve as a dynamic element in the wireless environment, assisting other transmissions and enhancing their efficiency. In the context of this thesis,

the IRS is exclusively utilized to augment BackCom systems in chapters 3 and 4.

1.2 State-of-the-Art

In this section we review the state-of-the-art in BackCom. We highlight key research challenges in BackCom and also present a detailed literature review of the issues that we have addressed in later chapters of this thesis.

1.2.1 Research Challenges in BackCom

Within the evolving landscape of green communications, BackCom is poised to assume a crucial role. This is particularly relevant in the context of the requirements of ultra-dense connectivity in future wireless networks, including the anticipated 6G framework. BackCom's significance lies in its potential to facilitate the provisioning of emergent services that align with these advancements. Notably, it stands to support services like massive IoT, enhanced broadband capabilities, and a diverse array of innovative service offerings that are expected to be part and parcel of future wireless networks [6].

Although the foundational concept of backscatter operation is straightforward, the journey towards establishing a viable practical backscatter communication system suitable for real-world IoT applications is far from complete. Within this pursuit, the research community has highlighted several principal challenges inherent to backscatter communication. In the following, we present a brief overview of these challenges:

1.2.1.1 Range Extension

There are a variety of IoT services that demand extensive communication ranges. Achieving such long-distance communication is a formidable challenge, especially in the context of BackCom systems. Significant signal loss occurs during reflection at the backscatter tag. Additionally, radio signals undergo path loss twice: first from the transmitter to the tag and then from the tag to the receiver—unlike conventional wireless technologies, which experience path loss only once.

Traditionally, the range issue has been addressed in wirless communication by either increasing transmission power or adopting specialized modulation schemes. However, these solutions are not easily applicable to BackCom systems. Firstly, boosting transmission power to compensate for additional attenuation in BackCom may necessitate a fourfold increase in power as the distance doubles, potentially exceeding electronic component limitations, circuit design constraints, power budgets, and government reg-

ulations. Secondly, backscatter tags have restricted processing capabilities for incoming signals due to power constraints. Consequently, implementing special modulation schemes on standard backscatter tags becomes challenging, requiring the development of unique techniques to overcome this obstacle. These issues collectively make constructing a long-range BackCom system a daunting task.

The range limitation and coverage challenge within BackCom has lead to the emergence of newer configuration arrangements for the RF source, tag, and reader components (Bistatic architecture) to minimize the resulting path loss. These configuration sets have the potential to enhance BackCom's range while simultaneously decreasing path loss. In addition, several techniques have been employed to enhance the range of BackCom systems, e,g., introduction of microcode [17], using variants of amplitude and frequency modulations [18, 19] and developing tags with advanced modulation schemes like CSS-modulated LoRa [20] and using multiple antennas at the reader or tag. Despite the variety of research efforts, the issue of limited range still exists in BackCom systems.

1.2.1.2 Data Rate

Many IoT applications demand wireless data rates significantly faster than several kilobits per second. For instance, voice streaming requires bit rates exceeding tens of kilobits per second, while video applications go over 1 megabit per second during active operation. The need for increased data rates is expected to go higher with future applications involving augmented and virtual reality. Conventional radio technology effectively addresses this challenge by employing advanced modulation techniques to maximize the utilization of available channel bandwidth. However, adapting similar solutions to backscatter communication proves challenging as implementing highly complex modulations on a backscatter tag presents a nontrivial task due to its limited capacity for manipulating RF signals and performing baseband processing. Moreover, achieving high throughput typically demands high-performance electronic components and rapid computational capabilities, which in turn lead to increased energy consumption. Consequently, supporting high-throughput applications within backscatter communication systems becomes a complex endeavor, necessitating a careful tradeoff to strike a balance between throughput and per-bit energy consumption. In this regard, several protocols and prototypes have been developed including BackFi [21], passive Wi-Fi [22] and FreeRider [23] among others.

1.2.1.3 Energy Efficiency

As discussed before, one of the chief reasons for increasing research interest in BackCom is the technology's ultra low-power characteristics, which hold immense promise for enabling battery-free IoT applications. In some scenarios, these applications may require continuous, always-on communication, making RF signals the most viable ambient energy source for energy harvesting, surpassing alternatives like solar and vibration. Consequently, there is a strong motivation to develop backscatter communication systems capable of relying entirely on ambient RF energy for power. However, it's important to note that the typical efficiency of RF energy harvesting is quite low, standing at a mere 18.2% when the ambient RF signal strength is at -20 dBm, and a mere 0.4% at -40 dBm [24]. This extremely limited energy budget poses significant challenges for both hardware and system design.

In the recent years, several energy efficient prototypes have been presented, e.g., the work in [8] presents the first backscatter communication system that runs solely on energy harvested from ambient RF signals. Another work [25] presents an energy efficient BackCom tag design by eliminating digital computational components, such as the FPGA and ADC/digital-to-analog converter (DAC), while working on RF energy harvested from a cellular base station 9.4 m away. Other prototypes have been developed that trade off energy efficiency to optimize other parameters e.g., higher data rate [21,25] and increased range [20].

1.2.1.4 Deployment

A typical backscatter communication system comprises essential components: a backscatter tag and supporting devices in the form of a carrier transmitter and receiver. While the backscatter tag is typically small and cost-effective, the transmitter and receiver tend to be expensive and bulky, significantly inflating deployment costs. Unlike established wireless technologies like Wi-Fi and Bluetooth, backscatter communication operates in a relatively niche market, leading to limited incentives for manufacturers to produce these supporting devices on a large scale at low costs.

Most recent innovations in backscatter technology often require specialized equipment like software-defined radio devices or custom hardware, potentially discouraging users due to the initial investment, especially when conventional wireless communication infrastructure like LTE and Wi-Fi is readily available. Consequently, the high deployment cost presents a significant hurdle to the practical adoption of backscatter communication.

To address this challenge and reduce costs, leveraging existing, affordable, and widely

available commodity devices as backscatter transmitters or receivers is desirable. These commodity devices can include conventional wireless devices like Wi-Fi access points (APs) or Bluetooth-enabled computers, which are already present in many scenarios where backscatter communication is intended. Utilizing these devices can significantly lower deployment overhead. Moreover, commodity wireless devices often incorporate mature technologies that have undergone extensive optimization efforts over the years. For instance, many Wi-Fi chips provide excellent sensitivity as good as -80 dBm while remaining cost-effective, making them an attractive choice for improving system performance.

However, achieving the goal of using commodity hardware for backscatter transmission and reception presents two primary challenges. First, the backscatter tag must effectively inject data onto an excitation signal transmitted by commodity devices like Wi-Fi or Bluetooth packets. This can be challenging because backscatter tags lack the ability to decode the signal and must inject data blindly. Second, the commodity receiver must decode and process a signal modified and reflected by a backscatter tag. The challenge here lies in the limited control that commodity wireless devices typically allow over the decoding process. Packets altered by a backscatter tag may be ignored or corrupted during decoding, potentially preventing them from reaching a user-space program.

1.2.1.5 Interference Management

Interference management is a critical challenge in BackCom systems. Interference can arise from various sources and can significantly impact the performance and reliability of communication between BackCom devices/tags and readers. The interference management issues in BackCom can be categorized as:

- **External RF Interference/Direct-link Interference:** BackCom systems often operate in shared frequency bands with other wireless devices and communication systems. Interference from nearby devices operating in the same frequency range can disrupt communication between tags and readers. Managing and mitigating external RF interference is crucial for reliable operation, especially in the context of Ambient BackCom systems.

- **Interference from Multiple Tags:** In scenarios with a large number of tags in close proximity, multiple tags may transmit simultaneously or collide while trying to respond to a reader's query. This tag-to-tag interference can lead to data collisions and reduced system performance. Anti-collision protocols and multiple

access techniques are essential to address this issue by ensuring that tags take turns communicating with the reader.

- **Multipath and Signal Reflection** In indoor environments or areas with many reflective surfaces, multipath propagation can occur. Signals can bounce off walls, floors, and objects, leading to multiple signal paths and reflections arriving at the reader. Managing and interpreting these reflections can be challenging and may lead to errors or reduced communication range.
- **Noise and Signal Quality** The quality of the backscattered signal from a tag can be affected by noise, fading, and attenuation, especially in challenging environments. Managing noise and optimizing signal quality through error correction techniques or signal processing is essential to improve reliability.
- **Coexistence with Other Wireless Technologies** In many real-world scenarios, backscatter communication systems need to coexist with other wireless technologies such as Wi-Fi, Bluetooth, and cellular networks. Interference from these technologies can degrade backscatter communication performance and requires careful spectrum management and interference avoidance strategies.
- **Dynamic Environments** In dynamic environments where tags or readers are in motion or where the environment changes rapidly, interference patterns can fluctuate. Adapting to dynamic interference conditions and ensuring continuous communication is a complex challenge.

1.2.1.6 Security

Privacy and security are significant concerns in BackCom systems, particularly in applications that involve the tracking or monitoring of physical objects or people. Since BackCom systems often collect and transmit data from passive tags or devices (which may include information about objects, individuals, or assets), protecting the privacy of this data is critical, as unauthorized access or tracking could lead to privacy violations. Unauthorized readers or eavesdroppers may attempt to intercept the communication between tags and legitimate readers. This can lead to the unauthorized collection of sensitive information or tracking of objects or individuals without their consent. Furthermore, ensuring the integrity of the data transmitted by backscatter devices is essential. Tampering with the data on the tags or during transmission can have serious consequences, especially in applications like supply chain management or healthcare. Similarly, verifying the authenticity of the tags and readers is crucial. Without proper authentication

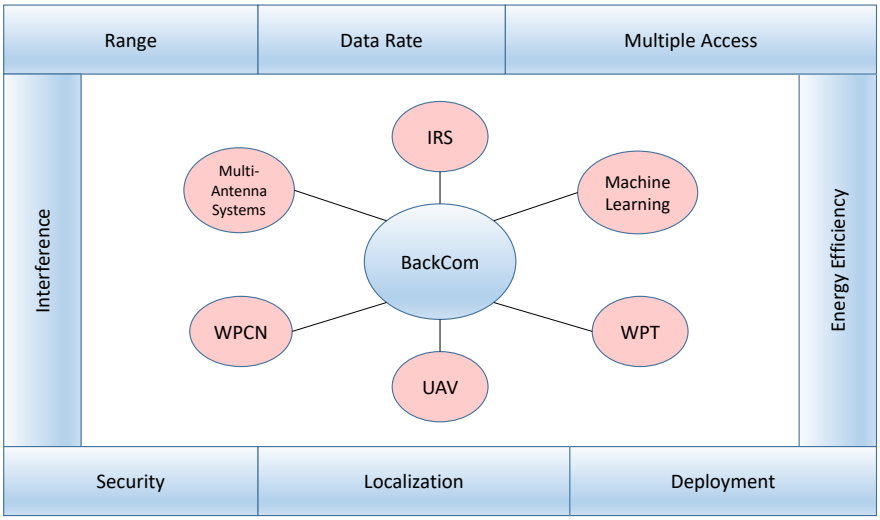

Figure 1.3: Research Challenges in BackCom.

mechanisms, malicious devices could impersonate legitimate ones, leading to unauthorized access or data compromise. Encrypting the data transmitted between tags and readers can help protect it from eavesdropping and unauthorized access. Several works have addressed the issue of eavesdropper security, e.g., [26] employs selection of best relay scheme to avoid attacks, [27] injects noise like signals into the carrier wave and [28] highlighted the blackhole attack.

1.2.1.7 Integration of BackCom with Other Technologies

As we move towards 6G wireless systems, there are a number of exciting technologies emerging including but not limited to Intelligent Reflecting Surface, Massive MIMO, Wireless Power Transfer (WPT), Wireless Powered Communication Networks (WPCNs) and Unmanned Aerial Vehicles (UAVs), in addition to machine learning techniques. Instead of solely focusing on improving a single technology in isolation, research focus has shifted towards synergizing wireless communication technologies to achieve seamless, strong, and efficient communication. In this thesis, we investigate the integration of BackCom with other 6G technologies to tackle the research challenges mentioned above and illustrated in Fig. 1.3 to attain performance levels that BackCom alone could not achieve.

1.2.2 Literature Review

In this section we present a detailed literature review of the prior work done in regards to our identified design challenges in our considered system scenarios.

1.2.2.1 Wireless Power Transfer

As we move towards a world filled with a large number of IoT devices, the means to sustainably powering these IoT devices is a key challenge. In this regard, far-field WPT is a promising technology to provide convenient wireless charging to low power IoT devices [29–32].

The problem of efficient WPT from an energy transmitter (ET) to an energy receiver (ER) has received much attention in the literature [33–42]. Typically, WPT relies on highly directional beamforming to increase the end-to-end power efficiency and overcome the severe RF signal attenuation over distance. In this regard, different beamforming architectures have been proposed [33–35]. However, the implementation of these beamforming architectures requires channel state information (CSI) estimation at the ET [36,37] or at the ER [38–41], or energy feedback from the ER to the ET [42,43]. CSI estimation at the ER increases the complexity of the ER, which is undesirable. In addition, training methods suffer from high feedback overhead, which should also be avoided.

Employing the concept of retrodirectivity is a promising solution to avoid the need for any CSI estimation for efficient WPT [32, 44]. Originally, retrodirective arrays, such as Van Atta array [45] and Pon array [46], were proposed as 'reflection type' arrays to reflect an incident signal back to the direction that it came from. This reflection of incoming waves is realized by their reversal in the time domain or phase conjugation in the frequency domain. Recently, more advanced versions of arrays employing the retrodirective principle have been developed for the purpose of WPT [44, 47–50]. The retrodirective WPT exploits channel reciprocity and provides WPT without explicit channel estimation. In particular, it involves the ET equipped with a phased array, providing WPT to an ER. This is accomplished by the ET first receiving a signal from the prospective ER, which then serves as a reference signal to steer a beam back towards the ER. This is done by conjugating this received signal and using this conjugated signal to set the phase of an energy signal such that it is emanated towards the ER [32]. In this regard, a novel massive MIMO retrodirective WPT scheme was proposed in [51]. However, this scheme still required active signal transmission from the ER to initiate WPT, which consumes energy and may not be desirable for low power IoT devices. The active signal transmission from the ER to the ET was avoided in [52] by enabling the ER to backscatter

the pilots emitted by the ET. However, conventional beamforming was still employed at the ET. A WPT scheme employing monostatic backscatter at the ER and retrodirective WPT at the ET was proposed in [53]. However, the charging request was initiated by the ET using active transmission.

1.2.2.2 Ambient Backscatter Communication

In addition to BackCom's fundamental aspect of keeping tag power consumption low and circuitry simple, it is also desirable to keep RF emissions by the large number of IoT devices in check. This led to the emergence of the Ambient BackCom architecture. As explained in Section 1.1, this architecture enables the tag to make use of ambient RF signals generated from ambient RF sources for communication [8, 9, 17, 18, 21, 22, 54–60].

A key issue in ambient backscatter communication systems is the direct-link interference that the RF ambient source causes to the tag. Since Ambient BackCom involves devices that modulate and reflect existing wireless signals for communication, the presence of direct links between the primary transmitter and receiver can introduce interference that degrades the performance of the Ambient BackCom system. This interference can significantly degrade the quality of the BackCom signal and can lead to errors in data transmission and reception, resulting in reduced communication reliability. Moreover, it can limit the effective communication range and achievable data rate of the Ambient BackCom system.

Several works in literature have striven to solve the problem of DLI cancellation and improving the quality of the BackCom signal by evaluating the impact of DLI on different aspects of system performance, e.g., bit error rate (BER) of ambient backscatter communication [54] and propose different techniques to resolve this issue. One approach is to consider this direct-link interference as a component of the background noise [9, 18, 55]. However, since the backscatter signal is very weak as compared to the ambient signal, such schemes do not perform so well. [56] demonstrated the existence of a BER floor in a single antenna backscatter device and used multiple antennas to cancel the direct link interference in a non-coherent receiver setup. Other approaches involve general signal processing techniques [22, 57–59] or techniques like frequency shifting [21, 60] which are not desirable at the low-power BackCom tag. The work in [61] created a hot-spot on the BD and a good reception spot on a RX using massive MIMO at the ambient source. The work in [62] discussed using multi-antenna reader to tackle the DLI problem and proposed optimal beamforming in terms of SINR maximization and zero-forcing beamforming based solutions. However, with practical system parameter values affect-

ing backscatter signal strength, the BER is still high for these two schemes. Thus, DLI still remains a fundamental limitation to the application of Ambient BackCom for future wireless networks. In this thesis, we have addressed the issue of DLI cancellation for Ambient BackCom in chapters 2 and 3. In chapter 2, a training design is proposed for Ambient BackCom supporting wireless power transfer, whereas in chapter 3 the DLI issue is tackled with a novel scheme for an IRS-aided Ambient BackCom system.

1.2.2.3 Monostatic Backscatter Systems

Monostatic BackCom architecture is the most fundamental of the three BackCom architectures and has been most commonly deployed in commercial RFID technology applications. The idea of communication using reflected power from different electromagnetic (EM) waves was first introduced in 1940s. Initially, BackCom found applications in object detection, particularly for air crafts, using radar techniques. In recent decades, it has gained prominence as a mainstream application in the form of RFID, widely utilized in industrial settings for locating, identifying, and tracking items. The EPC Class 1 Gen 2 protocol [63] serves as the governing standard for RFID systems, covering both the physical and upper layers.

With the increased interest in low power communication technologies, the research efforts in monostatic BackCom from communication theory perspective spiked up. The works in [64–66] explored aspects such as radar cross-section, propagation properties, and link budget. Further examinations of monostatic systems considered impedance choices at the tags, interference mitigation between tags, and higher-order modulation in [67,68]. The performance analysis of monostatic BackCom with multi-antenna readers was explored in [69], with subsequent optimization studies presented in [70, 71].

Despite its widespread deployment, monostatic BackCom faces significant challenges related to round-trip signal losses, inversely proportional to the fourth power of the reader-tag distance. This issue of severe round trip pathloss in such systems has limited their use to very short range applications. The range extension of monostatic BackCom is highly desirable as it will allow the technology to be used for a wider variety of applications requiring extended field coverage while reaping the benefits of reduced tag power consumption [72].

A variety of research works have been undertaken to explore the range extension issue of BackCom systems by either tweaking the microwave parameters of the tag [73] or using multiple antennas on either the reader [69] or the tag [74]. However, these efforts resulted in range extension of the order of a few meters. With smart wireless environ-

ments being the future of wireless networks, leveraging an IRS to improve the range and coverage of BackCom systems is an energy and cost effective solution. In chapter 3 of this thesis, we address the range extension issue of Monostatic BackCom through a smart wireless propagation environment realized by IRS and controlled by machine learning based techniques.

1.2.2.4 IRS-aided BackCom Systems

As mentioned in Section 1.1.2, IRS has recently gained popularity due to its potential for enabling other 6G technologies, by capitalizing on its ability to transform the wireless medium by the coordinated design of phase shifts at its reflectors (passive beamforming), to ensure constructive or destructive reception at desired locations in the network [11, 12]. The promising potential of IRS and its usefulness in solving key issues of existing technologies like multiple-input multiple-output (MIMO) systems, millimeter-wave (mmWave) communications, terahertz (THz) communications, UAV communication and mobile-edge computing has gathered a lot of interest [10, 14, 75–78]. Similar to these 6G technologies, passive communication systems like backscatter communication are expected to be widely deployed in IoT technology for pervasive connectivity. As a result, there will be an increased probability of an IRS being present nearby. Therefore, it is only natural to explore the opportunities afforded by IRS-aided backscatter systems.

Like other 6G technologies, BackCom can be favourably assisted by the IRS for performance improvement. It has been established in the literature that an IRS can assist in maximising signal strength at a receiver in proportion to IRS surface area [15]. The potential gain brought about by the IRS can help BackCom systems in improving the strength of the backscatter signal arriving at the receiver. In particular, for monostatic BackCom systems, a strategically placed IRS in the surroundings can enhance the performance of the conventional RFID type system in terms of rate and range.

IRS assisted BackCom systems are emerging in literature as evidenced by [79–91] and summarised in Table 1.1. Some of these works are in the area of IRS aided monostatic BackCom, e.g., the work in [80] presented performance analysis for an IRS -aided monostatic BackCom system with the direct reader-to-tag link blocked, whereas the work in [81] presented a channel estimation scheme for the base case of an IRS aided monostatic BackCom system with single tag and single antenna reader. An IRS-aided bistatic backscatter system was introduced in [82], solving the transmit power minimization problem while considering multiple signal reflections at the IRS due to the coexistence of the IRS and backscatter systems. Some works have explored the IRS aided ambient backscatter sys-

Table 1.1: Literature review of relevant works for Section 1.2.2.3

Ref	Configuration	Objective	Metric of interest
[80]	Monostatic BackCom	Performance analysis	Symbol Error Probability
[81]	Monostatic BackCom	Channel Estimation	Mean-square error (MSE)
[82]	Bistatic BackCom	Carrier Emitter (CE) transmit power minimization	Transmit Power of CE
[83]	Ambient BackCom	Achieving a higher transmission rate	Bit Error Rate (BER)
[84]	Ambient BackCom	BackCom signal strength maximization	BER
[85]	Cooperative Ambient BackCom	IRS as BackCom device for symbiotic radio	BER
[86]	Cooperative Ambient BackCom	Minimization of IRS power consumption	IRS Power Consumption
[87]	BackCom-aided WPN	Maximization of total network throughput	Throughput
[88]	RIS-Scatter	Unifying IRS and Ambient BackCom	BER
[89]	Ambient BackCom	Experimental prototype: IRS-aided Ambient BackCom	BER
[90]	Ambient BackCom	Optimizing IRS using deep reinforcement learning	BER
[91]	Monostatic BackCom	Optimzing IRS using supervised learning	Signal to noise ratio (SNR)
This work	Monostatic BackCom	Joint optimization of IRS and BackCom by unsupervised learning	SNR

tems with [83] discussing throughput maximization of such an IRS-aided short-range ambient backscatter communication and [84] presenting a scheme of designing optimal IRS phase shifts to assist an ambient backscatter system.

The potential of enhancing other backscatter architecture variants using IRS has also been considered in literature, e.g., the work in [85] proposed a joint optimization scheme to use an IRS to assist a symbiotic cognitive backscattering communication system, the work in [86] studied the transmission design problem to minimize IRS power consumption while maintaining QoS constraints for backscatter devices in a cooperative ambient backscatter communication system assisted by an IRS, the work in [87] examined backscatter-assisted wireless powered communication network empowered by IRS and the work in [88] presented a protocol for unifying BackCom and IRS. Some experimental works [89] have also emerged, demonstrating experimentally that by tuning the beam and the phase-shift of the IRS, the performance of ambient backscatter systems can be improved. Specifically, a "hot spot" is created on the tag or "coherent spots" are created both on the tag and the reader, so that all the direct and IRS-reflected waves combine coherently at the reader, thereby improving performance.

Recently, DL based approaches have started emerging in the literature for IRS aided BackCom systems as well, e.g., the work in [90] used a deep reinforcement learning (DRL) based framework to optimize the Ambient Backscatter Communication (AmBC) detection without any knowledge of CSI, while the work in [91] presented a supervised learning based approach for designing passive beamforming at the IRS for a single antenna monostatic backscatter system.

For the successful working for IRS-aided BackCom system, joint optimization of IRS and BackCom is crucial. Previously, one of the seminal papers in IRS literature [92], presented the joint optimization of the active transmit beamforming and the passive IRS phase shifts in conventional point-to-point MISO system and and provided a semi-definite relaxation (SDR) based centralized solution and an alternating optimization (AO) based

solution. However, in an IRS-aided backscatter system, the signal model and the design of IRS phase shifts becomes a lot more challenging as the coexistance of these two reflection-based systems lead to multiple reflections at the IRS being significant [82]. Recently, the work in [85] has dealt with joint optimization of the IRS with AmBC but under the special case of a symbiotic, cognitive ambient backscatter system where the original ambient signal and the backscatter signal are both jointly decoded at the RX. To the best of our knowledge, in regards to the IRS aided Ambient BackCom systems, a solid theoretical benchmark obtained through an analytical solution to the important problem of finding the optimal IRS phase shifts to augment the ambient backscatter signal strength was missing from the literature.

1.2.2.5 Use of Deep Learning Techniques for BackCom Systems

The emergence of DL techniques have the potential for revolutionizing the design and optimization of communication systems due to their ability to improve system performance and reduce the computational cost [93]. This is due to the fact that deep neural networks and their variants are trained offline and a well-trained neural network deployed online comprises only simple linear and non-linear transformations. Moreover, DL based techniques can extract meaningful features from raw data and construct a model-free data mapping with a large number of learnable parameters [94]. For the success of the IRS-aided BackCom system, the joint design of the beamforming at the reader and the IRS reflection coefficients is crucial, which is a difficult problem due to the multi-reflection nature of the system and the large number of parameters to be learned. Thus, DL based approaches have huge potential for realizing IRS-aided systems, in particular, the design of IRS phase shifts for different system applications, as evidenced by [95–101].

Despite this being a logical evolution to the conventional monostatic backscatter system, the idea of addressing the shortcomings of BackCom through a smart wireless propagation environment realized by IRS and controlled by deep learning based techniques, is relatively unexplored in literature. Future wireless networks providing pervasive connectivity based on energy efficient BackCom can be realized by capitalizing on a smart wireless propagation environment empowered by IRS and controlled seamlessly and intelligently by data-driven machine learning techniques [102]. Based on this idea, in Chapter 4 of this thesis, we study a monostatic BackCom system assisted by a nearby IRS in this work. We propose a deep learning based approach to jointly optimize the IRS and the reader beamforming to enhance the performance of the BackCom system in terms of its range and received SNR at the reader.

1.3 Considered Communication System Scenarios with their Specific Design Problems

While extensive research has been conducted on all three BackCom architectures, it's essential to highlight that the majority of commercially utilized BackCom applications today are rooted in the monostatic setup (e.g., RFID, contactless payments). Moreover, the monostatic architecture has a relatively straightforward design with the BackCom tags having simple hardware, which makes them easier and cost effective to deploy. Monostatic BackCom can also be integrated with existing communication systems and infrastructure, enabling seamless integration into various environments. This compatibility is crucial for practical applications and the deployment of IoT devices. Furthermore, due to the existing commercial deployment of the RFID systems, there are well-established standards and infrastructure for monostatic architecture, making it easier for businesses and consumers to adopt them.

Due to the issue of limited range in Monostatic BackCom systems, the bistatic architecture was introduced to enable range extension. However, it still requires a dedicated carrier emitter that is separate from the receiver/reader, which means additional costs. Furthermore, it does not possess the same level of deployment-readiness as monostatic BackCom. With the advent of IRS and machine learning teachniques, there are new degrees of freedom for enhancing the capabilities of the already prevalent monostatic architecture. The ambient architecture, on the other hand is also highly desirable because it has the additional highly coveted features of inter-operability with existing RF signals, not relying on a dedicated carrier emitter and not producing new RF emissions.

Owing to the reasons stated above, in this thesis, we study the monostatic and ambient architectures and evaluate their integration with 6G technologies to enhance the overall performance of the system. We consider generic system models that cover various use-cases and application scenarios and address the key challenges of range extension in Monostatic BackCom and direct-link interference in Ambient BackCom.

1.3.1 Ambient Backscatter Training for Wireless Power Transfer

For future wireless networks, energy beamforming is a favourable solution to increase end-to-end power efficiency. However, the existing beamforming approaches either require channel state information (CSI) estimation at the energy transmitter (ET) or the energy receiver (ER) or energy feedback from the ER. These schemes result in an increase in either the complexity of the ER or feedback overhead which is undesirable for

IoT systems. An alternative low complexity WPT scheme is retrodirective WPT. The idea of retrodirective transmission involves a multi-antenna array that can transmit a beamformed signal in the source direction of an incoming wave by conjugating its phase. Thus with no prior knowledge of the source direction, high link gain can be achieved while avoiding channel estimation. However, such a system always needs an interrogating signal from the prospective ER. In this work, we propose to employ ambient backscatter at the ER to request WPT from the ET.

An inherent issue in Ambient BackCom systems is the direct-link interference from the RF ambient source to the backscatter device. This is because the backscatter signal suffers inevitable attenuation and is much weaker than the original ambient signal, which has a pervasive and stronger presence. We study a wireless power transfer scenario and propose to use Ambient BackCom at the ER to request WPT from the ET. We propose the design of ambient backscatter training at the ER to tackle the following design challenge:

Research Problem: To solve the fundamental signal recovery problem at the ET of recovering the weak backscattered signal in the presence of strong direct-link ambient interference.

1.3.2 IRS-aided Ambient BackCom Systems

Despite the research efforts in the area of Ambient BackCom, the reliability in terms of bit error rate (BER) of such systems is still limited. This is due to the fact that the backscatter signal suffers double fading and when it arrives at the RX, it is very weak as compared to the ambient signal from the original RF source, also known as direct-link interference (DLI). The DLI is an unknown, already modulated signal, much stronger than the information signal of interest from the BD. It has been shown that, even in line-of-sight (LOS), the DLI and the AmBC signal can combine such that the received signals corresponding to bit '0' and bit '1' differ only in phase, but have very close values in terms of power [103]. In such a scenario, the ED performs poorly and BER is high.

To improve the performance of the ED, it is imperative to strengthen the backscatter signal and also to maximize the contrast between the received energies at the ED corresponding to bit '0' and '1'. To achieve this, we leverage an IRS to strengthen the backscatter signal. We study a general IRS-aided ambient backscatter scenario and propose a novel scheme to address the fundamental aspect of improving the detection of ambient backscatter signal at the RX. We accomplish this by designing the IRS phase shifts to improve backscatter signal strength and performing eigenvector beamforming

(EBF) assisted energy detection at the RX to maximize the ratio of the two received energies.

Research Problem: To optimize the reflection pattern of the IRS (passive beamforming) and the receive beamforming at the receiver to minimize the BER by maximizing the ratio of received energies corresponding to bit '0' and bit '1'.

1.3.3 IRS-aided Monostatic BackCom Systems with Learning

As noted in Section 1.1, the ability of BackCom systems to communicate without active circuitry makes them ideal to be deployed in IoT devices [1]. In fact, monostatic BackCom systems have been most commonly deployed in commercial RFID technology applications. However, the issue of severe round trip pathloss in such systems has limited their use to very short range applications. Newer architectures like bistatic and ambient have been explored but they have their own limitations, e.g., bistatic systems require a separate carrier emitter, which needs to be placed very close to the tags and the ambient architecture suffers from direct-link interference. Monostatic BackCom remains the most widely deployed architecture commercially and its range extension is highly coveted as it will allow the technology to be used for a wider variety of applications requiring extended field coverage while reaping the benefits of reduced tag power consumption [72].

Previously considered legacy solutions to extend the range of monostatic BackCom include tag modifications [73] and relay-aided and multi-antenna backscattering [69,104]. However, despite the high infrastructure cost, complexity, and power consumption of such techniques, the range extension has been incremental.

With smart wireless environments being the future of wireless networks, leveraging an IRS to improve the range and coverage of BackCom systems is an energy and cost effective solution. In particular, the coordinated design of the phase shifts at the IRS to enable constructive combining of signals can enhance the BackCom system by boosting both the forward and backscatter paths. The improved signal reception at the reader translates into the range extension of monostatic BackCom. Furthermore, the IRS can be deployed to "power up" the tags that are in areas with no signal reception.

For the success of the IRS-aided BackCom system, the joint design of the beamforming at the reader and the IRS reflection coefficients is crucial, which is a difficult problem due to the multi-reflection nature of the system and the large number of parameters to be learned. With the breakthroughs in DL, such techniques are being leveraged in the design and optimization of communication systems to improve system performance and reduce the computational cost [93]. This is due to the fact that trained deep neural networks can

extract meaningful features from raw data and construct a model-free data mapping with a large number of learnable parameters [94]. Moreover, with the pervasive information exchange requisite in future wireless network, learning based data-driven approaches are favoured over conventional model driven approach [7]. Thus, future wireless networks providing pervasive connectivity based on energy efficient BackCom can be realized by capitalizing on a smart wireless propagation environment empowered by IRS and controlled seamlessly and intelligently by data-driven machine learning techniques [102].

Despite this being a logical evolution to the conventional monostatic backscatter system, the idea of addressing the shortcomings of BackCom through a smart wireless propagation environment realized by IRS and controlled by deep learning based techniques, is unexplored in literature. BackCom for energy efficiency, IRS for low cost smart propagation and machine learning based data driven intelligent control are three innovative paradigms that have proved their utility and potential for next generation self-sustainable wireless networks. Deployed together, they can help realize massive energy efficient connectivity for future IoT in a cost effective manner. With this motivation, we study a monostatic BackCom system with a multi-antenna reader, assisted by a nearby IRS. We propose a deep learning based approach to jointly optimize the IRS and the reader beamforming to enhance the performance of the BackCom system in terms of its range and received SNR at the reader.

Research Problem: Jointly optimize the reflection pattern of the IRS (passive beamforming) and the beamforming at the multi-antenna reader to maximise the SNR of the backscattered signal received at the reader.

We aim to tackle some of the research challenges identified above by synergizing BackCom with other 6G technologies in terms of system modelling, design and anaylsis of such integrated systems. In the next section, we summarize the scope and contributions of this thesis.

1.4 Thesis Overview and Contributions

This thesis proposes design insights and performance analysis of three different network scenarios where BackCom is integrated with other 6G technologies. Figure 1.4 shows an overview of the thesis chapters. In this regard, an ambient backscatter training scheme is proposed for wireless power transfer in Chapter 2. An IRS aided Ambient BackCom system with enhanced performance is presented in Chapter 3. The joint optimization of passive beamforming at the BackCom tag and active beamforming at the reader using unsupervised deep learning is proposed in Chapter 4. The chapter-wise summary of the

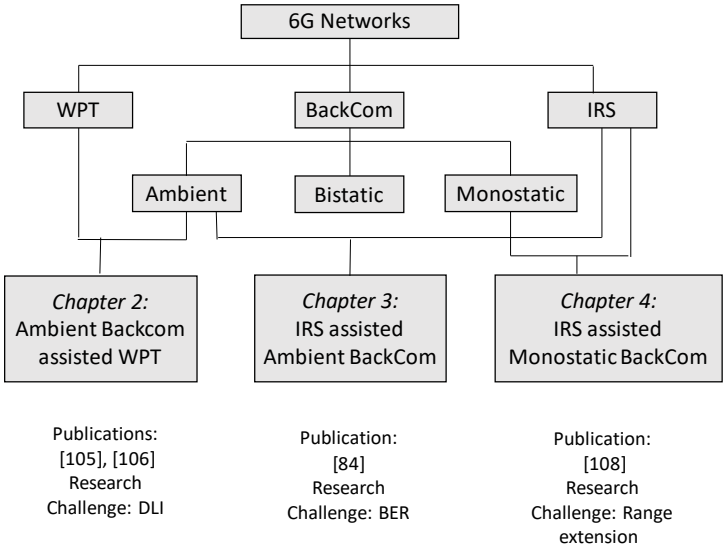

Figure 1.4: Thesis Organization.

contributions by this thesis is given as follows:

Chapter 2 - Design of Ambient Backscatter Training for Wireless Power Transfer

In this chapter, we consider a scenario with an ET equipped with a large phased antenna array capable of retrodirective WPT and an ER equipped with an ambient backscatter tag. The fundamental signal recovery problem at the ET is then: *How to recover the weak backscattered signal in the presence of strong direct-link ambient interference?* We consider this problem assuming general Nakagami-m fading and non-linear energy harvesting model. In this context, our main contributions are:

- Taking inspiration from Direct Sequence Spread Spectrum (DSSS)[1], we consider an ambient backscatter training scheme in which we vary the backscatter coefficient at the ER. This in effect multiplies the backscattered signal with a DSSS training signal and aims to capitalize on the spreading gain to boost the backscattered signal. We show that with a pseudo-noise (PN) training sequence, the average harvested

[1]DSSS transmission employs a chipping code to "spread" the transmission over a wider frequency band than it would normally occupy.

power at the ER is small and it even reduces as the training period increases. This is due to the fact that the use of PN training sequence completely fails in dealing with the strong direct-link ambient interference.

- We then propose the design of the training sequence (i.e., the pattern of varying the reflection coefficient), to completely eliminate the direct-link ambient interference. We show that when the ambient symbol duration is known, the ambient interference is cancelled as long as there are equal number of $+1$ and -1 chips over one ambient symbol. The number of chips or equivalently the switching rate does not matter in this case. Hence, we can use the slowest switching rate, i.e., we can switch the backscatter coefficient only twice per ambient symbol period. We analytically model the system and derive a closed-form expression for the average harvested power at the ER. We show that this deterministic training sequence scheme has superior performance as compared to the PN training sequence scheme.

- Finally, we show that the proposed solution is robust to small timing offset mismatch at the correlator. This is because the undesired component is still perfectly eliminated. However, good synchronization is needed for the best performance. In addition, when the ambient duration is unknown, the power transfer performance under the proposed deterministic training scheme can be severely degraded. This is due to unequal durations of $+1$ and -1 chips in one ambient symbol. We show that in this mismatched case, the number of chips does matter, i.e., it is best to use a fast switching rate to minimize the effect of the uncancelled ambient. In addition, we consider interference from neighbouring signals in the ambient environment, which is shown to impact the energy harvesting performance. However, the system can still harvest tens to hundreds of μW of power if these interference signals from neighbouring ambient sources are significantly weaker than the direct-link ambient signal.

The results of this chapter have been presented in the following publications [105, 106]:

J1. S. Idrees, X. Zhou, S. Durrani and D. Niyato, "Design of Ambient Backscatter Training for Wireless Power Transfer," in IEEE Trans. Wireless Commun., vol. 19, no. 10, pp. 6316-6330, Oct. 2020.

C1. S. Idrees, X. Zhou, S. Durrani and D. Niyato, "A Retrodirective Wireless Power Transfer Scheme for Ambient Backscatter Systems," 2020 IEEE Intl. Conf. Commun. (ICC), Dublin, Ireland, 2020, pp. 1-6.

Chapter 3 - Design of IRS-boosted Ambient Backscatter

In this chapter, we study a general IRS-aided ambient backscatter scenario with on-off keying deployed at the backscatter tag and an ED deployed at the receiver. For improved performance of the ED, it is vital to strengthen the backscatter signal and to maximize the contrast between the received energies at the ED corresponding to the two backscatter symbols. We propose a novel scheme to address the fundamental aspect of improving the detection of ambient backscatter signal at the receiver. We accomplish this by designing the IRS phase shifts to improve backscatter signal strength and performing eigenvector beamforming (EBF) assisted energy detection at the RX to maximize the ratio of the two received energies. The main contributions of this paper are as follows:

- We study the BER minimization problem in an IRS-aided AmBC system. We present the system and signal model considering two significant reflections at the IRS and formulate a general optimization problem for BER minimization. As the general problem is difficult to solve, we propose a simpler two-step approach that is computationally less intensive.

- We find the optimal value of the IRS phase shifts that maximize the received backscatter signal strength at the RX. Since this optimization problem is non-convex we use the minorization-maximization (MM) algorithm to obtain approximate solutions for the IRS phase shifts. Despite being suboptimal, the IRS phase shifts effectively boost the strength of the backscatter signal arriving at the RX.

- Our results show that the IRS phase shifts obtained from the proposed scheme effectively boost the strength of the backscatter signal at the energy detector. With a stronger backscatter signal, the eigenvector beamformer maximizing the relative difference in received energies of bit '0' and bit '1' leads to an improved BER under realistic channel parameters as compared to the previous schemes, which is an important improvement for IoT systems.

The results of this chapter have been presented in the following publication [84]:

J2. S. Idrees, X. Jia, S. Durrani and X. Zhou, "Design of Intelligent Reflecting Surface (IRS)-Boosted Ambient Backscatter Systems," in IEEE Access, vol. 10, pp. 65000-65010, 2022.

Chapter 4 - Joint Active and Passive Beamforming for IRS-aided Monostatic Backscatter Systems: An Unsupervised Learning Approach

In this chapter, we study an IRS-aided monostatic BackCom system with a single antenna tag and multi-antenna reader. The reader emits unmodulated signals that the tag leverages for backscatter communication back to the reader. The IRS assists the BackCom system by reflecting the signals on the forward as well as backscatter path. Thus, the joint design of IRS phase shifts and the beamforming at the reader becomes a non-trivial problem, due to the coupling of the two variables and because both the forward and the backscatter paths have a direct and a via-IRS component. We present the system and signal models and the problem of jointly optimizing the passive beamforming at the IRS and the active beamforming at the reader to maximize the backscatter signal strength arriving at the reader, as a means to extend the range of monostatic BackCom. For benchmarking purpose, we solve the non-convex optimization problem of maximising the SNR using the conventional semidefinite relaxation (SDR) based approach, which is a common practice for IRS optimization in literature [107]. The main contributions of this paper are:

- We present a novel Deep Residual Convolutional Neural Network (DRCNN) network named *BackIRS-Net*, to tackle the joint optimization problem mentioned above. The proposed network exploits the unique coupling that exists between the active beamforming at the reader and the passive beamforming at the IRS. It first learns the beamforming vector at the IRS using the channel input, which is then combined with the channel information to learn the beamforming vector at the reader. We present the network architecture, feature design, training and tuning of hyper-parameters and its testing on unseen data.

- We perform a complexity analysis of our proposed approach versus the conventional optimization based approach. The analysis indicates that once trained, the proposed *BackIRS-Net* requires substantially less computation complexity and hence time. In particular, for large IRS, a trained *BackIRS-Net* significantly outperforms the SDR based approach in terms of computational complexity and time.

- We conduct extensive numerical simulations to evaluate the viability of our proposed DL- based approach and to compare it with benchmark schemes. Our results indicate that with the assistance of IRS, the effective SNR at the reader of the backscatter signal is effectively boosted. We show that the performance of our proposed *BackIRS-Net* is very close to the SDR approach while incurring far

less complexity. Moreover, with the increase in IRS size, the performance gap reduces further. We also demonstrate that our proposed DRCNN based network architecture performs better than a simpler multi-layer perceptron (MLP) based framework.

- Our results show that our monostatic BackCom system, even when assisted by an IRS of modest size ($N = 25$), experiences a range extension by a factor of more than 4 times that of the no-IRS scenario. With an IRS of larger size, the increase in range is even more substantial.

The results of this chapter have been presented in the following publication [108]:

J3. S. Idrees, S. Durrani, Z.Xu, X. Jia, and X. Zhou, "Joint Active and Passive Beamforming for IRS-assisted Monostatic Backscatter Systems: An Unsupervised Learning Approach," in *IEEE Trans. Mach. Learn. Commun. Netw.*, Jan 2024.

Finally, Chapter 5 provides a summary of the thesis results and makes suggestions for future research work.

Chapter 2

Design of Ambient Backscatter Training for Wireless Power Transfer

Far-field WPT is a promising technology to provide convenient wireless charging to low power IoT devices. Typically, WPT relies on highly directional beamforming to increase the end-to-end power efficiency and overcome the severe RF signal attenuation over distance. However, CSI estimation requisite for WPT is a challenge. So in this chapter, we propose to employ the concept of retrodirectivity to avoid the need for any CSI estimation for efficient WPT.

The retrodirective WPT exploits channel reciprocity[1] and provides WPT without explicit channel estimation. In particular, it involves the ET equipped with a large phased array, providing retrodirective WPT to an ER equipped with an ambient backscatter tag. This is accomplished by the ET first receiving a signal from the prospective ER, which then serves as a reference signal to steer a beam back towards the ER. This is done by conjugating this received signal and using this conjugated signal to set the phase of an energy signal such that it is emanated towards the ER. We propose to leverage ambient BackCom at the ER to send WPT request to the ET. The fundamental signal recovery problem at the ET is then: How to recover the weak backscattered signal in the presence of strong direct-link ambient interference (DLI)?

To solve the issue of DLI, we propose a training sequence design, i.e., pattern of varying the reflection coefficient at the ER. We show that when the ambient symbol

[1] An alternative to the channel reciprocity assumption is to utilize some sort of feedback mechanism from the energy receiver, once it receives training sequences from the energy transmitter [42, 43]

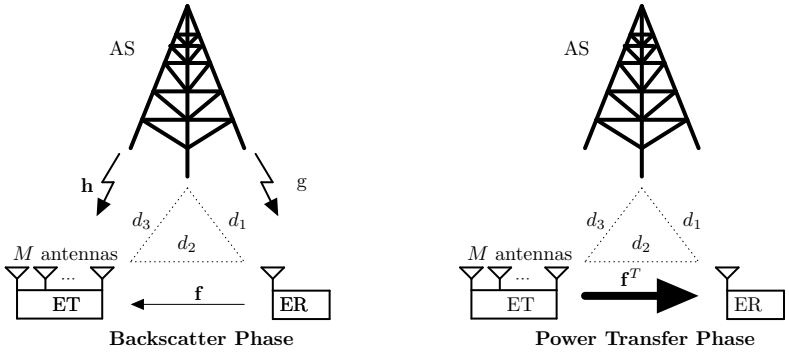

Figure 2.1: Illustration of the system model.

duration is known, the ambient interference is fully cancelled by the proposed design. We analytically model the system and find the average harvested power at the ER considering Nakagami-m fading channels and non-linear energy harvesting model. Our results clearly show that the proposed solution is robust to a small timing offset mismatch at the correlator.

This chapter is organized as follows: Section 2.1 describes the system model and assumptions, along with the proposed wireless power transfer scheme and its phases. Section 2.2 presents the signal model of the system in terms of mathematical equations and defines the metric of interest. Section 2.3 gives the analysis of the proposed scheme with a PN sequence applied at the ER. Section 2.4 proposes the design of the deterministic training sequence for the elimination of the direct-link ambient interference and also gives the analysis of the system in this scenario. Section 2.5 deals with the impact of practical system aspects like imperfect synchronization at the correlator and change in ambient symbol duration. Section 2.6 presents the numerical results. Finally, Section 2.7 concludes the chapter.

2.1 System Model

We consider a WPT scenario with an ambient source (AS), an energy transmitter (ET) and an energy receiver (ER). The signal broadcasted from the AS is received by both the ET and the ER. We study the design of wireless power transfer (WPT) from the ET to the ER, as illustrated in Fig. 2.1. In addition, a summary of the main mathematical symbols used in this chapter is given in Table 2.1.

The ER is a device (e.g., a sensor) that is capable of backscatter transmissions. It is composed of a single antenna element, a micro-controller, a variable impedance and an

Table 2.1: Summary of main mathematical symbols.

	Symbol	Description	Symbol	Description
System Parameters	η	Path-loss exponent	T_b	Duration of backscatter phase
	γ	Large scale channel attenuation	T_c	Chip duration (fixed backscatter coefficient)
	ζ	Backscatter coefficient	T_s	Duration of one ambient symbol
	m	Nakagami fading parameter	T_{off}	Duration of offset mismatch at correlator
	σ_n^2	Variance of AWGN	M	No. of antennas at ET
	d_1	Distance between AS and ER	N_c	No. of chips during backscatter phase
	d_2	Distance between ER and ET	N_s	No. of ambient signals /backscatter phase
	d_3	Distance between AS and ET	c_n	n-th chip in the training sequence
	P_s	Transmit power of AS	P_t	Transmit power of ET
RVs	s_i	i-th ambient symbol	$\mathbf{f}$	Channel from the ER to the ET
	g	Channel from the AS to the ER	$\mathbf{r}_{\text{ET}}$	Signal received at ET: backscatter phase
	$\mathbf{h}$	Channel from the AS to the ET	$\mathbf{r}_{\text{ER}}$	Signal received at ER: PT phase

energy harvester. We also assume that the ER is equipped with an ideal energy storage element (e.g., a supercapacitor) for storing the energy transferred by the ET. The block diagram of the ER is illustrated in Fig. 2.2a.

The ET is connected to the power grid and transmits with a fixed power P_t using a phased antenna array with M elements where M is large, which ensures that the ET forms a thin focussed beam. The block diagram of the ET is illustrated in Fig. 2.2b.

2.1.1 Channel Assumptions

We assume that all the channel links are composed of large-scale path loss, with exponent η. The block fading for all links is modelled as the independent and identically distributed (i.i.d.) Nakagami-m fading with m_g, m_f and m_h being the Nakagami-m parameters of the AS to ER, ER to ET and AS to ET channels respectively. We denote the distances between AS $\rightarrow$ ER, ER $\rightarrow$ ET and AS $\rightarrow$ ET by d_1, d_2 and d_3 respectively. Thus, large-scale attenuation is modelled as $\gamma_i = k_0(d_i/d_0)^{-\eta}$ where k_0 is the constant attenuation for path-loss at a reference distance of d_0 and $i \in \{1, 2, 3\}$.

The ER $\rightarrow$ ET, AS $\rightarrow$ ET and AS $\rightarrow$ ER fading channel coefficients, denoted by $\mathbf{f}$, $\mathbf{h}$ and g respectively, are modeled as quasi-static and frequency non-selective parameters. Consequently, the complex fading channel coefficient g is a circular symmetric complex Gaussian random variable with zero mean and unit variance. Similarly, $\mathbf{f}$ and $\mathbf{h}$ are also uncorrelated circularly symmetric complex Gaussian random vectors, i.e., $\mathbf{f} = [f_1, \ldots, f_M]^T \sim \mathcal{CN}(0, \boldsymbol{I}_M)$ and $\mathbf{h} = [h_1, \ldots, h_M]^T \sim \mathcal{CN}(0, \boldsymbol{I}_M)$. We make the following assumptions regarding the channels:

- The fading channel coefficients are assumed to be constant over the duration of one set of backscatter and power transfer phases, i.e., $T_b + T_p$ seconds and independent

and identically distributed from one $T_b + T_p$ slot to the next. The use of such channels is in line with the recent work in this research field [51, 53, 109].

- We assume channel reciprocity, i.e., the channel from ER $\rightarrow$ ET during the backscatter phase and the channel from ET $\rightarrow$ ER during the power transfer phase are constant and transpose of each other [38–43, 51].
- In this work, we do not need to make any channel state information (CSI) assumption at the ET or the ER, as the retrodirective WPT technique precludes the need for CSI at either ET or the ER.

2.1.2 Proposed Transmission Phases

The wireless power transfer from the ET to the ER takes place in two phases: (i) the backscatter phase and (ii) the power transfer phase, as shown in Fig. 2.1. During the first backscatter phase of duration T_b, the ER initiates a request for WPT by sending a backscattered ambient signal to the ET. During the second power transfer phase of duration T_p, the ET performs retrodirective energy beamforming towards the ER. Note that in this chapter we will study the effect of varying the backscatter phase duration T_b, while we assume unit time in the power transfer phase.

2.1.2.1 The Backscatter Phase

The backscattering at the ER is achieved by adapting the level of the antenna impedance mismatch, which affects the power of the reflected signal. During the backscatter phase of duration T_b seconds, the switch in Fig. 2.2a stays in position 1 and the ER backscatters the ambient signal given by $r_b(t) = \sqrt{\gamma_1} g \zeta s(t)$ where ζ is the backscatter reflection coefficient and $\sqrt{\gamma_1} g s(t)$ is the ambient signal arriving at the ER to be backscattered after suffering large scale attenuation γ_1 and channel coefficient g. In this work, we consider a BPSK-like backscatter coefficient having two different values, i.e., $\zeta = \pm 1$.[2] The backscatter training means that the tag backscatters the ambient signal while switching the backscatter coefficient N_c times[3] according to a pre-defined sequence between the values $+1$ and -1 at a rate of $\frac{1}{T_c}$, where T_c is the duration for which the backscatter coefficient maintains a certain value. This is effectively equivalent to multiplying the backscattered signal with a training signal $c(t)$ of N_c short duration pulses of amplitude

[2] ζ can assume any pair of values $|\zeta| \leq 1$. However, for simplicity we assume that $|\zeta| = 1$.

[3] In practice, the switching of the backscatter coefficient would be activated using an oscillator. The state-of-the art low power backscatter tags have internal oscillators that consume only tens of microwatts of power [58] and are feasible to be employed in our system model.

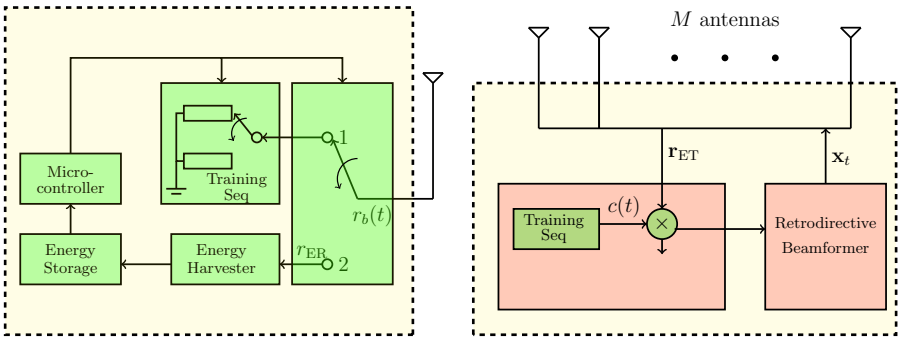

(a) The energy receiver (b) The energy transmitter

Figure 2.2: Block diagram of the energy transmitter and receiver.

$+1$ and -1. Thus, at a given time instant t, the backscattered signal from the ER is given by $r_b(t) = \sqrt{\gamma_1} g c(t) s(t)$, where γ_1, g and $s(t)$ are as given above and $c(t)$ is the training signal composed of a sequence of $+1$ and -1 pulses governed by the backscatter coefficient. This training sequence applied at the ER is quite similar to the DSSS [110][4]. Henceforth, we will also refer to the short duration pulses of switching the reflection coefficient as 'chips' and T_c as the chip duration due to the similarity of this scenario with DSSS.

The ET receives the composite signal consisting of the backscattered signal from the ER as well as the ambient signal and noise. The ET correlates this composite signal with the known training sequence $c(t)$. In this work, we assume perfect timing synchronization at the ET, in the baseline case. We then investigate the impact of imperfect synchronization in Section 2.5.

The purpose of using backscatter training is as follows. In general, the ambient signal is much stronger than the backscattered signal. This is because the latter suffers pathloss and attenuation twice and is orders of magnitude smaller than the former. The training performed at the ER before backscattering opens up a possibility for dealing with this issue of direct-link interference from the ambient signal at the ET. This is discussed in Section 2.4.

2.1.2.2 The Power Transfer Phase

During the power transfer phase, the ET provides retrodirective wireless power transfer to the ER. Specifically, the ET conjugates the phase of the de-spread signal and each

[4]The signal backscattered from the ER is spread in frequency. However, its in-band and out-of-band interference to the licensed users is negligible since it is very weak, i.e., it is being generated by ambient backscatter and not active transmission [1]

antenna at the ET sends a single-tone sinusoidal waveform towards the ER as shown in Fig. 2.2b. The phase and amplitude of this waveform are set according to the conjugated signal, subject to the maximum total transmit power P_t at the ET. The switch in the ER in Fig. 2.2a moves to position 2. Consequently, the ER stops backscattering and only harvests energy from the energy beam directed to it by the ET. This energy is stored in the energy storage device in the ER. Note that during the backscatter phase when the ER is backscattering the ambient signals, the energy harvester remains idle and can complete the rectification and storage of energy.

2.2 Signal Model

In this section, we present the signal equations that form the basis of analysis and design in the later sections. We adopt a continuous-time baseband signal model.

2.2.1 The Ambient Signal

For simplicity, similar to the previous works [109], we model the ambient signal as

$$s(t) = \sqrt{P_s} \sum_{i=1}^{\infty} s_i p_s(t - iT_s), \tag{2.1}$$

where i is the index of the ambient symbol and $s_i \sim \mathcal{CN}(0, 1)$ and $p_s(t)$ is a rectangular pulse of duration T_s given by

$$p_s(t) = \begin{cases} 1, & 0 \leq t \leq T_s \\ 0, & t > T_s. \end{cases} \tag{2.2}$$

Note that the power of an ambient symbol in (2.1) is P_s.

2.2.2 The Backscatter Phase

In the backscatter phase, as described in Section II, the backscattered signal from the ER is given by

$$r_b(t) = \sqrt{\gamma_1} g c(t) s(t), \tag{2.3}$$

where $c(t)$ is the training sequence with length N_c and chip duration T_c and g is the AS to ER fading channel coefficient. It can be modelled as

$$c(t) = \sum_{n=0}^{N_c-1} c_n p_c(t - nT_c), \tag{2.4}$$

where c_n is the n-th chip ($+1$ or -1) of the training sequence and $p_c(t)$ is a rectangular pulse of duration T_c, i.e.,

$$p_c(t) = \begin{cases} 1, & 0 \le t \le T_c \\ 0, & t > T_c. \end{cases} \tag{2.5}$$

The received signal at the ET is given by

$$\begin{aligned} \mathbf{r}_{\mathrm{ET}}(t) &= \sqrt{\gamma_2}\mathbf{f} r_b(t) + \sqrt{\gamma_3}\mathbf{h}s(t) + \mathbf{n}(t) \\ &= \sqrt{\gamma_1\gamma_2} g\mathbf{f}c(t)s(t) + \sqrt{\gamma_3}\mathbf{h}s(t) + \mathbf{n}(t), \end{aligned} \tag{2.6}$$

where $\mathbf{n}(t) \sim \mathcal{CN}(0, {\sigma_n}^2 \boldsymbol{I}_M)$ is the AWGN. Note that $\mathbf{r}_{\mathrm{ET}}(t)$ is a composite signal with three components, i.e., the backscattered signal from the ER, the ambient signal from the AS and the AWGN. The ET correlates this composite signal with the known training sequence with perfect frame synchronization to give

$$\begin{aligned} \mathbf{x}_r &= \frac{1}{N_c T_c} \int_0^{N_c T_c} \mathbf{r}_{\mathrm{ET}}(t)c(t)dt \\ &= \underbrace{\frac{1}{N_c T_c} \int_0^{N_c T_c} \sqrt{\gamma_1\gamma_2} g\mathbf{f}c(t)s(t)c(t)dt}_{\mathbf{x}_s} \\ &\quad + \underbrace{\frac{1}{N_c T_c} \int_0^{N_c T_c} \sqrt{\gamma_3}\mathbf{h}s(t)c(t)dt}_{\mathbf{x}_i} + \underbrace{\frac{1}{N_c T_c} \int_0^{N_c T_c} \mathbf{n}(t)c(t)dt}_{\bar{\mathbf{n}}}, \end{aligned} \tag{2.7}$$

where $\mathbf{x}_s$ and $\mathbf{x}_i$ are desired signal and undesired ambient (i.e., interference) components at the output of the correlator. Substituting the value of $c(t)$ from (2.4), we get $\mathbf{x}_s$ and $\mathbf{x}_i$ as

$$\mathbf{x}_s = \frac{\sqrt{\gamma_1\gamma_2} g\mathbf{f}}{N_c T_c} \int_0^{N_c T_c} s(t) \sum_{n=0}^{N_c-1} c_n p_c(t - nT_c) \sum_{m=0}^{N_c-1} c_m p_c(t - mT_c)dt,$$

$$= \frac{\sqrt{\gamma_1\gamma_2}g\mathbf{f}}{N_cT_c} \int_0^{N_cT_c} \sum_{n=0}^{N_c-1} c_n^2 s(t) {p_c}^2(t-nT_c)dt. \tag{2.8}$$

$$\mathbf{x}_i = \frac{1}{N_cT_c} \int_0^{N_cT_c} \sqrt{\gamma_3} s(t)c(t)\mathbf{h}dt,$$

$$= \frac{\sqrt{\gamma_3}\mathbf{h}}{N_cT_c} \int_0^{N_cT_c} s(t) \sum_{n=0}^{N_c-1} c_n p_c(t-nT_c)dt. \tag{2.9}$$

2.2.3 Power Transfer Phase

Once the received signal is correlated with the local copy of the training sequence, the phase of the signal at the output of the correlator in (2.7) is conjugated in accordance with the principle of retrodirective WPT. This conjugate signal then controls the phase and amplitude of ET's energy signal subject to the maximum total transmit power P_t at the ET. It is given as in [51],

$$\mathbf{x}_t = \sqrt{P_t}\frac{(\mathbf{x}_r)^*}{\|\mathbf{x}_r\|}, \tag{2.10}$$

where $\|\mathbf{x}_r\| = \sqrt{{\mathbf{x}_r}^T\mathbf{x}_r}$. Note that in (2.10), we have dropped the time index t because the baseband signal x_t does not vary with time. The signal received by the ER in the power transfer phase is given by

$$r_{\text{ER}} = \sqrt{\gamma_2}\mathbf{f}^T\mathbf{x}_t,$$
$$= \sqrt{\gamma_2 P_t}\frac{\left(\mathbf{f}^T{\mathbf{x}_s}^* + \mathbf{f}^T{\mathbf{x}_i}^* + \mathbf{f}^T\widetilde{\mathbf{n}}^*\right)}{\|\mathbf{x}_s + \mathbf{x}_i + \widetilde{\mathbf{n}}\|}, \tag{2.11}$$

where $\mathbf{x}_s$ is given in (2.8), $\mathbf{x}_i$ is given in (2.9) and $\widetilde{\mathbf{n}} \sim \mathcal{CN}(0, \frac{{\sigma_n}^2}{N_cT_c}\boldsymbol{I}_M)$ is the noise at the output of the matched filter. Note that the receiver noise at the ER is not included in (2.11) because it is irrelevant to energy harvesting.

2.2.4 Non-linear Energy Harvester

In this work, we have assumed that the ER is equipped with a non-linear energy harvester modelled as follows [111–113]. Assuming that the incident RF power on the ER is $Q_{RF} = |r_{\text{ER}}|^2$, where r_{ER} is the received signal at the ER during power transfer phase as given in (2.11), the instantaneous harvested power by the energy harvester in the ER

is given by

$$Q = \frac{\frac{c_0}{1+\exp(-a_0(Q_{RF}-b_0))} - \frac{c_0}{1+\exp(a_0 b_0)}}{1 - \frac{1}{1+\exp(a_0 b_0)}}, \tag{2.12}$$

where the parameters a_0, b_0 and c_0 respectively reflect the nonlinear charging rate with respect to the input power, the minimum turn-on voltage and the maximal harvested power when the energy harvester is drawn into saturation.

2.2.5 Metric

In this work, we use the average harvested power at the ER, $\overline{Q}$, as the figure of merit. It is defined as

$$\overline{Q} = E[Q], \tag{2.13}$$

where Q is the instantaneous harvested power given by (2.12).[5].

2.3 Analysis of Energy Harvested with a PN Sequence

In this section, we discuss the ambient backscatter training performed at the ER. As explained before, the ET receives a backscattered ambient signal from the ER. In addition to this, the ET also receives the original ambient signal which is orders of magnitude stronger than its backscattered version from the ER. As a result, the signal received at the ET during the backscatter phase is predominantly composed of the ambient component.

This problem of recovering the weak backscatter signal in the presence of a much stronger unwanted ambient signal is quite similar to the signal recovery problem in DSSS. Taking inspiration from that, we consider a pseudo-noise (PN) training sequence at the ER when backscattering, i.e., the backscatter coefficient is switched between $+1$ and -1 in a pseudo-random fashion. By doing this, we expect to capitalize on the spreading gain and boost the backscatter signal against the direct-link ambient interference. In order to assess this technique and the impact of the spreading gain, we evaluate the power harvested at the ER during the power transfer phase of this scheme. We assume that the number of ambient symbols in the backscatter phase is N_s, i.e., $T_b = N_s T_s = N_c T_c$.

[5]In this work, we assume unit time in the power transfer phase. Hence, we use the terms energy and power interchangeably

We analyze the expressions for the desired signal component and the undesired ambient component to find the energy harvested by the ER in the following two cases: (i) $N_s \leq N_c$ and (ii) $N_s \geq N_c$. The main result is presented in the proposition below.

Proposition 2.1 *For the system model considered in Section 2.1 with Nakagami-m fading channels when the number of antennas at the ET $M \to \infty$, the incident RF power on the ER is given by,*

$$Q_{RF} = \begin{cases} \gamma_2 P_t \left(\dfrac{\gamma_1\gamma_2|g|^2\mu\left(M+\dfrac{1}{m_f}\right)+\gamma_3\nu\left(\dfrac{N_s}{N_c}\right)^2+\dfrac{\sigma_n^2 N_s}{T_s P_s}}{\gamma_1\gamma_2|g|^2\mu+\gamma_3\nu\left(\dfrac{N_s}{N_c}\right)^2+\dfrac{\sigma_n^2 N_s}{T_s P_s}} \right) & \text{if } N_s \leq N_c \\ \gamma_2 P_t \left(\dfrac{\gamma_1\gamma_2|g|^2\mu\left(M+\dfrac{1}{m_f}\right)+\gamma_3\nu+\dfrac{\sigma_n^2 N_s}{T_s P_s}}{\gamma_1\gamma_2|g|^2\mu+\gamma_3\nu+\dfrac{\sigma_n^2 N_s}{T_s P_s}} \right) & \text{if } N_s \geq N_c \end{cases} \tag{2.14}$$

where

$$\mu = \left| \sum_{i=1}^{N_s} s_i \right|^2 = \left| \sum_{i=1}^{N_s} s_i^* \right|^2, \tag{2.15}$$

$$\nu = \left| \sum_{i=1}^{N_s} \sum_{n=\frac{N_c}{N_s}(i-1)}^{\frac{N_c}{N_s}i-1} c_n s_i^* \right|^2 = \left| \sum_{i=1}^{N_s} \sum_{n=\frac{N_c}{N_s}(i-1)}^{\frac{N_c}{N_s}i-1} c_n s_i \right|^2, \tag{2.16}$$

for simplicity. Substituting this value of Q_{RF} in (2.12)*, we get the instantaneous harvested power at the ER, from which the average harvested power is calculated according to* (2.13)*.*

Proof: See Appendix A.1.

The general expression for the instantaneous harvested power in (2.14) has two mutually dependent random variables μ and ν, in addition to g, $\mathbf{f}$ and $\mathbf{h}$. In addition, due to the nonlinear nature of the energy harvester, the overall expression for Q in (2.13) is fairly complex. Therefore, it is not possible to obtain a closed form expression for the expected value of harvested power. However, we can easily find the average harvested power by numerically taking the average of (2.14) substituted in (2.12) over a large number of Monte carlo realizations. Our simulation results in Section 2.6 confirm the accuracy of

this approach.

We have presented the average harvested power for the two possible cases of $N_s \leq N_c$ and $N_s \geq N_c$ in (2.14). However, we will show in Fig. 2.4 in Section 2.6 that the harvested power becomes very low with increasing values of N_s. As N_s exceeds N_c, the average harvested power stays perpetually low. This is due to the fact that the proposed scheme depends upon the variation of the backscatter coefficient during each ambient symbol that is backscattered. Therefore, from this point onwards, we only consider the case $N_s \leq N_c$.

From the results in Fig. 2.4 in Section 2.6.1, the main conclusion is that even with the training sequence at work, the value of average harvested power is very small and it actually decreases with the increase of training duration. This is due to the fact that the ambient signal is orders of magnitude stronger than the backscattered signal. The spreading gain of the training sequence employed is not sufficient to boost the backscatter signal significantly against the ambient signal. Thus, during the power transfer phase, most of the energy transmitted by the ET effectively leaks towards the AS. Since the PN-sequence approach for training design fails to boost up the backscattered signal in the presence of the strong ambient interference, another approach of training sequence design is considered in the next section, that directly looks at eliminating the ambient interference. This new scheme relies on the variation of the backscatter coefficient between ± 1 during each ambient symbol.

2.4 The Proposed Training Sequence Design

As mentioned in the previous section, the purpose of employing backscatter training was to enable the ET to differentiate the backscattered transmission from the ambient signal. However, since the backscattered signal is orders of magnitude weaker than the ambient interference and the DSSS approach cannot boost up the backscatter signal, the only option left is to directly cancel or significantly suppress the ambient interference. In the following, we propose a scheme to remove the direct-link interference from the AS.

Design Criterion: For the system model considered in Section 2.1, the ambient component can be eliminated at the output of the correlator in the ET if for each ambient symbol that is backscattered from the ER during the backscatter phase, the number of $+1$ and -1 chips is equal, i.e., $N_{+1} = N_{-1}$ and $N_{+1} + N_{-1} = \frac{N_c}{N_s}$, where N_{+1} and N_{-1} are the number of positive and negative chips respectively that are multiplied per symbol of the ambient source. This means that the backscatter coefficient is switched between $+1$ and -1 an even number of times, i.e., $N_c = 2kN_s$ where k is a positive integer, i.e.,

$k \in \{1, 2, \cdots\}$.

We justify the above design criterion as follows: In this case, $c(t)$ is a deterministic sequence of equal number of $+1$ and -1 chips instead of a PN sequence. Any sequence with equal number of $+1$ and -1 chips applied to each ambient symbol while backscattering, does the job. So we consider the expressions for $\mathbf{x}_\mathrm{s}$ and $\mathbf{x}_\mathrm{i}$, which are the expanded forms of (2.8) and (2.9) for $N_s \leq N_c$ (as derived in the Appendix), and are given below

$$\mathbf{x}_s = \sqrt{\gamma_1 \gamma_2 P_s} \frac{g\mathbf{f}}{N_s} \sum_{i=1}^{N_s} s_i. \tag{2.17}$$

$$\mathbf{x}_i = \sqrt{\gamma_3 P_s} \frac{\mathbf{h}}{N_c} \sum_{i=1}^{N_s} s_i \sum_{n=\frac{N_c}{N_s}(i-1)}^{\frac{N_c}{N_s}i-1} c_n. \tag{2.18}$$

We can see from (2.17) that, the desired backscattered component at the output of the correlator $\mathbf{x}_\mathrm{s}$ does not depend on the attributes of the training sequence, i.e., how the backscatter coefficient is changed. Therefore, it remains the same as in the previous case. However, with our proposed training sequence satisfying the *design criterion*, (2.18) becomes

$$\begin{aligned} \mathbf{x}_i &= \sqrt{\gamma_3 P_s} \frac{\mathbf{h}}{N_c} \sum_{i=1}^{N_s} s_i \sum_{n=\frac{N_c}{N_s}(i-1)}^{\frac{N_c}{N_s}i-1} c_n, \\ &= \sqrt{\gamma_3 P_s} \frac{\mathbf{h}}{N_c} \sum_{i=1}^{N_s} s_i \left[(+1)N_{+1} + (-1)N_{-1}\right] = 0 \end{aligned} \tag{2.19}$$

since $N_{+1} = N_{-1}$. Thus, the ambient component at the output of the correlator cancels out.

The following remarks discuss important practical aspects related to the *design criterion*.

Remark 2.1 *The design criterion is generic, i.e., any sequence that satisfies the two properties can serve the purpose. Moreover, we have seen that once the ambient component is removed, having a greater number of chips does not affect the harvested energy. Therefore, taking into account the hardware implementation, it is best to have the minimum number of chips per ambient symbol period, i.e., $k = 1$ and $N_c = 2N_s$ or $T_c = \frac{T_\mathrm{s}}{2}$. This means that we can switch the backscatter coefficient only twice per ambient symbol,*

i.e., for each ambient symbol that is backscattered, the backscatter coefficient is kept $+1$ *for half of the ambient symbol duration and* -1 *for the other half.*

Remark 2.2 *It is interesting to see how this design criterion compares with the well-known training sequences commonly used in wireless communications, i.e., Maximal length sequences, Gold sequences, Walsh-Hadamard sequences and Kasami sequences. Out of these, only the Walsh-Hadamard sequences have equal number of* $+1$ *and* -1 *and hence satisfy the design criterion.*

Using the proposed sequence in the *design criterion*, we find the average harvested energy at the ER, which is presented in the proposition below.

Proposition 2.2 *For the system model considered in Section 2.1 with Nakagami-m fading channels and* $N_s \leq N_c$ *while employing the backscatter training scheme proposed in the design criterion, when the number of antennas at the ET* $M \to \infty$*, the incident RF power on the ER is given by*

$$Q_{RF} \approx \gamma_2 P_t \left(\frac{\gamma_1 \gamma_2 |g|^2 \mu \left(M + \frac{1}{m_f} \right) + \frac{\sigma_n^2 N_s}{T_s P_s}}{\gamma_1 \gamma_2 |g|^2 \mu + \frac{\sigma_n^2 N_s}{T_s P_s}} \right). \tag{2.20}$$

where μ *is as defined in* (2.15)*. Substituting this value of* Q_{RF} *in* (2.12)*, we get the instantaneous harvested power at the ER, from which the average harvested power is calculated according to* (2.13)*.*

Proof: The proof is similar to the procedure in Appendix A and is omitted for the sake of brevity. The following insight is gained from *Proposition 2.*

Remark 2.3 *As the proposed scheme completely removes the direct-link ambient interference, the term involving the random variable* ν *is removed from the expression of* Q_{RF}*. Thus, during the power transfer phase, the ET forms a focussed beam towards the ER with no energy leaking towards the AS. This leads to a significant improvement in the harvested energy. This is demonstrated in the numerical results in Section 2.6.*

2.5 Impact of Practical System Imperfections

In the previous section, we propose a training design, under the perfect synchronization assumption. However, in practice, if the ambient symbol duration is unknown or changes from the one for which the system is designed, it may lead to the loss of timing

synchronization at the correlator in the ET or unequal durations of $+1$ and -1 values of the backscatter coefficient at the ER. Consequently, the ambient signal may not be completely cancelled and the performance of the system in terms of average harvested power at the ER may be affected. In this regard, we analytically examine the impact of imperfect synchronization at the correlator in the following susbsection. Another important scenario is when the duration of the ambient symbol is unknown and therefore an even number of chips or backscatter coefficient changes do not fit in each ambient symbol. In this situation, it is difficult to present any analytical results. Hence, we will investigate its impact using simulations in Section 2.6.3.2. Lastly, we discuss the effect other interference from neighbouring ambient sources in this section.

2.5.1 Imperfect synchronization at the correlator

The analysis in Section 2.4 assumes perfect synchronization. In this sub-section, we consider the case when an integer number of ambient symbols fit in the duration of the backscatter phase, but there is a misalignment between the received signal at ET and the locally generated training sequence during the backscatter phase. We model this misalignment as a time offset T_{off}.

2.5.1.1 Effect of offset on the desired signal component

We assume that the timing offset $T_{\text{off}} < T_c$. This is shown in Fig. 2.3. In this case, the desired component at the output of the correlator in (2.8) becomes

$$\begin{aligned}
\mathbf{x}_s &= \frac{\sqrt{\gamma_2\gamma_1}g\mathbf{f}}{N_cT_c}\int_0^{N_cT_c}\sum_{n=0}^{N_c-1} s(t)c_np_c(t-nT_c) \\
&\quad \sum_{m=0}^{N_c-1} c_mp_c(t-T_{\text{off}}-mT_c)dt, \\
&\overset{(a)}{=} \sqrt{\gamma_1\gamma_2P_s}\frac{g\mathbf{f}}{N_cT_c}\sum_{i=1}^{N_s} s_i\frac{N_c}{N_s}\left(\int_0^{T_{\text{off}}} -1dt + \int_{T_{\text{off}}}^{T_c} 1dt\right), \\
&= \sqrt{\gamma_1\gamma_2P_s}\frac{g\mathbf{f}}{N_cT_c}\sum_{i=1}^{N_s} s_i\frac{N_c}{N_s}\left(-2T_{\text{off}}+T_c\right), \\
&= \sqrt{\gamma_1\gamma_2P_s}\frac{g\mathbf{f}}{N_s}\sum_{i=1}^{N_s} s_i\left(1-2\frac{T_{\text{off}}}{T_c}\right),
\end{aligned} \tag{2.21}$$

where (a) splits the overall integration into intervals over each symbol.

Comparing (2.8) and (2.21) above we get for $T_{\text{off}} \leq T_c$

$$\mathbf{x}_{s(\text{misaligned})} = \left(1 - 2\frac{T_{\text{off}}}{T_c}\right) \mathbf{x}_{s(\text{sychronized})}. \tag{2.22}$$

Similarly, it can be shown that for $T_c < T_{\text{off}} \leq 2T_c$,

$$\mathbf{x}_{s(\text{misaligned})} = \left(2\frac{T_{\text{off}}}{T_c} - 1\right) \mathbf{x}_{s(\text{sychronized})}. \tag{2.23}$$

Thus, we can see that if the synchronization is not perfect, the desired backscatter component is a fraction of the fully synchronized case.

2.5.1.2 Effect of offset on the undesired ambient component

Again assuming that the timing offset $T_{\text{off}} < T_c$, the undesired ambient component from (2.9) at the output of the correlator becomes,

$$\begin{aligned}
\mathbf{x}_i &= \frac{\sqrt{\gamma_3}\mathbf{h}}{N_c T_c} \int_0^{N_c T_c} \sum_{m=0}^{N_c-1} c_m p_c(t - T_{\text{off}} - nT_c) s(t) dt, \\
&= \frac{\sqrt{\gamma_3 P_s}\mathbf{h}}{N_c T_c} \int_0^{N_c T_c} \sum_{m=0}^{N_c-1} c_m p_c(t - T_{\text{off}} - nT_c) \sum_{i=1}^{S} s_i p_s(t - iT_s) dt, \\
&= \sqrt{\gamma_3 P_s} \frac{\mathbf{h}}{N_c T_c} \sum_{i=1}^{N_s} s_i \\
&\left(\int_0^{T_{\text{off}}} -1 dt + \int_{T_{\text{off}}}^{T_c} +1 dt + \int_{T_c}^{2T_c} -1 dt + \cdots + \int_{(\frac{N_c}{N_s}-1)T_c}^{\frac{N_c}{N_s}T_c - T_{\text{off}}} -1 dt \right), \\
&= \sqrt{\gamma_3 P_s} \frac{\mathbf{h}}{N_c T_c} \sum_{i=1}^{N_s} s_i \left(-T_{\text{off}} + T_c - T_c + T_c \cdots - T_c + T_{\text{off}}\right), \\
&= 0.
\end{aligned} \tag{2.24}$$

Note that the same result is obtained even when $T_{\text{off}} > T_c$.

As we have seen in the previous sub-section, the desired component is scaled down because of the offset in synchronization while the undesired component is still completely being eliminated. This change in the magnitude of the desired component is reflected in the energy harvested at the ER. *Therefore, we can conclude that the system can work reasonably well with a small timing offset. However good synchronization is needed for*

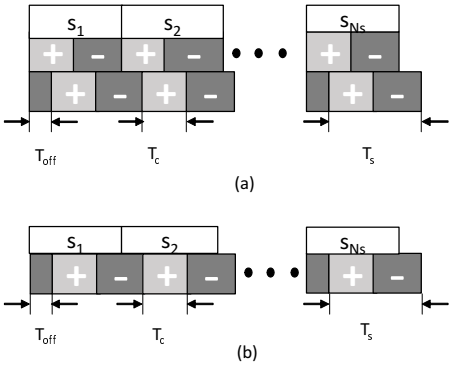

Figure 2.3: Misalignment between the backscattered signal and locally generated spreading sequence at the ET: (a) Effect on the backscatter component (b) Effect on the ambient component

best performance.

Using the above values of $\mathbf{x}_s$ and $\mathbf{x}_i$, the incident RF power at the ER in case of misalignment at the ET can be shown to be given by

$$Q_{RF} \approx \gamma_2 P_t \left(\frac{\left|1 - \frac{2T_{\text{off}}}{T_c}\right|^2 \gamma_1\gamma_2|g|^2\mu \left(M + \frac{1}{m_f}\right) + \frac{\sigma_n^2 N_s}{T_s P_s}}{\gamma_1\gamma_2|g|^2\mu + \frac{\sigma_n^2 N_s}{T_s P_s}} \right). \tag{2.25}$$

which holds for all values of T_{off} except when $T_{\text{off}} = k\frac{T_c}{2}$, where k is an integer and $k \geq 0$. Substituting this value of Q_{RF} in (2.12), we get the instantaneous harvested power at the ER, from which the average harvested power is calculated according to (2.13).

2.5.2 Effect of other interference from neighbouring ambient sources

In this subsection, we consider the impact of interference on our system from neighbouring ambient sources. In particular, the application of the chipping sequence at the ET increases the bandwidth of the backscatter signal. Therefore, the ambient signals in neighbouring frequencies can potentially cause interference to the system.

The interference signal can be from a variety of sources and can even include the backscattered versions of these interference signals. Compared with the interference signals directly received at the ET, their backscattered versions have much weaker strength (by several orders of magnitude) when they reach the ET. Therefore, we only consider the directly received interference signals. In this work, we have assumed the original ambient signal to follow a normal distribution, since the ambient signal may come from a variety

of sources and is usually random. Therefore, we assume that the aggregate interference signal from other ambient sources in the same environment follows a zero-mean circularly symmetric complex Gaussian distribution [9, 109], i.e., $\mathbf{u}_i(t) \sim \mathcal{CN}(0, {\sigma_i}^2 \boldsymbol{I}_M)$ where ${\sigma_i}^2$ is the received interference power.

The expression in (2.6) for the received signal at the ET thus becomes,

$$\mathbf{r}_{\mathrm{ET}}(t) = \sqrt{\gamma_1\gamma_2} g \mathbf{f} c(t) s(t) + \sqrt{\gamma_3}\mathbf{h} s(t) + \mathbf{u}_i(t) + \mathbf{n}(t), \tag{2.26}$$

As the ET correlates this composite signal with the known training sequence we get,

$$\begin{aligned}\mathbf{x}_r = &\underbrace{\frac{\sqrt{\gamma_2}\mathbf{f}}{N_c T_c}\int_0^{N_c T_c} \sqrt{\gamma_1} g c(t) s(t) c(t) dt}_{\mathbf{x}_s} + \underbrace{\frac{1}{N_c T_c}\int_0^{N_c T_c} \sqrt{\gamma_3}\mathbf{h} s(t) c(t) dt}_{\mathbf{x}_i} \\ &+ \underbrace{\frac{1}{N_c T_c}\int_0^{N_c T_c} \mathbf{u}_i(t) c(t) dt}_{\widetilde{\mathbf{u}}_\mathbf{i}} + \underbrace{\frac{1}{N_c T_c}\int_0^{N_c T_c} \mathbf{n}(t) c(t) dt}_{\widetilde{\mathbf{n}}},\end{aligned} \tag{2.27}$$

where $\mathbf{x}_s$ and $\mathbf{x}_i$ are desired signal and undesired primary ambient component and $\widetilde{\mathbf{u}}_\mathbf{i}$ is the interference component from the neighbouring ambient signals, with $\widetilde{\mathbf{u}}_\mathbf{i} \sim \mathcal{CN}(0, \frac{{\sigma_i}^2}{N_c T_c}\boldsymbol{I}_M)$ and $\widetilde{\mathbf{n}} \sim \mathcal{CN}(0, \frac{{\sigma_n}^2}{N_c T_c}\boldsymbol{I}_M)$ is the noise at the output of the matched filter.

Using (2.27), the signal received at the ER, previously given by (2.11) becomes,

$$r_{\mathrm{ER}} = \sqrt{\gamma_2}\mathbf{f}^T\mathbf{x}_t = \sqrt{\gamma_2 P_t}\frac{\left(\mathbf{f}^T{\mathbf{x}_s}^* + \mathbf{f}^T{\mathbf{x}_i}^* + \mathbf{f}^T\widetilde{\mathbf{u}}_\mathbf{i}^* + \mathbf{f}^T\widetilde{\mathbf{n}}^*\right)}{\|\mathbf{x}_s + \mathbf{x}_i + \widetilde{\mathbf{u}}_\mathbf{i} + \widetilde{\mathbf{n}}\|}, \tag{2.28}$$

where $\mathbf{x}_t = \sqrt{P_t}\frac{(\mathbf{x}_r)^*}{\|\mathbf{x}_r\|}$. Thus, the incident RF power at the ER with interference present can be shown to be given by,

$$Q_{RF} \approx \gamma_2 P_t \left(\frac{P_s\gamma_1\gamma_2|g|^2\mu\left(M + \frac{1}{m_f}\right) + P_s\gamma_3\nu\left(\frac{N_s}{N_c}\right)^2 + \frac{\sigma_i^2 N_s}{T_s} + \frac{\sigma_n^2 N_s}{T_s}}{P_s\gamma_1\gamma_2|g|^2\mu + P_s\gamma_3\nu\left(\frac{N_s}{N_c}\right)^2 + \frac{\sigma_i^2 N_s}{T_s} + \frac{\sigma_n^2 N_s}{T_s}} \right) \tag{2.29}$$

where ν is defined in (A.6) in the appendix. Substituting this value of Q_{RF} in (2.12), we get the instantaneous harvested power at the ER, from which the average harvested power is calculated according to (13). Generally, larger interference power leads to a degradation in the average harvested power, because our training design and interference cancellation is only targeted at the interference from the primary ambient signal, not the

secondary interference signals from neighbouring ambient sources. This is numerically investigated in Section 2.6.4.

2.6 Results

In this section we present the numerical and simulation results. In order to model a practical ambient backscatter scenario, we set the distances as follows: $d_1 = 200$ m, $d_2 = 10$ m, $d_3 = 200$ m [1]. The values of the rest of system parameters are: $d_0 = 1$ m, $k_0 = 0.001$, $M = 500$, $P_t = 1$ W, $P_s = 1$ W, $\sigma_n^2 = 10^{-18}$, $T_s = 5$ μs , $T_c = 500$ ns. For the non-linear energy harvester, we set $a_0 = 1500$, $b_0 = 0.0022$ and $c_0 = 24$ mW [112]. The choice of $T_c = 500$ ns ensures that multipath delay spread is negligible [21]. As mentioned in Section 2.1, we have assumed Nakagami-m fading on all channel links. However, we can see from (2.14) and (2.20) and that the final analytical result only depends upon m_f. Hence, for the sake of simplicity, we have considered $m_h = m_g = 1$ for the AS to ET and AS to ER links and $m_f = 1$ and $m_f = 10$ for the ER to ET link. We initially ignore the impact of other interference from neighbouring ambient signals, setting $\sigma_i = 0$ in Sections 2.6.1- 2.6.3, and then investigate the impact of such interference in Section 2.6.4.

2.6.1 Energy Harvested with a PN Sequence

Fig. 2.4 plots the average harvested power versus the duration of the backscatter phase, i.e., T_b with the ambient signal duration being $T_s = 5$ μs. These results are averaged over 10^4 Monte Carlo simulation trials. In each trial, a new pseudorandom sequence is generated and used. Note that for other practical values of system parameters, the average harvested power has very similar values and trend. Thus, we only show a single curve in Fig. 2.4.

The figure shows that there is a very good agreement between the analytical results in (2.14) and the simulation for $N_s \leq N_c$[6]. The figure also shows that the average harvested power is maximum around 15 μW when $N_s = 1$ and $T_b = 5$ μs. As N_s and hence T_b increase, the average harvested power quickly decreases and reaches a value of approximately 4 μW. Thus, we can conclude from Fig. 2.4 that the average harvested power is very small and it reduces further as the training period increases.

This latter observation is particularly counter-intuitive, since it is not expected to happen when using DSSS techniques. The reason for this trend is that the ambient signal

[6]A similar match is observed between the analytical result and the simulation for $N_s \geq N_c$ but the corresponding plots are not presented here due to the reason discussed in Section 2.3.

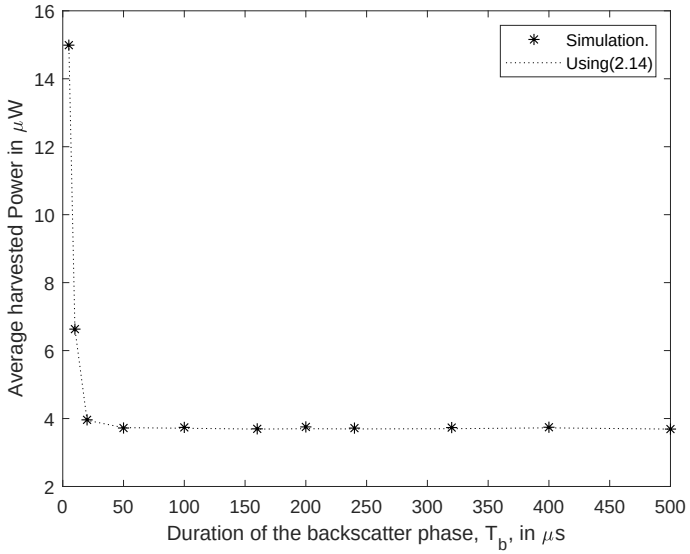

Figure 2.4: Average harvested power at the ER as a function of T_b (duration of the backscatter phase).

is orders of magnitude stronger than the backscattered signal. The spreading gain of the training sequence employed is not sufficient to boost the backscatter signal significantly against the ambient signal. In order to demonstrate this, Fig. 2.5 plots $\frac{|x_i|}{|x_s|}$, i.e., the ratio of the magnitudes of the undesired ambient component and the desired backscatter component at the output of the correlator versus the duration of the backscatter phase T_b. We can see from the figure that even with the training sequence in use, the ambient component is much stronger than the desired backscattered signal. Moreover, as the duration of the training phase increases, the ambient component becomes increasingly stronger. Thus, when the ET performs retrodirective WPT by taking the conjugate of the composite signal at the output of the correlator, the comparative strength of the ambient component is far greater than the backscattered one for larger durations of backscatter phase. Thus, most of the energy transmitted by the ET is still effectively leaking towards the AS and this situation becomes exacerbated for longer durations of backscatter phase due to the comparatively higher strength of the ambient component.

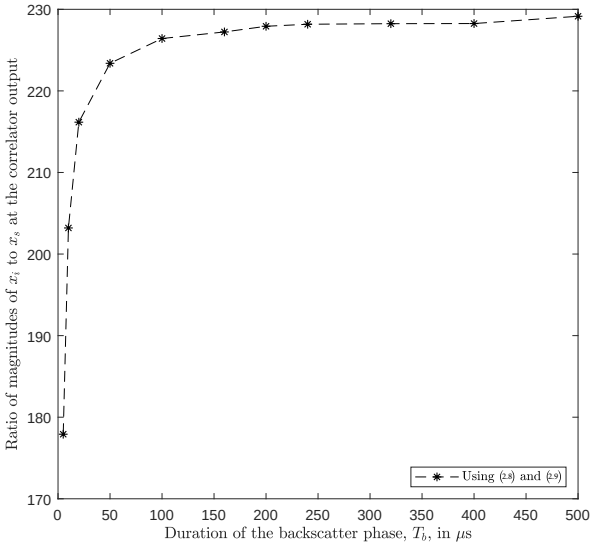

Figure 2.5: Ratio of magnitude of ambient and backscatter signal components at the output of the correlator plotted against T_b (duration of the backscatter phase).

2.6.2 Energy Harvested with the Proposed Ambient Backscatter Training Scheme

Using (2.20), (2.12) and (2.13), the average harvested energy at the ER is calculated and plotted in Fig. 2.6 for three different values of ambient symbol duration, i.e., $T_s = 5$ μs, $T_s = 10$ μs and $T_s = 20$ μs and two different values of Nakagami-m fading on the ET to ER link i.e. $m_f = 1$ and $m_f = 10$. The values of other system parameters are the same as stated in the beginning of this section for Fig. 2.4. Numerous features of the proposed scheme are evident from Fig. 2.6. Firstly, we can see that the result for $m_f = 1$ and $m_f = 10$ are quite similar. Thus, in this case, having a line of sight link between ET and ER does not significantly impact the results. Hence, in the remaining results, we only consider $m_f = 10$.

Secondly, comparing the $T_s = 5\mu s$ plot with Fig. 2.4, it can be observed that the energy harvested at the ER increases significantly as compared to the case when a pseudo-random sequence is employed at the ER during the backscatter phase. This is due to the fact that the proposed scheme completely eliminates the ambient component. As a result, during retrodirective WPT the ET forms a focused beam directed back at the ER alone, with no energy leaking to the AS. This clearly delineates the advantage of using the designed training sequence.

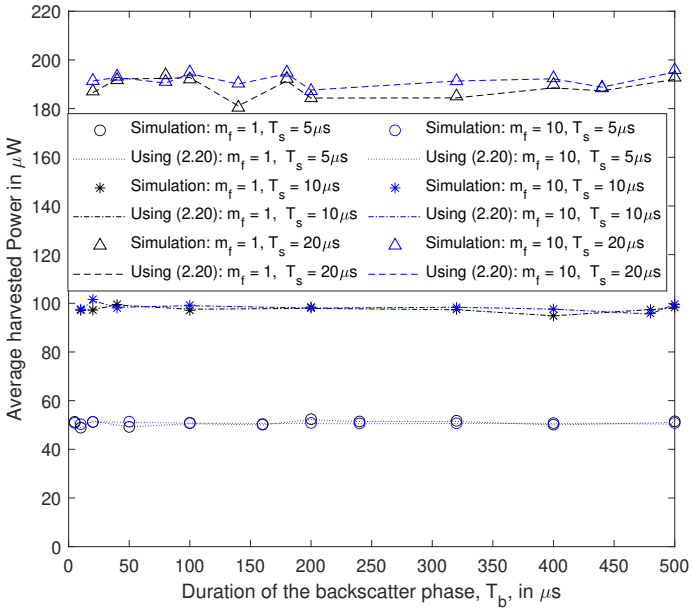

Figure 2.6: Average harvested power at the ER with the proposed sequence plotted against the duration of the backscatter phase, T_b.

Thirdly, the harvested power at the ER does not change with the increase in backscatter training duration T_b, but stays constant as long as the ambient symbol duration T_s stays constant. Specifically, when the system is designed with a fixed value of T_c, then for different values of N_s and hence T_b, the average harvested power at the ER now stays around 50 μW for $T_s = 5$ μs, 99 μW for $T_s = 10$ μs and 190 μW for $T_s = 20$ μs.

Fourthly, with the ambient component removed, the average harvested power depends largely on the duration of the ambient symbol T_s, as is evident from the plot with the average harvested power having a significantly larger value for $T_s = 20$ μs, compared to $T_s = 5$ μs

Lastly, it can also be inferred from the plot that for a fixed ambient source, the average harvested power in this case is independent of the number of chips N_c. Actually, for a fixed chip duration, the number of chips also increases with the increased backscatter period T_b and as we can see from Fig. 2.6, the average harvested power stays constant for the increased values of the backscatter period.

Fig. 2.7 presents the plots of average harvested power against the duration of backscatter phase T_b for different values of P_s, the power of the AS. We can see that the average harvested power is larger with higher values of P_s. This observation is consistent with

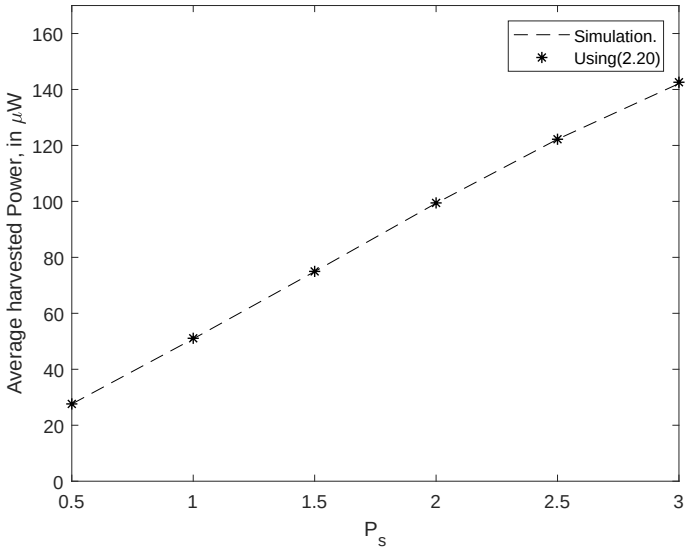

Figure 2.7: Average harvested power, $\overline{Q}$, plotted against transmit power of AS, P_s.

the analysis in Section 2.4. We can see from (2.17) that the desired backscatter component $\mathbf{x}_\mathrm{s}$ is directly proportional to the strength of the AS. Since the ambient component is now completely removed, a higher value of power is harvested on average at the ER when the AS is stronger. Similarly, Fig. 2.8 plots the average harvested power against M, the number of antennas at the ET. It can be observed that there is a good agreement again between the results obtained by simulation and by numerically averaging (2.20) for practical values of M.

2.6.3 Impact of Practical System Imperfections

2.6.3.1 Imperfect synchronization at the correlator

A plot of the average harvested power at the ER as a function of time offset between the received and locally generated signal is given in Fig. 2.9. The parameter values used are the same as for Fig. 2.6. For this plot we have taken $T_c = \frac{T_s}{2}$, as discussed in Remark 1 in Section 2.4. It can be seen from Fig. 2.9 that the average harvested power decreases for $kT_c \leq T_\mathrm{off} < k\frac{T_c}{2}$, achieving a local minimum at $T_\mathrm{off} = k\frac{T_c}{2}$ and then increases for $k\frac{T_c}{2} < T_\mathrm{off} \leq kT_c$. This reiterates that the system can work reasonably with a small offset, as discovered in Section 2.5.1.

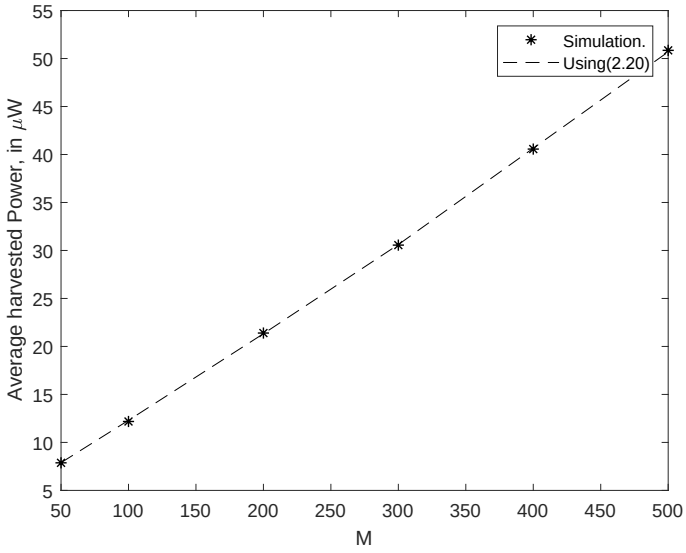

Figure 2.8: Average harvested power, $\overline{Q}$,
plotted against number of antennas at the ET M.

2.6.3.2 Effect of unknown ambient symbol duration

In this subsection, we consider the scenario in which the system is designed for an ambient symbol duration T_s. However, when the system is actually deployed, the available ambient symbol has a different duration, i.e., T_s'. Fig. 2.10 plots the average harvested power at the ER versus the number of ambient symbols that fit in the backscatter phase duration of T_b seconds for training sequences that satisfy the *design criterion* but have different number of chips, i.e., $\frac{N_c}{N_s} = 2, 10$ and 40. This system was originally designed for the following values: $T_b = 200$ μs, $N_c = 400$, $T_c = 500$ ns, $T_s = 5$ μs, $N_s = 10$, $m_g = m_h = 1$ and $m_f = 10$. We plot the average harvested power at the ER for a range of values of $N_s' = \{6, 7, 8, 9, 10, 11, 12, 13, 14, 15\}$ and the corresponding T_s'.

We can see from Fig. 2.10 that the training sequence with the least number of chips per symbol gives the worst performance, i.e., as the number of the ambient symbols in the backscatter phase deviates from designed value, the average harvested power drops to a fraction of a μW. This is due to the fact that the ambient component is no longer completely cancelled as the ER was designed to switch the backscatter coefficient at $\frac{T_s}{2}$, so that each ambient symbol was multiplied by $+1$ and -1 for alternate halves of its duration. However, in the new scenario, a switch at $\frac{T_s'}{2}$ is required. Consequently, the ambient component is not eliminated completely; rather a fraction from each ambient

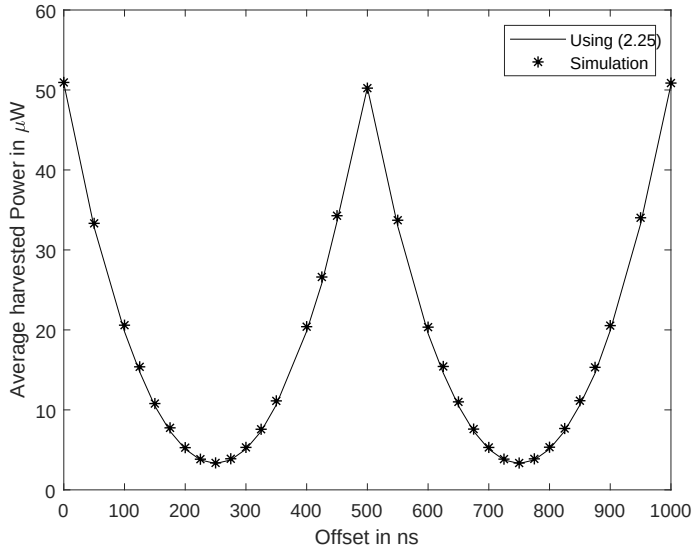

Figure 2.9: Average harvested power at the ER plotted against the offset between incoming and locally generated signal at the correlator.

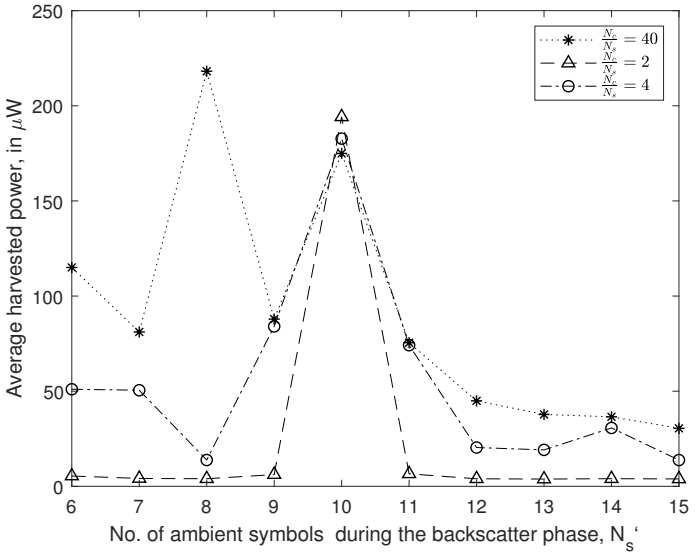

Figure 2.10: Average harvested power at the ER plotted against the number of ambient symbols during the backscatter phase when the actual ambient symbol duration is different from the designed value.

symbol remains that contributes to a residual ambient component at the output of the correlator. This, in turn leads to a significant amount of power leaking to the AS.

It can be further noted from the figure that the point where all the three curves meet, i.e., $N_s' = 10$ corresponds to the ideal scenario when the number of ambient symbols fitting within the backscatter phase is precisely 10, i.e., the value for which the system is designed. Therefore, regardless of the ratio of N_c/N_s, as long as the number of ambient symbols in the backscatter phase is equal to the value for which the system is designed, we receive the best performance, i.e., maximum value of average harvested energy.

Another vital observation from Fig. 2.10 is that as the number of chips per ambient symbol increase, better performance can be obtained. For instance, the curve with the largest number of chips per symbol, i.e., $\frac{N_c}{N_s} = 40$ performs relatively better than the other two cases for moderate mismatch in symbol duration. The reason for this behaviour is that the fraction of ambient component that is not cancelled due to the unknown value of T_s depends upon the chip duration T_c. Therefore, in spite of the fact that an even number of chips may not fit in one ambient symbol (leading to imperfect cancellation), by increasing the switching rate of the backscatter coefficient and thereby decreasing the chip duration T_c, the un-cancelled fraction of a chip can be reduced and hence a smaller ambient component remains at the output of the correlator. In this way, there is less leakage towards the AS and the ER is able to harvest more power. *Thus, when the ambient symbol duration is unknown, a faster switching rate can help to minimize the effect of uncancelled ambient for moderate mismatch of symbol duration.*

2.6.4 Effect of other interference from neighbouring ambient sources

Fig. 2.11 plots the average harvested power at the ER versus the ratio of the average received power from the direct-link AS and the received interference power from neighbouring sources σ_i^2. This ratio is expressed in dB. For this plot, we have taken $T_s = 20$ μs and $N_s = 4$ while all the other system parameters are kept the same as for Fig. 2.6. It can be seen that the average harvested power is 7.09 μW when this ratio is 20 dB. However, when this ratio increases to 30 dB and 40 dB, the average harvested power jumps to tens and hundreds of μW respectively, finally approaching the value of over 180 μW for 50 dB, very close to that can be achieved when there is no interference. Therefore, if the interference signal is significantly weaker than the original ambient signal, our system can harvest tens to hundreds of μW of power.

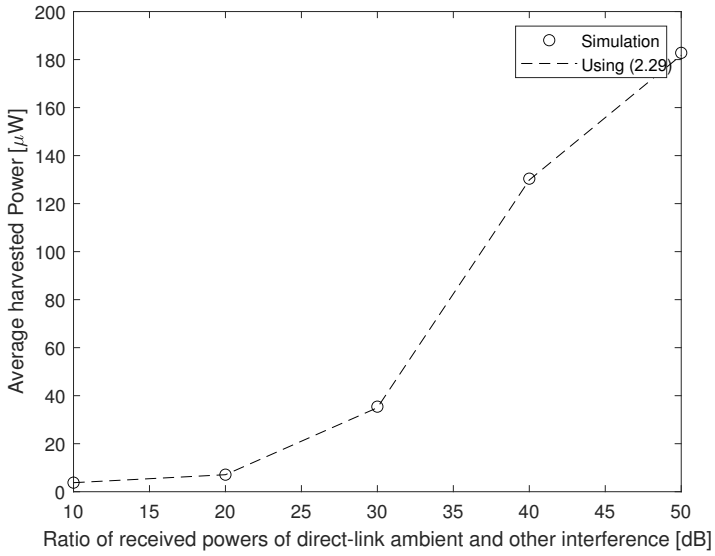

Figure 2.11: Average harvested power at the ER versus the ratio of the average received power from the direct-link ambient and the average interference power from neighbouring ambient sources.

2.7 Conclusions and Future Work

In this chapter, we have presented a wireless power transfer scheme to energize an ER using retrodirective WPT at the ET and ambient backscatter at the ER. To deal with the direct-link ambient interference, we have proposed the approach of backscatter training, i.e., the pattern of varying the reflection coefficient at the ER to completely eliminate the strong direct-link ambient interference. We have showed that when the ambient symbol duration is known, the switching rate does not matter and we can switch the backscatter coefficient only twice per ambient symbol period. When the ambient symbol duration is unknown, then switching at a faster rate helps to minimize the effect of the uncancelled ambient and boost the harvested power. The best average harvested power is achieved when the interference signal from neighbouring ambient sources is significantly weaker than the original ambient signal. The scheme proposed in this paper can be extended to multiple backscatter tags located in an area by assigning the mutually orthogonal Walsh-Hadamard sequences to individual ERs and considering scheduling or collision resolution schemes. This is outside the scope of this chapter and can be considered in future work. Another interesting direction for future work is to study the distribution of the harvested energy, which may be relevant for particular use cases.

Chapter 3

Design of Intelligent Reflecting Surface (IRS)-boosted Ambient Backscatter Systems

Despite the research efforts in the area of Ambient BackCom, the reliability in terms of bit error rate (BER) of such systems is still limited. This is due to the fact that the BackCom signal suffers double fading and when it arrives at the backscatter receiver, it is very weak as compared to the ambient signal from the original RF source, also known as direct-link interference (DLI). The DLI is an unknown, already modulated signal, much stronger than the information signal of interest from the BD. It has been shown that, even in line-of-sight (LOS), the DLI and the ambient BackCom signal can combine such that the received signals corresponding to bit '0' and bit '1' differ only in phase, but have very close values in terms of power. In such a scenario, the ED performs poorly and BER is high.

To improve the performance of the ED, it is imperative to strengthen the backscatter signal and also to maximize the contrast between the received powers at the ED corresponding to bit '0' and '1'. In this work, we study a general IRS-aided ambient backscatter scenario. We propose a novel scheme to address the fundamental aspect of improving the detection of ambient backscatter signal at the RX. We accomplish this by designing the IRS phase shifts to improve backscatter signal strength and performing eigenvector beamforming (EBF) assisted energy detection at the RX to maximize the ratio of the two received energies. Our results clearly show that an IRS of reasonable size can considerably improve the BER performance of ambient BackCom, which is an important improvement for low-power IoT systems.

The rest of this chapter is organized as follows. Section 3.1 describes the system model and assumptions. Section 3.2 presents the signal model of the system in terms of mathematical equations. Section 3.3 presents the proposed scheme and the associated optimization problems. Section 3.4 solves the optimization problem. Section 3.5 presents and discusses the numerical results. Finally, Section 3.6 concludes the chapter.

3.1 System Model

We consider a system in which an IRS with N passive reflecting elements is deployed to assist a BD to communicate to a RX by backscattering ambient signals from an ambient source (AS). We model the system in a three dimensional setup as shown in Fig. 3.1. The location coordinates of the IRS, AS, BD and the RX are $(0, 0, l_z^{\mathrm{I}})$, $(l_x^{\mathrm{A}}, l_y^{\mathrm{A}}, l_z^{\mathrm{A}})$, $(l_x^{\mathrm{B}}, l_y^{\mathrm{B}}, 0)$ and $(l_x^{\mathrm{R}}, l_y^{\mathrm{R}}, 0)$ respectively. The distance among the system components is represented by d_{i-j} and the corresponding pathloss as β_{i-j}, where i and j represent the respective components of the system. Note that for the links through the IRS, the pathloss of the two links (to and from IRS) is lumped into a single constant, e.g., $\beta_{\text{A-I-R}}$ is the pathloss associated with the AS to IRS to RX link [15].

The BD is a single-antenna device whereas the RX has M antennas. The IRS is equipped with its own power supply and a smart controller, which is connected with the RX via a separate reliable wireless link and is responsible for coordinating their operation as well as exchanging information such as reflection coefficients and channel state information (CSI). We assume perfect CSI knowledge [85] as CSI acquisition is beyond the scope of this work and should be addressed separately.[1] As the BD performs diffuse reflection, we ignore the signals reflected two or more times at the BD due to severe power loss [115]. However, for the paths in which IRS is involved, we also consider the signals that undergo two reflections at the IRS, i.e., the signal going through the AS-IRS-BD-IRS-RX link, that undergoes reflection at IRS before as well as after getting backscattered by the BD, which is a unique feature of this system. The IRS can increase overall signal strength at the RX by adjusting its phase shifts to balance the signal strengths between the AS-BD and BD-RX direct and via IRS links [82].

We assume all the channels to be quasi-static, frequency non-selective and constant in each fading block. The small-scale fading for all links is modelled as independent

[1] In practice, CSI can be estimated at the RX by adapting the channel estimation methods for the IRS systems or by using deep learning [114]. In particular for our system model, channel estimation can be carried out by turning only two nodes in our system model ON at a time and estimating the relevant channels. Thus, CSI is acquired by going pair-wise among all the nodes in the system till all of the available channels are obtained.

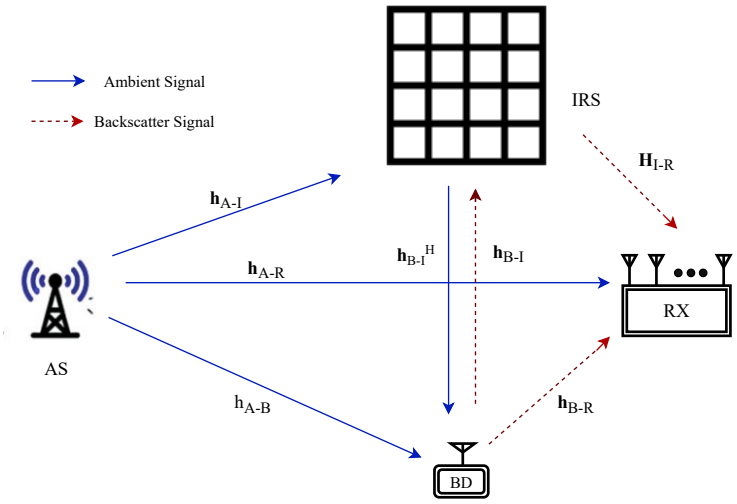

Figure 3.1: Illustration of the system model

and identically distributed (i.i.d.) Nakagami-m fading due to its mathematical tractability [116] and because it can be used to model Rayleigh as well as Rician distributions as special cases for $m = 1$ and $m \geq 1$ [117]. This channel model allows a flexible evaluation and is commonly adopted in research works on ambient backscatter as well as on IRS [118–120]. Let the channels from the AS, BD and RX to the IRS be represented by $\mathbf{h}_{\text{A-I}} \in \mathbb{C}^{N\times 1}$, $\mathbf{h}_{\text{B-I}} \in \mathbb{C}^{N\times 1}$ and $\mathbf{H}_{\text{R-I}} \in \mathbb{C}^{N\times M}$ respectively. Similarly, the channels from the AS to the BD and the RX are represented by $h_{\text{A-B}} \in \mathbb{C}^{1\times 1}$ and $\mathbf{h}_{\text{A-R}} \in \mathbb{C}^{M\times 1}$ respectively, while the channel from the BD to the RX is represented by $\mathbf{h}_{\text{B-R}} \in \mathbb{C}^{M\times 1}$.

3.2 Signal Model

The ambient signal is independent and identically distributed at different time instants, and follows the CSCG distribution. Let s_n be the n^{th} ambient symbol that is backscattered, i.e., $s_n \sim \mathcal{CN}(0, P_s)$ where P_s is the transmit power of the AS. The signal received at the BD is a sum of the n^{th} symbol directly from the AS and its reflection from the IRS and is given by

$$r_n = \left(h_{\text{A-B}} + \mathbf{h}_{\text{B-I}}^{H} \boldsymbol{\Theta} \mathbf{h}_{\text{A-I}}\right) s_n, \tag{3.1}$$

where $\mathbf{h}_{\text{B-I}}$ and $\mathbf{h}_{\text{A-I}}$ are $N \times 1$ vectors and $\boldsymbol{\Theta}$ is the $N \times N$ matrix of phase shift values at the IRS such that $\boldsymbol{\Theta} = \text{diag}(e^{j\theta_1}, \cdots, e^{j\theta_N})$ and θ_n being the phase shifts of individual

elements of the IRS with $\theta_n \in [0, 2\pi)$, $\forall n$.

The BD modulates its information bits over the ambient signals by changing its antenna impedance. We adopt on–off keying at the BD, which means that the ambient signal is fully reflected when bit '1' is transmitted and there is no reflection when bit '0' is transmitted. Thus, if we denote the BD's symbol as b, we have $b \in \{0, 1\}$. Since the backscatter link is typically weaker than the direct link, the BD transmits at a much lower rate than that of the AS [62]. We assume that the BD symbol b remains unchanged for S consecutive ambient symbols. So S can be taken as the backscatter symbol length. Thus, during one BD symbol period, the backscattered signal from the BD to the RX is given by

$$x_n = \left(\sqrt{\beta_{\text{A-B}}} h_{\text{A-B}} + \sqrt{\beta_{\text{A-I-B}}} \mathbf{h}_{\text{B-I}}^H \mathbf{\Theta} \mathbf{h}_{\text{A-I}}\right) b s_n, \tag{3.2}$$

where s_n is the n^{th} ambient symbol. At the RX, the signal backscattered from the BD arrives by two paths i.e., directly and also after reflection from the IRS. Simultaneously, the original ambient signal from the AS reaches the RX directly as well as after suffering a reflection from the IRS. Assuming negligible synchronization errors [55], for the n^{th} ambient symbol that is backscattered, the overall signal received at the M antenna RX is,

$$\mathbf{y}_n = \mathbf{f}_{\text{A}} s_n + \mathbf{f}_{\text{B}} b s_n + \mathbf{z}_n, \tag{3.3}$$

where $\mathbf{y}_n$ is an $M \times 1$ vector, $\mathbf{z}_n \sim \mathcal{CN}(0, \sigma^2 \mathbf{I}_M)$ is the AWGN and σ^2 is the noise power. $\mathbf{f}_{\text{A}}$ is the total effective channel experienced by the direct signal from the AS, i.e.,

$$\mathbf{f}_{\text{A}}(\mathbf{\Theta}) = \sqrt{\beta_{\text{A-R}}} \mathbf{h}_{\text{A-R}} + \sqrt{\beta_{\text{A-I-R}}} \mathbf{H}_{\text{I-R}} \mathbf{\Theta} \mathbf{h}_{\text{A-I}}, \tag{3.4}$$

and $\mathbf{f}_{\text{B}}$ is total effective channel (from the AS to BD to RX including the intermediate IRS reflections) experienced by the backscattered signal, i.e.,

$$\begin{aligned} \mathbf{f}_{\text{B}}(\mathbf{\Theta}) = &\left(\sqrt{\beta_{\text{A-B}}} h_{\text{A-B}} + \sqrt{\beta_{\text{A-I-B}}} \mathbf{h}_{\text{B-I}}^H \mathbf{\Theta} \mathbf{h}_{\text{A-I}}\right) \\ &\times \left(\sqrt{\beta_{\text{B-R}}} \mathbf{h}_{\text{B-R}} + \sqrt{\beta_{\text{B-I-R}}} \mathbf{H}_{\text{I-R}} \mathbf{\Theta} \mathbf{h}_{\text{B-I}}\right). \end{aligned} \tag{3.5}$$

Note that there are N elements of IRS and M antennas at the reader. The channels from the ambient source, backscatter device and the reader to the IRS are $\mathbf{h}_{A-I} \in \mathbb{C}^{N \times 1}$, $\mathbf{h}_{B-I} \in \mathbb{C}^{N \times 1}$ and $\mathbf{H}_{R-I} \in \mathbb{C}^{N \times M}$ respectively. Similarly, the channels from the ambient source to the backscatter device and the reader are represented by $h_{A-B} \in \mathbb{C}^{1 \times 1}$ and

$\mathbf{h}_{A-R} \in \mathbb{C}^{M\times 1}$ respectively, while the channel from the BD to the RX is represented by $\mathbf{h}_{B-R} \in \mathbb{C}^{M\times 1}$. h_{A-B} is a scalar as there is a single channel coefficient between the ambient source and the backscatter device, whereas the other channels are multi-dimensional and hence expressed as vectors/matrices.

Substituting (3.4) and (3.5) in (3.3) we get,

$$\begin{aligned}\mathbf{y}_n = \Bigg\{ &\sqrt{\beta_{\text{A-R}}}\mathbf{h}_{\text{A-R}} + \sqrt{\beta_{\text{A-I-R}}}\mathbf{H}_{\text{I-R}}\boldsymbol{\Theta}\mathbf{h}_{\text{A-I}} + \Bigg(\sqrt{\beta_{\text{A-B}}\beta_{\text{B-R}}}h_{\text{A-B}}\mathbf{h}_{\text{B-R}} \\ &+ \sqrt{\beta_{\text{A-B}}\beta_{\text{B-I-R}}}h_{\text{A-B}}\mathbf{H}_{\text{I-R}}\boldsymbol{\Theta}\mathbf{h}_{\text{B-I}} + \sqrt{\beta_{\text{A-I-B}}\beta_{\text{B-R}}}\mathbf{h}_{\text{B-R}}\mathbf{h_{B-I}}^{H}\boldsymbol{\Theta}\mathbf{h}_{\text{A-I}} \\ &+ \sqrt{\beta_{\text{A-I-B}}\beta_{\text{B-I-R}}}\mathbf{H}_{\text{I-R}}\boldsymbol{\Theta}\mathbf{h}_{\text{B-I}}\mathbf{h}_{\text{B-I}}^{H}\boldsymbol{\Theta}\mathbf{h}_{\text{A-I}}\Bigg)b\Bigg\}s_n + \mathbf{z}_n. \end{aligned} \tag{3.6}$$

The receiver performs receive beamforming on the received signal $\mathbf{y}_n$ to obtain

$$v_n = \mathbf{w}^H\mathbf{y}_n = \mathbf{w}^H(\mathbf{f}_{\text{A}}(\boldsymbol{\Theta}) + \mathbf{f}_{\text{B}}(\boldsymbol{\Theta})b)s_n + \mathbf{w}^H\mathbf{z}_n, \tag{3.7}$$

where $\mathbf{w}$ represents the receive beamforming vector. v_n then follows CSCG distribution such that,

$$v_n \sim \begin{cases} \mathcal{CN}(0, C_0), & \text{if } b = 0 \\ \mathcal{CN}(0, C_1), & \text{if } b = 1, \end{cases} \tag{3.8}$$

where

$$C_0 = \mathbf{w}^H\mathbf{R}_0\mathbf{w} \tag{3.9}$$

$$C_1 = \mathbf{w}^H\mathbf{R}_1\mathbf{w} \tag{3.10}$$

are the energies received at the RX when bits 0 and 1 are transmitted respectively by the BD. Note that $\mathbf{R_0}$ and $\mathbf{R_1}$ are given by:

$$\mathbf{R}_0 = P_s \ \mathbf{f}_{\text{A}}(\boldsymbol{\Theta})\mathbf{f}_{\text{A}}(\boldsymbol{\Theta})^H + \sigma^2\mathbf{I}_M \tag{3.11}$$

$$\mathbf{R}_1 = P_s \ \Big(\mathbf{f}_{\text{A}}(\boldsymbol{\Theta}) + \mathbf{f}_{\text{B}}(\boldsymbol{\Theta})\Big)\Big(\mathbf{f}_{\text{A}}(\boldsymbol{\Theta}) + \mathbf{f}_{\text{B}}(\boldsymbol{\Theta})\Big)^H + \sigma^2\mathbf{I}_M. \tag{3.12}$$

The output v_n of the receive beamformer then goes to the energy detector that compares it against a decision threshold T to detect whether b sent by the BD was a 0 or 1:

$$V = \frac{\epsilon}{S} \sum_{n=1}^{S} \left| \mathbf{w}^H v_n \right|^2 \gtrless_{b=0}^{b=1} T, \tag{3.13}$$

where $\epsilon = sgn(C_1 - C_0)$ and $T = \frac{\epsilon C_1 C_0}{C_1 - C_0} \ln \frac{C_1}{C_0}$ [62]. To evaluate the BER of the system, we define the *generalized relative channel difference (GRCD)* [62, 90] as the energy ratio between the symbol with the higher energy and the symbol with the lower energy, i.e.,

$$\Delta_C \triangleq \max \left\{ \frac{C_1}{C_0}, \frac{C_0}{C_1} \right\} = \max \left\{ \frac{\mathbf{w}^H \mathbf{R}_1 \mathbf{w}}{\mathbf{w}^H \mathbf{R}_0 \mathbf{w}}, \frac{\mathbf{w}^H \mathbf{R}_0 \mathbf{w}}{\mathbf{w}^H \mathbf{R}_1 \mathbf{w}} \right\} \tag{3.14}$$

For a reasonably large S, using the central limit theorem, the BER is given by [62], [90] as[2]

$$P_e = \frac{1}{2} \left[\mathcal{Q}\left(\sqrt{S} \left(\frac{\Delta_C \log \Delta_C}{\Delta_C - 1} - 1 \right) \right) + \mathcal{Q}\left(\sqrt{S} \left(1 - \frac{\log \Delta_C}{\Delta_C - 1} \right) \right) \right] \tag{3.15}$$

Since $\Delta_c \geq 1$, $\left(\frac{\Delta_C \log \Delta_C}{\Delta_C - 1} - 1 \right)$ and $\left(1 - \frac{\log \Delta_C}{\Delta_C - 1} \right)$ are both monotonically increasing functions of Δ_c in this range. Therefore, due to the monotonicity of the Q-function, the GRCD directly measures the BER.

3.3 Proposed Beamforming Scheme

3.3.1 Problem Formulation

We study the BER minimization problem in an IRS-aided ambient BackCom system. To minimize the BER we use the GRCD defined in (3.14). The GRCD measures the ratio of the magnitudes of the energies of the two symbols received at the RX and directly determines the BER of the energy detector based ambient BackCom system [62, 90]. To minimize the BER, we find the phase shift matrix $\mathbf{\Theta}$ and the receive beamforming vector $\mathbf{w}$ to maximize the GRCD

$$(\text{P1}): \quad \max_{\mathbf{\Theta}, \mathbf{w}} \quad \Delta_C \tag{3.16a}$$

$$\text{s.t.} \quad \theta_n \in [0, 2\pi] \ \forall n \in \{1, 2, ..., N\} \tag{3.16b}$$

[2]The BER expression given here is for the case $C_1 \geq C_0$. The case of $C_0 > C_1$ is analogous.

(P1) is not a convex optimization problem as the objective function is non-convex with respect to $\mathbf{w}$ and $\boldsymbol{\Theta}$, although the constraints are convex. In general, there is no standard method for solving such non-convex problems optimally [92].

3.3.2 Proposed Scheme

Instead of searching for the optimal values of $\boldsymbol{\Theta}$ and $\mathbf{w}$ in the entire solution space defined by constraint (3.16b), we note that the ambient BackCom system has a unique characteristic of detecting a weak backscatter signal from the BD in the presence of very strong DLI. Leveraging this unique inherent characteristic of such systems, significant BER improvement can be brought about by strengthening the backscatter signal and by increasing the contrast in the received energies corresponding to bit '0' and bit '1' being sent by the BD. So instead of solving (P1), which takes into account the joint optimization of $\boldsymbol{\Theta}$ and $\mathbf{w}$ to maximize GRCD, we propose a two-step sub-optimal strategy and show that its performance is comparable to the optimal solution of (P1) obtained by exhaustive search.

We propose to use an IRS for the specific purpose of enhancing the quality of the backscatter signal arriving at the RX by balancing the signal strengths of the direct and reflected paths. In particular, we first find the IRS phase shifts that maximize the backscatter signal strength arriving at the RX. Afterwards, we employ optimal beamforming at the RX, which maximizes the GRCD, that depends on the ratio of received energies corresponding to bits '0' and '1'. Finally, we perform energy detection on the backscatter signal. It is noteworthy that owing to the non-convexity of the problems and the number of variables involved, alternating optimization is generally the go-to technique for problems involving optimization over multiple variables in IRS-based systems. In contrast, our proposed scheme consists of just two steps performed sequentially and is therefore computationally less intensive.

Our proposed scheme can be broken down into the following two steps:

- In the first step, as the BD sends a known signal, we find the phase shifts at the IRS to maximize the strength of the backscatter signal arriving at the RX. To this end we can write the following optimization problem:

$$\text{(P2)}: \quad \max_{\boldsymbol{\Theta}} \quad ||\mathbf{f}_{\mathrm{B}}(\boldsymbol{\Theta})||^2 \tag{3.17a}$$

$$\text{s.t.} \quad |e^{j\theta_n}| = 1, \forall n \in \{1, 2, ..., N\} \tag{3.17b}$$

- In the second step, the IRS sets its phase shifts according to $\boldsymbol{\Theta}^*$ obtained in step

1, to strengthen the backscatter signal. The RX performs optimal beamforming based on SINR maximization principle. As mentioned before, for an energy detector based RX, the optimal receive beamforming vector is the one that maximizes the difference of the two energies corresponding to bits '0' and '1'. The difference of the two energies is measured by the GRCD defined in (3.14). Mathematically, we have the following optimization problem,

$$(\text{P3}): \quad \max_{\mathbf{w}} \quad \Delta_C \tag{3.18}$$

Since the IRS fixes its phase shifts according to $\boldsymbol{\Theta}^*$ in this step, (P3) is just an optimization over candidate beamforming vectors $\mathbf{w}$.

3.4 Problem Solution

3.4.1 Solution to (P2)

In this subsection, we solve (P2). To obtain a solution for $\boldsymbol{\Theta}$, we simplify the objective function in (3.16a) by splitting it into the product of a scalar term and a squared norm:

$$\|\mathbf{f}_{\text{B}}(\Theta)\|^2 = |\mathbf{f}_{\text{B1}}(\boldsymbol{\Theta})|^2 \, \|\mathbf{f}_{\text{B2}}(\Theta)\|^2 . \tag{3.19}$$

$|\mathbf{f}_{\text{B1}}(\Theta)|^2$ is given by,

$$\begin{aligned} |\mathbf{f}_{\text{B1}}(\Theta)|^2 &= \left| \sqrt{\beta_{\text{A-B}}} h_{\text{A-B}} + \sqrt{\beta_{\text{A-I-B}}} \mathbf{h}_{\text{B-I}}^H \boldsymbol{\Theta} \mathbf{h}_{\text{A-I}} \right|^2 \\ &= \beta_{\text{A-I-B}} \mathbf{v}^H \boldsymbol{\Phi}_{\text{A-I-B}} \boldsymbol{\Phi}_{\text{A-I-B}}^H \mathbf{v} + \sqrt{\beta_{\text{A-B}} \beta_{\text{A-I-B}}} \mathbf{v}^H \boldsymbol{\Phi}_{\text{A-I-B}} h_{\text{A-B}}^H \\ &\quad + \sqrt{\beta_{\text{A-B}} \beta_{\text{A-I-B}}} h_{\text{A-B}} \boldsymbol{\Phi}_{\text{A-I-B}}^H \mathbf{v} + \beta_{\text{A-B}} |h_{\text{A-B}}|^2, \end{aligned} \tag{3.20}$$

where $\boldsymbol{\Phi}_{\text{A-I-B}} \triangleq \text{diag}(\mathbf{h}_{\text{A-I}}^H) \mathbf{h}_{\text{B-I}}$ and $\mathbf{v} = \left[e^{j\theta_1}, \ldots, e^{j\theta_N} \right]^H$ such that $|v_n| = 1, \ \forall n \in \{1, \ldots, N\}$.

Let

$$\mathbf{S_1} = \begin{bmatrix} \beta_{\text{A-I-B}} \boldsymbol{\Phi}_{\text{A-I-B}} \boldsymbol{\Phi}_{\text{A-I-B}}^H & \sqrt{\beta_{\text{A-B}} \beta_{\text{A-I-B}}} \boldsymbol{\Phi}_{\text{A-I-B}} h_{\text{A-B}} \\ \sqrt{\beta_{\text{A-B}} \beta_{\text{A-I-B}}} h_{\text{A-B}}^* \boldsymbol{\Phi}_{\text{A-I-B}}^H & 0 \end{bmatrix}, \overline{\mathbf{v}} = \begin{bmatrix} \mathbf{v} \\ 1 \end{bmatrix}. \tag{3.21}$$

Then (3.20) can be re-written in matrix form as

$$|\mathbf{f}_{\text{B1}}(\Theta)|^2 = \overline{\mathbf{v}}^H \mathbf{S}_1 \overline{\mathbf{v}} + \beta_{\text{A-B}} |h_{\text{A-B}}|^2. \tag{3.22}$$

Similarly, $\|\mathbf{f}_{\text{B2}}(\Theta)\|^2$ is given by,

$$\begin{aligned}\|\mathbf{f}_{\text{B2}}(\Theta)\|^2 &= \left\|\sqrt{\beta_{\text{B-R}}}\mathbf{h}_{\text{B-R}} + \sqrt{\beta_{\text{B-I-R}}}\mathbf{H}_{\text{I-R}}\boldsymbol{\Theta}\mathbf{h}_{\text{B-I}}\right\|^2 \\ &= \beta_{\text{B-I-R}}\mathbf{v}^H\boldsymbol{\Phi}_{\text{B-I-R}}\boldsymbol{\Phi}_{\text{B-I-R}}^H\mathbf{v} + \sqrt{\beta_{\text{B-R}}\beta_{\text{B-I-R}}}\mathbf{v}^H\boldsymbol{\Phi}_{\text{B-I-R}}\mathbf{h}_{\text{B-R}} \\ &\quad + \sqrt{\beta_{\text{B-R}}\beta_{\text{B-I-R}}}\mathbf{h}_{\text{B-R}}^H\boldsymbol{\Phi}_{\text{B-I-R}}^H\mathbf{v} + \beta_{\text{B-R}}|\mathbf{h}_{\text{B-R}}|^2, \quad (3.23)\end{aligned}$$

with $\boldsymbol{\Phi}_{\text{B-I-R}} \triangleq \text{diag}(\mathbf{h}_{\text{B-I}}^H)\mathbf{H}_{\text{I-R}}^H$ and $\mathbf{v}$ as defined above.
Again, let

$$\mathbf{S_2} = \begin{bmatrix} \beta_{\text{B-I-R}}\boldsymbol{\Phi}_{\text{B-I-R}}\boldsymbol{\Phi}_{\text{B-I-R}}^H & \sqrt{\beta_{\text{B-R}}\beta_{\text{B-I-R}}}\boldsymbol{\Phi}_{\text{B-I-R}}h_{\text{B-R}} \\ \sqrt{\beta_{\text{B-R}}\beta_{\text{B-I-R}}}\mathbf{h}_{\text{B-R}}^H\boldsymbol{\Phi}_{\text{B-I-R}}^H & 0 \end{bmatrix}.\overline{\mathbf{v}} = \begin{bmatrix}\mathbf{v}\\ 1\end{bmatrix}. \quad (3.24)$$

Then (3.23) can also be re-written in matrix form as follows:

$$|\mathbf{f}_{\text{B2}}(\boldsymbol{\Theta})|^2 = \overline{\mathbf{v}}^H\mathbf{S}_2\overline{\mathbf{v}} + \beta_{\text{B-R}}|\mathbf{h}_{\text{B-R}}|^2, \quad (3.25)$$

Substituting (3.22) and (3.25) in (3.19). we get,

$$G_o(\overline{\mathbf{v}}) = \overline{\mathbf{v}}^H\mathbf{S}_2\overline{\mathbf{v}}\overline{\mathbf{v}}^H\mathbf{S}_1\overline{\mathbf{v}} + k_1\overline{\mathbf{v}}^H\mathbf{S}_2\overline{\mathbf{v}} + k_2\overline{\mathbf{v}}^H\mathbf{S}_1\overline{\mathbf{v}} + k_1k_2, \quad (3.26)$$

with $k_1 = |h_{A-B}|^2$ and $k_2 = \|\mathbf{h}_{B-R}\|^2$.

Using (3.26), (P2) can be written as

$$\begin{aligned}(\text{P4}): \quad &\max_{\overline{\mathbf{v}}} \quad G_o(\overline{\mathbf{v}}) && (3.27a)\\ &\text{s.t.} \quad |\overline{\mathbf{v}}_n| = 1, \forall n \in \{1, 2, ..., N\} && (3.27b)\end{aligned}$$

In the equivalent problem (P4), the objective function (3.27a) is a quartic polynomial in $\overline{\mathbf{v}}$. We let $\mathbf{V} = \overline{\mathbf{v}}\overline{\mathbf{v}}^H$ so that the objective function can be expressed as a function of $\mathbf{V}$ in terms of trace (i.e., $\text{tr}(\mathbf{SV})$), which is rank-one. However, since $\mathbf{S}_1$ and $\mathbf{S}_2$ are not positive semi-definite in general, one of the resulting trace terms in (3.27a), i.e., $\text{tr}(\mathbf{S}_2\mathbf{V}\mathbf{S}_1\mathbf{V})$, turns out to be generally non-convex. Moreover, optimizing multivariate polynomials of higher degrees is an NP-hard problem [121]. Therefore, a closed-form, optimal solution is generally not available. To solve this issue, we employ the MM algorithm [82]. The MM algorithm attempts to solve this difficult problem by constructing a series of more tractable approximate sub-problems, using a convex approximation to the original objective function.

The MM algorithm leverages a surrogate function that serves as a minorizer to an

objective function $f(\mathbf{x}) : \mathbb{C}^N \rightarrow \mathbb{R}$ with bounded curvature by taking the second-order Taylor expansion [122, Lemma 12]:

$$f(\mathbf{x}) \geq f(\mathbf{x}_0) + \mathrm{Re}\left\{\nabla f(\mathbf{x}_0)^H(\mathbf{x}-\mathbf{x}_0)\right\} - \frac{\ell}{2}\left\|\mathbf{x}-\mathbf{x}_0\right\|^2, \tag{3.28}$$

where $\mathbf{x}_0 \in \mathbb{C}^N$ is the point where the original and the surrogate functions intersect, ∇ is the gradient operator and ℓ is the maximum curvature of $f(\mathbf{x})$. According to (3.28), we find the minorizer $G_{m_1}(\overline{\mathbf{v}})$ to the objective function $G_o(\overline{\mathbf{v}})$ i.e.,

$$G_o(\overline{\mathbf{v}}) \geq G_m(\overline{\mathbf{v}}), \tag{3.29}$$

such that

$$\begin{aligned} G_{m_1}(\overline{\mathbf{v}}) = G_o(\overline{\mathbf{v}_0}) + \overline{\mathbf{v}}_0^H\mathbf{U}(\overline{\mathbf{v}}-\overline{\mathbf{v}}_0) + (\overline{\mathbf{v}}-\overline{\mathbf{v}}_0)^H\mathbf{U}\overline{\mathbf{v}}_0 \\ - \frac{\ell}{2}\left\|\overline{\mathbf{v}}-\overline{\mathbf{v}}_0\right\|^2, \end{aligned} \tag{3.30}$$

with $\mathbf{U} = \mathbf{S}_1\overline{\mathbf{v}}_0\overline{\mathbf{v}}_0^H\mathbf{S}_2 + \mathbf{S}_2\overline{\mathbf{v}}_0\overline{\mathbf{v}}_0^H\mathbf{S}_1 + k_2\mathbf{S}_1 + k_1\mathbf{S}_2$ being a Hermitian matrix obtained from the derivative of $G_o(\overline{\mathbf{v}}_0)$. Expanding (3.30) we get,

$$\begin{aligned} G_{m_1}(\overline{\mathbf{v}}) = -\frac{\ell}{2}\Bigg(\overline{\mathbf{v}}^H\mathbf{I}\overline{\mathbf{v}} + \overline{\mathbf{v}}^H\left(-\frac{2}{\ell}\mathbf{U}\overline{\mathbf{v}}_0 - \mathbf{I}\overline{\mathbf{v}}_0\right) \\ + \left(-\frac{2}{\ell}\mathbf{U}\overline{\mathbf{v}}_0 - \mathbf{I}\overline{\mathbf{v}}_0\right)^H\overline{\mathbf{v}}\Bigg) + k, \end{aligned} \tag{3.31}$$

where k denotes the cumulative sum of all constant terms. (3.31) is of quadratic form, and can be rewritten as:

$$G_{m_1}(\overline{\overline{\mathbf{v}}}) = \overline{\overline{\mathbf{v}}}^H\mathbf{Q}\overline{\overline{\mathbf{v}}} + k \tag{3.32}$$

where

$$\mathbf{Q} = -\begin{bmatrix} \mathbf{I} & -\frac{2}{\ell}\mathbf{U}\overline{\mathbf{v}}_0 - \mathbf{I}\overline{\mathbf{v}}_0 \\ (-\frac{2}{\ell}\mathbf{U}\overline{\mathbf{v}}_0 - \mathbf{I}\overline{\mathbf{v}}_0)^H & 0 \end{bmatrix}, \ \overline{\overline{\mathbf{v}}} = \begin{bmatrix} \overline{\mathbf{v}} \\ 1 \end{bmatrix}. \tag{3.33}$$

Letting $\overline{\overline{\mathbf{V}}} = \overline{\overline{\mathbf{v}}}\overline{\overline{\mathbf{v}}}^H$, a transformed version of Problem (P4) is given by

$$(\mathrm{P5}): \quad \max_{\overline{\overline{\mathbf{V}}}} \quad \mathrm{tr}(\mathbf{Q}\overline{\overline{\mathbf{V}}}) + k, \tag{3.34a}$$

$$\text{s.t.} \quad \overline{\overline{\mathbf{V}}}_{n,n} = 1, \ \forall n \in \{1,\ldots,N+2\}, \tag{3.34b}$$

$$\overline{\overline{\mathbf{V}}} \succeq 0, \tag{3.34c}$$

$$\text{rank}(\overline{\overline{\mathbf{V}}}) = 1. \tag{3.34d}$$

One potential strategy to tackle this situation is to drop the rank-one constraint, such that Problem (P5) becomes a convex semidefinite program (SDP), which is solvable using CVX [123]. The solution obtained by CVX may or may not be rank one. Therefore, Gaussian randomization [124] can be used, yielding a candidate vector, whose last element is dropped and then the resulting $N \times 1$ vector is substituted in (3.31) during the next MM iteration to obtain a new approximation to $G_o(\overline{\mathbf{v}})$. This process needs to be repeated till the MM algorithm converges.

The above stated process incurs a formidable complexity of the order of $O(I(N+2)^{4.5})$, where I is the number MM iterations, and the $(N+2)^{4.5}$ is the SDP complexity [125]. An alternative, less costly approach is to further take a minorizer G_{m_2} to G_{m_1}, similar to the procedure in [126] such that,

$$G_o(\overline{\mathbf{v}}) \geq G_{m_1}(\overline{\overline{\mathbf{v}}}) \geq G_{m_2}(\overline{\overline{\mathbf{v}}}). \tag{3.35}$$

where

$$G_{m_2}(\overline{\overline{\mathbf{v}}}) = \overline{\overline{\mathbf{v}}}^H \mathbf{T} \overline{\overline{\mathbf{v}}} + 2\text{Re}\{\overline{\overline{\mathbf{v}}}^H (\mathbf{Q} - \mathbf{T}) \overline{\overline{\mathbf{v}}}_0\} + \overline{\overline{\mathbf{v}}}_0{}^H (\mathbf{Q} - \mathbf{T}) \overline{\overline{\mathbf{v}}}_0 \tag{3.36}$$

Note that $\mathbf{T} = \lambda^- \mathbf{I}$, where λ^- is the minimum eigenvalue of $\mathbf{Q}$ and $\overline{\overline{\mathbf{v}}}_0$ is as before. G_{m_2} can serve as the objective function in each MM iteration instead of G_{m_1}. Ignoring the constant terms, the sub-problem to be solved in each iteration of the MM algorithm reduces to:

$$\begin{aligned}
(\text{P6}): \quad \max_{\overline{\overline{\mathbf{v}}}} \quad & 2\text{Re}\{\overline{\overline{\mathbf{v}}}^H (\mathbf{Q} - \mathbf{T}) \overline{\overline{\mathbf{v}}}_0\}, && \text{(3.37a)} \\
\text{s.t.} \quad & |\overline{\overline{\mathbf{v}}}_{n,n}| = 1, \ \forall n \in \{1, \ldots, N+2\}, && \text{(3.37b)} \\
& \overline{\overline{\mathbf{v}}}_{j,j} = 1, j = \{N+1, N+2\}, && \text{(3.37c)}
\end{aligned}$$

The closed form solution to (P6) is given by $\overline{\overline{\mathbf{v}}}^* = e^{j \ \arg((\mathbf{Q}-\mathbf{T})\overline{\overline{\mathbf{v}}}_0)}$.

It is noteworthy that the objective function G_o in the original problem (P4) is bounded from above, as $\mathbf{S}_1$ and $\mathbf{S}_2$ are constant matrices and $\|\overline{\mathbf{v}}\|^2 = N$ is a finite constant. Moreover, G_{m_1} and G_{m_2} can each serve as a minorizer to G_o and can also can be shown to satisfy the conditions for the convergence of MM algorithm, as stated in [122,126]. We run the MM algorithm with G_{m_2} as the surrogate function, such that a closed form optimal solution in terms of $\overline{\overline{\mathbf{v}}}$ is returned in each iteration. Therefore, the solution obtained

Algorithm 1 MM Algorithm for solving (P4)

1: **Initialize:** Random IRS phase shifts θ; set iteration number $i = 1$.
2: Obtain $\overline{\mathbf{v}}$ from θ and set $\overline{\mathbf{v}}_0^{(i)} = \overline{\mathbf{v}}$.
3: **while** the rate of change in objective function (3.26) is above a threshold $\varepsilon > 0$ **do**
4: Construct $\mathbf{Q}$ from $\overline{\mathbf{v}}_0^{(i)}$ and $\mathbf{U}$. 5: Set $\overline{\mathbf{v}}^{(i+1)} \leftarrow \overline{\overline{\mathbf{v}}}^{*} = e^{j \arg((\mathbf{Q}-\mathbf{T})\overline{\overline{\mathbf{v}}}_0)}$ for next iteration.
6: Update iteration number $i \leftarrow i + 1$.
7: **end while**
8: **Return:** Optimized phase shift vector $\mathbf{v}^*$ by dropping the last element of $\overline{\mathbf{v}}_0$ at convergence.

in each subsequent iteration of the MM algorithm will result in a monotonic increase in G_o and will ultimately converge to a local optimum. This approach, summarized in **Algorithm 1**, will incur a complexity of the order of $O(IN)$.

3.4.2 Solution to (P3)

Similarly to [62], (P3) is solved as follows: Substituting the definition of GRCD from (3.14) into (3.18) we get:

$$\text{(P3):} \quad \max_{\mathbf{w}} \left(\max \left(\frac{\mathbf{w}^{\mathrm{H}} \mathbf{R}_0 \mathbf{w}}{\mathbf{w}^{\mathrm{H}} \mathbf{R}_1 \mathbf{w}}, \frac{\mathbf{w}^{\mathrm{H}} \mathbf{R}_1 \mathbf{w}}{\mathbf{w}^{\mathrm{H}} \mathbf{R}_0 \mathbf{w}} \right) \right). \tag{3.38}$$

To solve (P3), without loss of generality we consider $f(\mathbf{w}) = \frac{\mathbf{w}^{\mathrm{H}} \mathbf{R}_1 \mathbf{w}}{\mathbf{w}^{\mathrm{H}} \mathbf{R}_0 \mathbf{w}}$. Then to find the maximum of (P3), we differentiate $f(\mathbf{w})$ with respect to $\mathbf{w}$ and set it equal to zero, i.e.,

$$\frac{d}{d\mathbf{w}} f(\mathbf{w}) = \frac{2\mathbf{R}_1 \mathbf{w} \left(\mathbf{w}^{\mathrm{H}} \mathbf{R}_0 \mathbf{w} \right) - 2\mathbf{R}_0 \mathbf{w} \left(\mathbf{w}^{\mathrm{H}} \mathbf{R}_1 \mathbf{w} \right)}{\left(\mathbf{w}^{\mathrm{H}} \mathbf{R}_0 \mathbf{w} \right)^2} = 0. \tag{3.39}$$

Rearringing (3.39) we obtain $\mathbf{R}_1 \mathbf{w} = f(\mathbf{w}) \mathbf{R}_0 \mathbf{w}$, which can be recognized as a generalized eigenvalue problem with $\lambda = f(\mathbf{w})$ being the eigenvalue and $\mathbf{w}$ the corresponding eigenvector. Let $\lambda_{\max}$ and $\lambda_{\min}$ be the maximum and minimum generalized eigenvalues, and $\mathbf{w}_{\max}$ and $\mathbf{w}_{\min}$ be the corresponding eigenvectors, respectively. Then, the optimal beamforming vector is by $\mathbf{w}_{\max}$ if $\lambda_{\max} \geq \frac{1}{\lambda_{\min}}$ and it is $\mathbf{w}_{\min}$ otherwise.

3.5 Results

In this section, we provide simulation results to evaluate our proposed scheme. We consider an ambient backscatter scenario, with an ambient signal of frequency 915 MHz. The AS, BD, IRS and RX are located at $[-50, 2, 5]$, $[10, 2, 0]$, $[0, 0, 2]$ and $[15, 2, 0]$ respectively, with all the coordinates in meters. The values of rest of system parameters are: $\alpha = 2.5$, $G_s = 1.5$ dB, $G_r = 1.5$ dB, $P_s = 30$ dBm, $\sigma^2 = -80$ dBm. The Nakagami-m parameter is set to 5 for all the links among IRS, BD and RX, while it is set to 1 for the links from IRS, BD and RX to the AS [118–120]. We set the backscatter frame consisting of 100 backscatter symbols and average our results over 1.5×10^6 Monte-Carlo runs.

3.5.1 Benchmark Solutions

For the purpose of comparison with our proposed scheme for the IRS-aided system, the alternating optimization based successive refinement of IRS phase shifts presented in [92] can be adapted as a benchmark. However, this adaptation is not straightforward as it does not yield a meaningful bound, unless some form of strengthening the backscatter signal or DLI cancellation is included. So we resort to exhaustive search to solve (P1) and establish a benchmark for IRS-aided ambient BackCom system. In addition we also present the following benchmarks for comparison:

- IRS-less system with zero-forcing beamforming (ZFBF) at the RX.
- IRS-less system with eigenvector beamforming (EBF) at the RX.
- IRS-aided system with ZFBF at the RX and IRS phase shifts set to random values.
- IRS-aided system with EBF at the RX and IRS phase shifts set to random values.
- IRS-aided system with ZFBF at the RX and IRS phase shifts calculated by solving (P2) given in (3.17a).

3.5.2 BER Performance with respect to the IRS size

Fig. 3.2 illustrates the BER performance of the proposed scheme with respect to the number of elements N of the IRS for $P_s = 30$ dBm and $S = 60$. The plot for exhaustive search results has only three data points highlighted by Δ for $N \in \{4, 6, 8\}$. Further data points could not be obtained because the exhaustive search method demands excessive computational resources. The plots of other five benchmarks enumerated above have

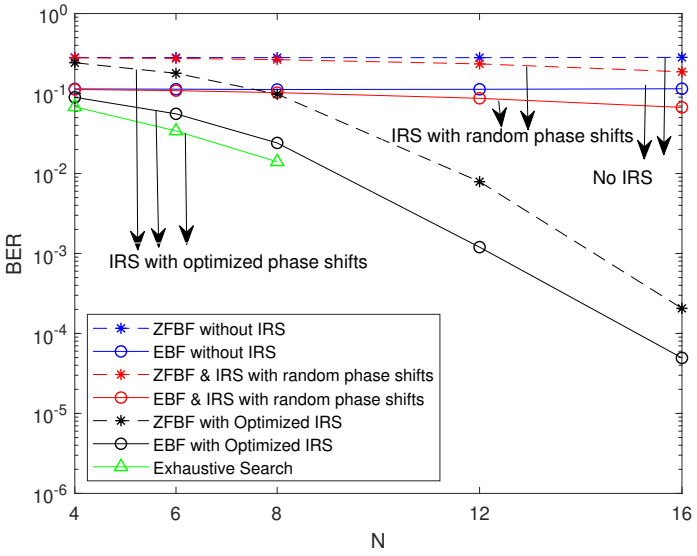

Figure 3.2: BER versus N with $P_s = 30$ dBm, $S = 60$, $M = 4$ with IRS located at $(12, 2, 5)$.

also been included. The main motivation for providing exhaustive search results was to establish the viability of the proposed scheme, i.e., despite being suboptimal, it provides results close to those obtained by exhaustive search. Fewer data points were plotted for in this benchmark because the exhaustive search method demands excessive computational resources and it is difficult to implement for larger values of N.

We can see that the gap between the plots for our proposed scheme and for the exhaustive search reduces as N increases. This highlights the usefulness of our scheme, as it is computationally less intensive and performs fairly closely (as N increases) to the results obtained by solving (P1) by exhaustive search.

Comparing the results of the proposed scheme with the benchmarks we can see that the performance of the system without the IRS is worst, regardless of the beamforming used at the RX. For the systems including an IRS with random phase shifts, we see a marginal improvement over the baseline schemes. However, with an optimized IRS, there is a marked improvement in the performance of both eigenvector and zero-forcing beamforming based energy detection. In all scenarios, EBF at the RX performs better than its zero-forcing counterpart, because the ZFBF removes the direct-link interference altogether and reduces overall signal strength at the RX, leading to performance loss. On the other hand, EBF at the RX achieves the perfect balance by maximizing the contrast between the two received energies and when employed with an optimized IRS

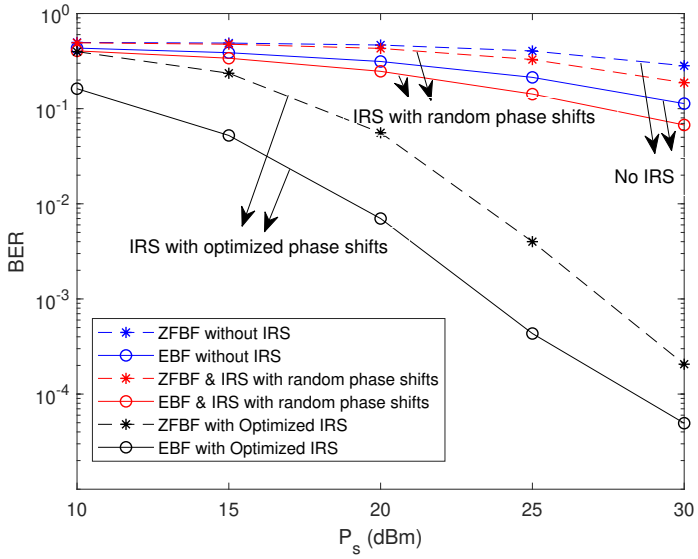

Figure 3.3: BER versus P_s with $S = 60$, $N = 16$, $M = 4$ with IRS located at $(12, 2, 5)$.

for maximizing backscatter signal strength, best performance is achieved.[3]

It is also clear from Fig. 3.2 that the BER significantly decreases with the increase of the IRS size. Even with an IRS of modest size $N = 4$, the BER is 8.9×10^{-2}. For an IRS of size $N = 16$ the BER drops to as low as 4.94×10^{-5}. We can see that with increase in its size, the IRS is more effective in balancing the signal strengths to increase the strength of received backscatter signal at the RX and thus reducing the BER further. Thus, an IRS of reasonable size can effectively boost the backscatter signal and thereby assist the RX in reducing the BER of energy detection.

3.5.3 BER Performance with respect to transmit power of the ambient source

Fig. 3.3 illustrates the BER performance with varying P_s, i.e., transmit power of the AS, for $N = 16$ and $S = 60$. It is seen that the BER of our proposed detector significantly decreases with the increase of P_s. This is in contrast to conventional ambient BackCom using simple energy detection at the RX [127], wherein, the BER did not decrease much with the increase of ambient signal power, but levels off in the high SNR region. This is due to the fact that the backscatter signal is inherently very weak. So when P_s increases, the subsequent increase in the DLI is orders of magnitude stronger than in the

[3]The overall computational complexity of the EBF with optimized IRS is $O(IN) + O(M^3)$.

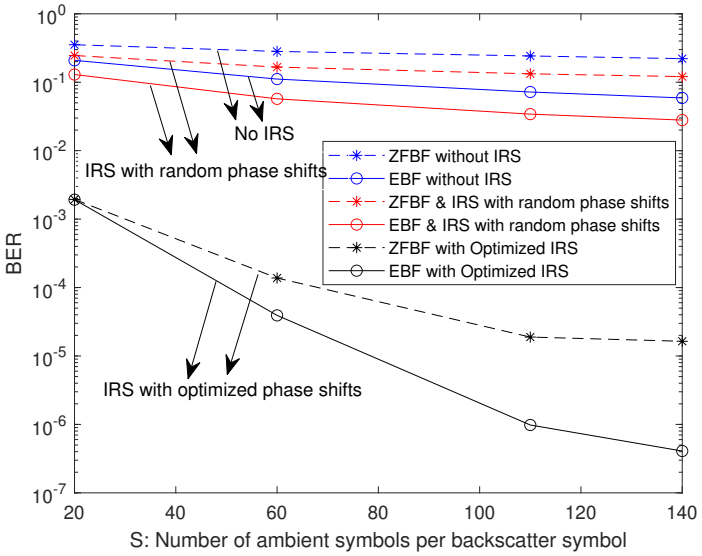

Figure 3.4: R versus S with $P_s = 30$ dBm, $N = 16$, $M = 4$ with IRS located at $(12, 2, 5)$.

backscatter signal. Consequently, the BER does not decrease much. To solve this issue, in benchmarks 1 and 2 originally proposed in [62], use ZFBF to remove DLI and EBF to maximize energy difference between the two backscatter symbols respectively, prior to energy detection at the RX. However, with practical system values, the backscatter signal is still very weak. Consequently, the relative energy difference between the signals corresponding to bit '1' and bit '0' received at the ED is very low, which leads to poor energy detection and the BER is still high. However, with the introduction of IRS, even with random phase shifts (benchmarks 3 and 4), the BER performance is somewhat improved. Finally, with an IRS optimized for maximizing backscatter signal strength, the BER performance drastically improves with increase in P_s as indicated by the steepness of the curve for our proposed scheme as well as for the ZFBF based solution.

3.5.4 BER Performance with respect to the number of ambient symbols per backscatter symbol

Fig. 3.4 illustrates the BER of our scheme for different values of S, i.e., the number of ambient symbols for which the backscatter symbol transmitted remains the same. For this plot, $P_s = 30$ dBm and $N = 16$. It is clear from the figure, that the performance in terms of BER of our proposed scheme as well as all benchmarks improves with an increase in S, at the cost of a lower transmission rate. Even with a low value of $S =$

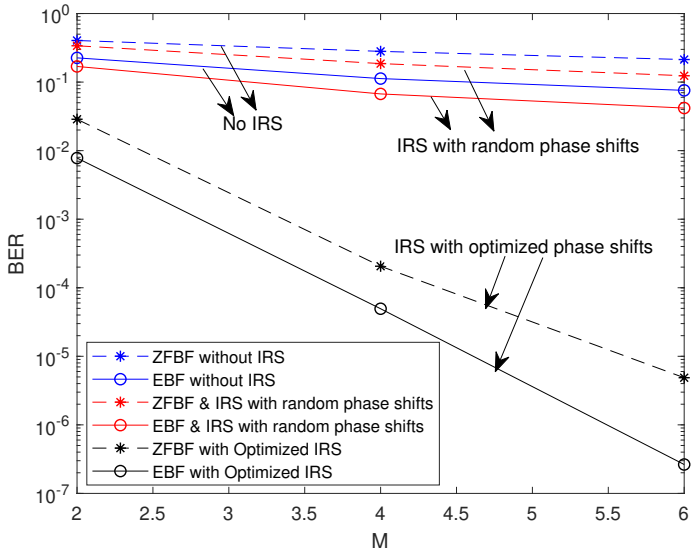

Figure 3.5: BER versus M with $P_s = 30$ dBm, $S = 60$, $N = 16$ with IRS located at $(12, 2, 5)$.

20 (corresponding to a higher transmission rate at the BD) the BER is 1.1×10^{-3}. It is also observed that as S increases, the slope of the BER curve somewhat tapers off. This is an encouraging outcome meaning that there is no significant advantage in extending the backscatter symbol lengths beyond a certain value as the IRS guarantees some performance improvement regardless of the backscatter transmission parameters.

3.5.5 BER Performance with respect to number of antennas at the ambient receiver

Fig. 3.5 illustrates the performance of our scheme for values of number of receive antennas M with $N = 16$, $P_s = 30$ dBm and $S = 60$. It can be seen that the performance improves for all bechmarks with the increase of M, due to the increased capability of beamforming at the RX. However, it is noteworthy, that for our proposed scheme, i.e., optimized IRS with EBF at the RX and the benchmark scheme with optimized IRS and ZFBF at the RX, the descent of the BER curves is significantly steeper than in the other benchmarks. This shows that with an optimized IRS assisting the backscatter signal, the EBF at the RX can more efficiently separate the powers corresponding to the two backscatter symbols, resulting in much improved BER.

3.5.6 BER Performance with respect to IRS placement

A plot of BER for three different placements of the IRS is shown in Fig. 3.6. We maintain the y and z coordinates of the IRS and move it parallel to the x-axis. Considering that we have kept the AS, BD and RX in a straight line in the $x-y$ plane, the three values of BER are obtained as we move the IRS from $(8, 2, 5)$ (between AS and BD) to $(12, 2, 5)$ (between BD and RX) to $(18, 2, 5)$ (on the other side of RX, away from AS and BD). We can see that as the IRS is moved to the other side of the RX i.e., to $(18, 2, 5)$, the BER goes up for all the schemes, as the increased distance of the IRS from the BD and the AS results in weakening the backscatter signal arriving at the RX. However, it is interesting to note that as the IRS moves from $(8, 2, 5)$ to $(12, 2, 5)$, the BER goes down for the ZFBF with optimized IRS benchmark, whereas it increases for our proposed scheme EBF with optimized IRS. This is due to the fact that the ZFBF at the RX completely eliminates the direct-link signal from the AS. Therefore, the IRS located at $(12, 2, 5)$ enjoys shorter distances to the BD and the RX and yields a smaller BER. On the other hand, our proposed scheme optimizes the received signal strength over the IRS reflection pattern and receive beamforming at the RX by maximizing the GRCD defined in (3.14). Therefore, when the IRS is at $(8, 2, 5)$, it is closer to the AS as well as the BD, while the distance from the RX is greater, but still reasonable. Therefore, the IRS is more effective is enhancing the signal strength and hence the GRCD, resulting in a lower BER at $(8, 2, 5)$. The BER increases as we move further away from the AS. Thus, we can conclude that for our proposed scheme, the IRS needs to be positioned such that it is as close to the AS as possible, while maintaining a short distance from the BD and the RX.

3.6 Summary

In this chapter, an IRS aided ambient BackCom system was studied and a new scheme was devised to enhance its performance in terms of BER. The non-convex problem of optimizing the phase shifts at the IRS for maximizing the backscatter signal strength arriving at the RX was addressed using SDR within MM algorithm. Our findings showed that with an IRS of moderate size enhancing the ambient BackCom system, the BER performance is significantly improved. The reduced BER can be instrumental in increasing the rate and range of ambient BackCom systems. The scheme proposed in this paper can be extended to multiple backscatter devices, where the role of IRS in aiding in collision avoidance can be studied as well. Moreover, future work can include the CSI estimation

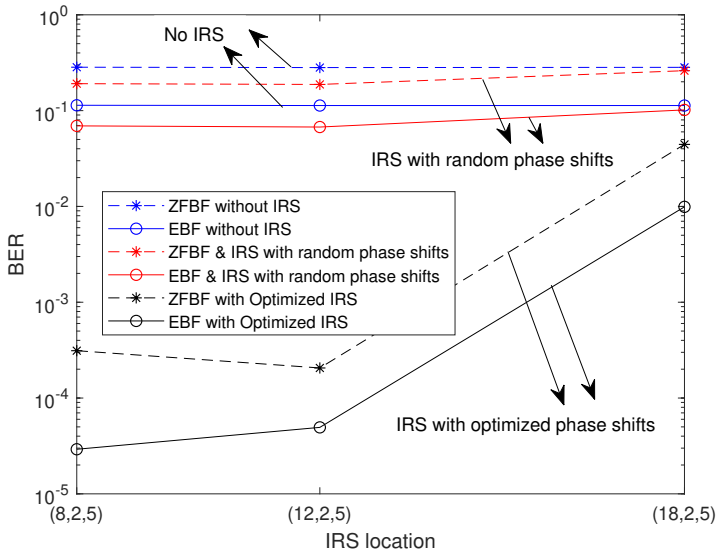

Figure 3.6: BER versus IRS position with $P_s = 30$ dBm, $S = 60$, $N = 16$ and $M = 4$.

problem of an IRS assisted ambient backscatter system.

Chapter 4

Joint Active and Passive Beamforming for IRS-assisted Monostatic Backscatter Systems: An Unsupervised Learning Approach

The Monostatic BackCom architecture, widely deployed in commercial applications, faces a range limitation that needs a cost-effective solution to unlock its potential for mass connectivity in future wireless networks. While legacy approaches such as tag modifications, relay-aided methods, and multi-antenna backscattering have been considered to extend BackCom's range, they come with drawbacks like high infrastructure costs, complexity, and increased power consumption, resulting in only incremental range improvements.

In the context of smart wireless environments shaping the future of wireless networks, leveraging an Intelligent Reflecting Surface (IRS) presents an energy-efficient and cost-effective solution to enhance the range and coverage of BackCom systems. Despite being a natural progression from traditional monostatic backscatter systems, the concept of addressing BackCom's limitations through a smart wireless propagation environment controlled by deep learning techniques remains relatively unexplored in existing literature.

Three innovative paradigms – BackCom for energy efficiency, IRS for low-cost smart propagation, and machine learning-driven intelligent control – have demonstrated their

utility and potential for next-generation self-sustainable wireless networks. When deployed together, they can facilitate massive energy-efficient connectivity for future IoT applications in an economically feasible manner.

Motivated by this perspective, our research focuses on an IRS-aided monostatic BackCom system featuring a multi-antenna reader. We propose a deep learning-based approach to jointly configure the IRS and the reader, thereby enhancing the BackCom system's performance. Our findings reveal that our monostatic BackCom system, even when assisted by a moderately-sized IRS (N = 25), achieves a range extension exceeding four times that of the scenario without an IRS.

The rest of the chapter is organized as follows. Section 4.1 describes the system model and assumptions. Section 4.2 presents the problem formulation. Section 4.3 presents the conventional optimization based approach to the problem, whereas Section 4.4 presents the design, learning policy, training and testing of the proposed DL based solution. Section 4.5 presents and discusses the numerical results, including comparison of the proposed scheme with several benchmarks and complexity analysis. Finally, Section 4.6 concludes the chapter.

4.1 System Model

We consider a monostatic BackCom system assisted by an IRS with N passive reflecting elements located nearby. The main components of the system are a reader with M antennas, a single antenna backscatter tag and the aforementioned IRS with N elements. We model the system in a three dimensional setup as shown in Fig. 4.1. A summary of the main mathematical symbols used in the chapter is given in Table. 4.1

The tag to reader, tag to IRS and IRS to reader distances are given by $d_{\text{T-R}}$, $d_{\text{T-I}}$, and $d_{\text{I-R}}$ respectively. The reader transmits a continuous wave signal with power P_t and beamforming vector $\mathbf{w}$ to power the tag's communication where $\|\mathbf{w}\|^2 \leq P_t$. The tag modulates its data on the incoming signal by intentional impedance mismatch. We consider a semi-passive tag, i.e., it has a backup battery. In the ON state, a portion of the incoming signal is used to power the tag, while the rest is reflected. The power splitting coefficient of the tag is α and represents the fraction of the incoming signal to be reflected[1], while the fraction $1-\alpha$ of the signal energy is used to power the tag circuit. In the absence of an incoming signal the tag utilizes the backup battery.

[1]From a practical perspective, the tag's circuitry design is kept simple with α fixed at a feasible value which keeps the tag powered under all channel conditions. This feasible value is calculated based on tag power constraint, i.e., $(1-\alpha)\eta \left|h_{T-R} + \mathbf{v}^H \phi_{\mathbf{T-I-R}}\right|^2 \geq \zeta$ where $\zeta = 8$ dB [82].

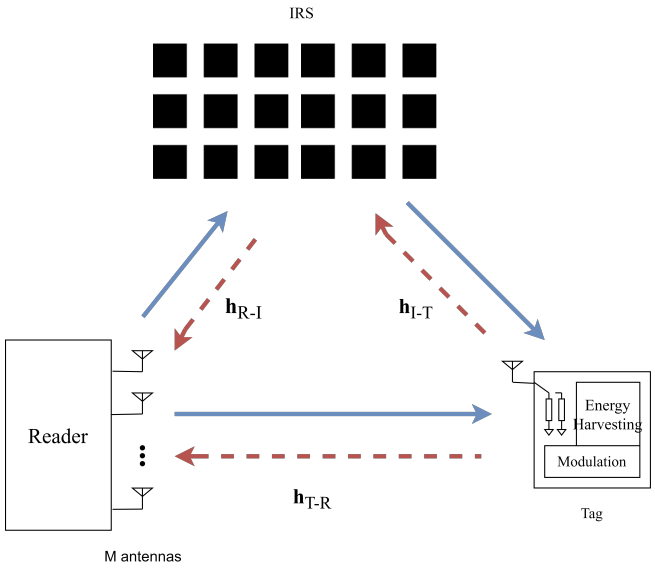

Figure 4.1: Illustration of the system model.

The IRS is assumed to be equipped with its own power supply and a smart controller, which is connected to the reader via a separate reliable wireless link and is responsible for coordinating their operation as well as exchanging information such as reflection coefficients. As the tag performs diffuse reflection, we ignore the signals reflected two or more times at the tag due to severe power loss [115]. However, for the paths in which IRS is involved, we also consider the signals that undergo two reflections at the IRS, i.e., the signal going through the reader-IRS-tag-IRS-reader link [82].

We assume all the channels to be quasi-static, frequency non-selective and constant in each fading block with independent and identically distributed (i.i.d.) Rician fading. Let $\mathbf{h}_{\text{T-R}} \in \mathbb{C}^{M\times 1}$, $\mathbf{H}_{\text{I-R}} \in \mathbb{C}^{M\times N}$ and $\mathbf{h}_{\text{T-I}} \in \mathbb{C}^{N\times 1}$ denote the baseband equivalent channels from the tag to the reader, the IRS to the reader and the tag to the IRS, respectively. Thus, if the signal sent out by the reader is denoted by s and $\mathbf{w}$ stands for the transmit beamforming vector of the reader, the signal arriving at the tag directly from the reader is given by

$$x_{\text{R-T}} = \sqrt{P_t \beta_{\text{T-R}}} \mathbf{h}_{\text{T-R}}{}^H \mathbf{w} s, \tag{4.1}$$

where $\beta_{\text{T-R}} = k_0 (d_0/d_{\text{T-R}})^{-a}$ is the path-loss for the direct reader to tag path with k_0 being the constant attenuation for path-loss at a reference distance of d_0 and a being the path-loss exponent. The signal arriving at the tag after going through reflection at the

Table 4.1: Important symbols used in this chapter

Symbol	Description
M	Number of antennas at the reader
N	Number of IRS elements
γ_b	SNR of the backscatter signal
$\mathbf{h}_{\text{T-R}}$	Tag to reader channel
$\mathbf{H}_{\text{I-R}}$	IRS to reader channel
$\mathbf{h}_{\text{T-I}}$	Tag to IRS channel
$\mathbf{\Phi}_{\text{T-I-R}}$	Overall tag-IRS-reader channel
P_t	Transmit power of reader
$\beta_{\text{T-R}}$	Tag to reader pathloss
$\beta_{\text{I-R}}$	IRS to reader pathloss
$\beta_{\text{T-I}}$	Tag to IRS pathloss
$\mathbf{w}$	Beamforming at the reader
$\mathbf{v}$	IRS reflection pattern
α	Power splitting ratio
σ	Noise power
γ_{m_1}	Minorizer to the objective function
$\mathbf{H}_D$	Combined channel information of $\mathbf{h}_{\text{T-R}}$ and $\mathbf{\Phi}_{\text{T-I-R}}$
$\mathcal{L}$	Loss function
$\mathcal{B}$	set of all batches of input data
B	Batch size
${\mathbf{H}_{\text{D}}}^b$	b^{th} batch
$\mathbf{\Theta}$	Network parameters
(h_p, u_p)	Size of average pooling
FC_v	Fully connected layer for $\mathbf{v}$
FC_w	Fully connected layer for $\mathbf{w}$

IRS is given as

$$x_{\text{R-I-T}} = \sqrt{P_t \beta_{\text{T-I-R}}} \mathbf{v}^H {\mathbf{\Phi}_{\text{T-I-R}}}^H \mathbf{w} s, \tag{4.2}$$

where $\mathbf{\Phi}_{\text{T-I-R}} = \text{diag}(\mathbf{h}_{\text{T-I}})\mathbf{H}_{\text{I-R}}$, $\mathbf{w}$ is the transmit beamforming at the reader and $\mathbf{v} = \left[e^{j\theta_1}, \ldots, e^{j\theta_N}\right]^T$ represents the reflection vector of the IRS such that $|v_n| = 1,\ \forall n \in \{1, \ldots, N\}$ and $\theta_n \in [0, 2\pi)$. The path-loss $\beta_{\text{T-I-R}}$ for the IRS involving channels is modelled according to [128]. The overall signal received at the tag over both the direct and IRS reflecting links is given by,

$$x_{\text{T}} = \sqrt{P_t} \left(\sqrt{\beta_{\text{T-R}}} \mathbf{h}_{\text{T-R}} + \sqrt{\beta_{\text{T-I-R}}} \mathbf{\Phi}_{\text{T-I-R}} \mathbf{v} \right) \mathbf{w} s, \tag{4.3}$$

Then, based on channel reciprocity (which is an accepted practice in monostatic backscatter systems [70,81]), the backscattered signal from the tag, received at the reader is given

by,

$$y_{\mathrm{R}} = \sqrt{\alpha P_t} \quad \mathbf{w}^H \left(\sqrt{\beta_{\text{T-I-R}}}\mathbf{h}_{\text{T-R}} + \sqrt{\beta_{\text{T-I-R}}}\mathbf{\Phi}_{\text{T-I-R}}\mathbf{v}\right). \\ \left(\sqrt{\beta_{\text{T-I-R}}}\mathbf{h}_{\text{T-R}} + \sqrt{\beta_{\text{T-I-R}}}\mathbf{\Phi}_{\text{T-I-R}}\mathbf{v}\right)^H \mathbf{w}x + n, \tag{4.4}$$

where $n \sim \mathcal{CN}(0, \sigma^2)$ is the AWGN and σ^2 is the noise power. For the sake of simpler notation, from here onwards, we adopt a consolidated notation wherein the path-losses for each link are assumed to be absorbed in the respective channel coefficient, i.e., $\mathbf{h}_{\text{T-R}}$ and $\mathbf{\Phi}_{\text{T-I-R}}$ represent the channel fading as well as the path-loss for these respective links. The SNR of the backscatter signal received at the reader is thus given by,

$$\gamma_b = \frac{\alpha P_t \quad \left|\mathbf{w}^H \left(\mathbf{h}_{\text{T-R}} + \mathbf{\Phi}_{\text{T-I-R}}\mathbf{v}\right)\left(\mathbf{h}_{\text{T-R}} + \mathbf{\Phi}_{\text{T-I-R}}\mathbf{v}\right)^H \mathbf{w}\right|^2}{\sigma^2}. \tag{4.5}$$

4.2 Problem Formulation

The goal behind using the IRS to assist the BackCom system is to improve the strength of the backscatter signal arriving at the reader. To this end, we need to jointly optimize the beamforming at the multi-antenna reader $\mathbf{w}$ and the IRS reflection pattern $\mathbf{v}$. This joint optimization problem for maximizing the signal-to-noise ratio γ_b of the backscatter signal received at the reader is given by,

$$\mathrm{P}_1 : \max_{\mathbf{v},\mathbf{w}} \quad \gamma_b(\mathbf{v}, \mathbf{w}) \tag{4.6a}$$

$$\text{s.t.} \quad |v_n| = 1, \ \forall n \in \{1, 2, \ldots N\}, \tag{4.6b}$$

$$\mathbf{w}^H\mathbf{w} \leq P_t, \tag{4.6c}$$

where (4.6c) is the transmit power constraint of the reader with P_t being the maximum transmit power at the reader.

To optimize the active beamforming at the reader and the passive beamforming at the IRS, the channel knowledge is required. Even with the channel knowledge available, we note that it is difficult to solve P_1 as the objective function is highly non-convex, although the constraints are convex. Therefore, we leverage the universal approximation property of the neural networks [129] and propose a convolutional neural network based solution named *BackIRS-Net* which provides predictions of optimal IRS phase shifts and beamforming at the reader based on channel knowledge.

4.3 Conventional Convex Optimization based Solution

In the following, we consider P_1 for the single and multi-antenna cases respectively.

4.3.1 Single Antenna Case

For the single antenna case, P_1 can be written as,

$$\mathrm{P}_2 : \max_{\mathbf{v}} \quad \gamma_b(\mathbf{v}) \tag{4.7a}$$

$$\text{s.t.} \quad |v_n| = 1, \ \forall n \in \{1, 2, \dots N\}, \tag{4.7b}$$

where $\gamma_b = |\mathbf{h}_{\text{T-R}} + \mathbf{\Phi}_{\text{T-I-R}}\mathbf{v}|^2$.
For this problem, a closed form solution exists, i.e., the optimal IRS reflection pattern is the one that aligns the direct and via IRS links [81] and is given by

$$\mathbf{v}^* = e^{j\arg(\mathbf{h}_{\text{T-R}}^{\dagger}\mathbf{\Phi}_{\text{T-I-R}})}. \tag{4.8}$$

4.3.2 Multi-Antenna Case

As noted before, the problem P_1 for $M \geq 2$ is highly non-convex and its optimal solution is intractable. Generally, there is no standard method for solving such non-convex problems optimally. Following similar approaches in the literature, we assume maximum-ratio transmission (MRT) and maximum-ratio combining (MRC) for transmit and receive beamformings as these are known to maximise signal to noise ratio for a given set of IRS phase shifts [107, 130]. Consequently, (4.5) becomes,

$$\gamma_b = \frac{\alpha P_t \ \ |\mathbf{h}_{\text{T-R}} + \mathbf{\Phi}_{\text{T-I-R}}\mathbf{v}|^4}{\sigma^2}. \tag{4.9}$$

Let $\mathbf{H} = \left(\frac{\sqrt[4]{\alpha P_t}}{\sqrt{\sigma}}\right)\begin{bmatrix}\mathbf{h}_{\text{T-R}} & \mathbf{\Phi}_{\text{T-I-R}}\end{bmatrix}$ and $\overline{\mathbf{v}} = \begin{bmatrix}1 \\ \mathbf{v}\end{bmatrix}$ be of dimensions $M \times (N+1)$ and $(N+1) \times 1$ respectively. Then (4.9) becomes,

$$\gamma_b = |\mathbf{H}\overline{\mathbf{v}}|^4 = \left| \overline{\mathbf{v}}^H\mathbf{H}^H\mathbf{H}\overline{\mathbf{v}}\right|^2 = \left|\overline{\mathbf{v}}^H\mathbf{G}\overline{\mathbf{v}}\right|^2 = \overline{\mathbf{v}}^H\mathbf{G}\overline{\mathbf{v}}\overline{\mathbf{v}}^H\mathbf{G}\overline{\mathbf{v}}, \tag{4.10}$$

where $\mathbf{G} = \mathbf{H}^H\mathbf{H}$ and is symmetric. P_1 thus gets transformed into the following optimization problem

$$\mathrm{P}_3 : \max_{\overline{\mathbf{v}}} \quad \overline{\mathbf{v}}^H\mathbf{G}\overline{\mathbf{v}}\overline{\mathbf{v}}^H\mathbf{G}\overline{\mathbf{v}} \tag{4.11a}$$

$$\text{s.t.} \quad |\overline{v_n}| = 1, \ \forall n \in \{1, 2, \dots N\}. \tag{4.11b}$$

The objective function (4.16a) in P_3 is a quartic polynomial in $\mathbf{v}$. If we transform the problem to express the objective function in terms of trace of $\mathbf{GV}$ where $\mathbf{V} = \overline{\mathbf{v}}\overline{\mathbf{v}}^H$ is rank one, then $\mathbf{G}$ is not positive semi-definite in general and leads to a non-convex term in (4.16a). In addition, optimizing multivariate polynomials of higher degrees is an NP-hard problem [121]. Therefore, a closed-form, optimal solution is generally not available. We resort to the MM algorithm [82, 84] to solve this problem, which entails using a series of convex approximations to the original objective function and then optimizing them till convergence.

In the MM algorithm we take a minorizer with bounded curvature, i.e., $f(\mathbf{x}) : \mathbb{C}^N \to \mathbb{R}$ to the objective function using the second-order Taylor expansion [122, Lemma 12],

$$f(\mathbf{x}) \geq f(\mathbf{x}_0) + \mathrm{Re}\left\{\nabla f(\mathbf{x}_0)^H(\mathbf{x} - \mathbf{x}_0)\right\} - \frac{\ell}{2}\left\|\mathbf{x} - \mathbf{x}_0\right\|^2, \tag{4.12}$$

where $\mathbf{x}_0 \in \mathbb{C}^N$ is the point where the original function and the minorizer intersect, ∇ is the gradient operator and ℓ is the maximum curvature of $f(\mathbf{x})$. According to (4.12), the minorizer $\gamma_{m_1}(\overline{\mathbf{v}})$ to the objective function $\gamma_b(\overline{\mathbf{v}})$ is given by,

$$\begin{aligned}\gamma_{m_1}(\overline{\mathbf{v}}) = \gamma_b(\overline{\mathbf{v}_0}) + \overline{\mathbf{v}}_0^H\mathbf{Q}(\overline{\mathbf{v}} - \overline{\mathbf{v}}_0) + (\overline{\mathbf{v}} - \overline{\mathbf{v}}_0)^H\mathbf{Q}\overline{\mathbf{v}}_0 \\ - \frac{\ell}{2}\left\|\overline{\mathbf{v}} - \overline{\mathbf{v}}_0\right\|^2,\end{aligned} \tag{4.13}$$

with $\mathbf{Q} = \mathbf{G}\overline{\mathbf{v}}_0\overline{\mathbf{v}}_0^H\mathbf{G} + \mathbf{G}\overline{\mathbf{v}}_0\overline{\mathbf{v}}_0^H\mathbf{G} + c_2\mathbf{G} + c_1\mathbf{G}$ being a Hermitian matrix obtained from the derivative of $\gamma_b(\overline{\mathbf{v}}_0)$. Rearranging, we can express (4.14) as,

$$\gamma_{m_1}(\overline{\overline{\mathbf{v}}}) = \overline{\overline{\mathbf{v}}}^H\mathbf{R}\overline{\overline{\mathbf{v}}} + c, \tag{4.14}$$

where c denotes the cumulative sum of all constant terms and

$$\mathbf{R} = -\begin{bmatrix} \mathbf{I} & -\frac{2}{\ell}\mathbf{Q}\overline{\mathbf{v}}_0 - \mathbf{I}\overline{\mathbf{v}}_0 \\ (-\frac{2}{\ell}\mathbf{Q}\overline{\mathbf{v}}_0 - \mathbf{I}\overline{\mathbf{v}}_0)^H & 0 \end{bmatrix}, \ \overline{\overline{\mathbf{v}}} = \begin{bmatrix} \overline{\mathbf{v}} \\ 1 \end{bmatrix}, \tag{4.15}$$

so that P_3 is simplified to

$$\mathrm{P}_4 : \max_{\overline{\overline{\mathbf{v}}}} \quad \overline{\overline{\mathbf{v}}}^H\mathbf{R}\overline{\overline{\mathbf{v}}} \tag{4.16a}$$

$$\text{s.t.} \quad |\overline{v_n}| = 1, \ \forall n \in \{1, 2, \dots N\}. \tag{4.16b}$$

We let $\overline{\overline{\mathbf{V}}} = \overline{\overline{\mathbf{v}}}\overline{\overline{\mathbf{v}}}^H$ and transform P_4 to

$$\mathrm{P}_5: \quad \max_{\overline{\overline{\mathbf{V}}}} \quad \mathrm{tr}(\mathbf{R}\overline{\overline{\mathbf{V}}}) + k, \tag{4.17a}$$

$$\text{s.t.} \quad \overline{\overline{\mathbf{V}}}_{n,n} = 1, \ \forall n \in \{1, \ldots, N+2\}, \tag{4.17b}$$

$$\overline{\overline{\mathbf{V}}} \succeq 0, \tag{4.17c}$$

$$\mathrm{rank}(\overline{\overline{\mathbf{V}}}) = 1. \tag{4.17d}$$

The rank-one constraint in $\mathcal{P}_5$ can be dropped to form a convex semidefinite program (SDP), which is solvable using CVX [123]. The optimal solution of $\mathcal{P}_5$ is not rank-one. Therefore, we use Gaussian randomization [124], to obtain a sub-optimal solution to $\mathcal{P}_4$ as $\overline{\overline{\mathbf{v}}}$. From this, $\overline{\mathbf{v}}$ is obtained as $\overline{\mathbf{v}} = \left[\frac{\overline{\overline{\mathbf{v}}}}{v_{N+2}}\right]_{(1:N+1)}$. The resulting $(N+1) \times 1$ vector is substituted to find a new approximation to the original objective function for the next MM iteration and this process is continued till the MM algorithm converges. The $\overline{\mathbf{v}}$ obtained at this time yields $\mathbf{v}$ as $\mathbf{v} = \left[\frac{\overline{\mathbf{v}}}{v_{N+1}}\right]_{(1:N)}$.

4.4 Deep Learning Based Solution

In the previous section, the joint optimization was tackled as an alternating optimization problem, where the sub-problems were solved iteratively using MM algorithm. High complexity methods like semidefinite relaxation were applied in each iteration to obtain a sub-optimal solution. Therefore, in spite of the fact that such optimization-based methods provide predictable performances, the computational complexity incurred is formidable. Moreover, for IRS-assisted systems, it has been shown that a larger sized IRS provides better control and flexibility. As noted in subsection 4.5.3, the computational complexity of the SDR based approach increases greatly with the increase in IRS size, which would make practical implementation difficult. In addition, since the solution presented in section 4.3 does not have closed-form expression, a new high complexity solution is required as the channel changes, which is infeasible in practice.

Such issues motivate the use of model-free ML approaches to solve the joint beamforming problem for IRS-assisted systems. The problem P_1 basically entails jointly optimizing the passive beamforming $\mathbf{v}$ at the IRS and the active beamforming $\mathbf{w}$ at the reader which are functions of channel information i.e.,

$$\mathbf{v} = f_v(\mathbf{H}_D), \tag{4.18a}$$

$$\mathbf{w} = f_w(\mathbf{H}_D), \tag{4.18b}$$

while satisfying constraints (4.6b) and (4.6c). Note that $\mathbf{H}_D$ is a matrix that combines the channel information of the direct and via IRS links i.e., $\mathbf{h}_{\text{T-R}}$ and $\mathbf{\Phi}_{\text{T-I-R}}$ as expressed in (4.20). According to the universal approximation theorem, a deep neural network has the capability of approximating any continuous function with arbitrarily small error [131]. Leveraging this property, we propose a DL based framework named *BackIRS-Net* to solve problem P_1. Our proposed neural network takes channel information as input and learns to adjust its parameters (weights and biases) represented by $\mathbf{\Theta}$ to output near optimal values of $\mathbf{v}$ and $\mathbf{w}$. In particular, it provides parameterizations $\mathcal{F}_v$ and $\mathcal{F}_w$ to approximate f_v and f_w from (4.18a) and (4.18b), i.e.,

$$\mathcal{F}_v(\mathbf{H}_D, \mathbf{\Theta}) \sim f_v(\mathbf{H}_D), \tag{4.19a}$$

$$\mathcal{F}_w(\mathbf{H}_D, \mathbf{\Theta}) \sim f_w(\mathbf{H}_D), \tag{4.19b}$$

In the following, we present our proposed framework and describe its feature design, network architecture, learning policy, and training. We also explain how the objective function and the constraints of P_1 are satisfied while training this network.

4.4.1 Feature Design

First of all, we design a suitable feature vector $\mathbf{H}_D$, by pre-processing the channel information, i.e., $\mathbf{h}_{\text{T-R}}$ and $\mathbf{\Phi}_{\text{T-I-R}}$ (the product channel of the reader to IRS and IRS to tag links). Since the existing deep learning modules do not support complex number operations, expressing the channel information in real number format is required. Therefore, we pre-process the input data to obtain a suitable feature matrix $\mathbf{H}_D$ by separating the real and imaginary parts of the channel coefficients and the concatenating them as follows,

$$\mathbf{H}_D = [\text{Re}\{\mathbf{h}_{\text{T-R}}\}, \text{Im}\{\mathbf{h}_{\text{T-R}}\}, \text{Re}\{\mathbf{\Phi}_{\text{T-I-R}}\}, \text{Im}\{\mathbf{\Phi}_{\text{T-I-R}}\}], \tag{4.20}$$

where $\mathbf{H}_D$ is of dimension $M \times 2(N+1)$. Thus, given that the batch size of a data sample is B, the data dimension of the network input is $B \times M \times 2(N+1)$. The network predicts the phase of the passive beamforming $\angle\mathbf{v}_{\text{pred}} \in \mathbb{R}^{B\times N\times 1}$ and the active beamforming $\mathbf{w}_{\text{pred}} = [\text{Re}\{\mathbf{w}_{\text{pred}}\}, \text{Im}\{\mathbf{w}_{\text{pred}}\}] \in \mathbb{R}^{B\times 2M\times 1}$.

4.4.2 Network Architecture

In our scenario, a unique coupling exists between the $\mathbf{w}$ at the reader and $\mathbf{v}$ at the IRS, in that the optimal transmit beamforming matrix depends on the effective channel con-

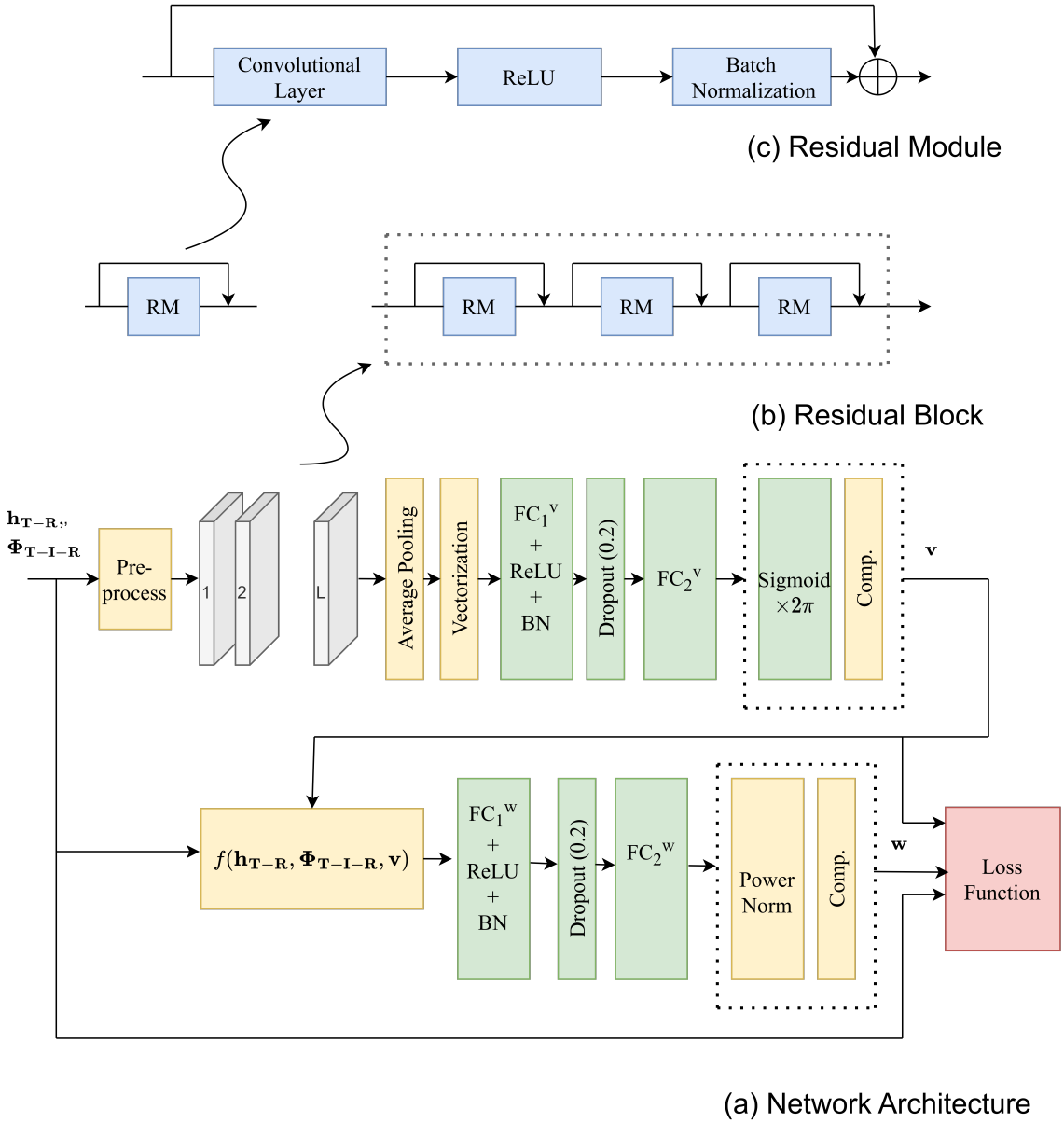

Figure 4.2: Structure of the proposed *BackIRS-Net*.
RM: Residual Module, FC: Fully Connected layer, Comp: Converts $\mathbf{v}$ from angle to complex form, BN: Batch Normalization.

structed by the original channels and $\mathbf{v}$. Therefore, we design the network architecture accordingly. The network first learns $\mathbf{v}$ from the channel input, which is then combined with the channel information to form the effective channel, i.e., $(\mathbf{h}_{\text{T-R}} + \mathbf{\Phi}_{\text{T-I-R}}\mathbf{v}_{\text{pred}})$, followed by normalization to learn $\mathbf{w}$.

In the single antenna reader case, a simple multi-layered perceptron (MLP) network consisting of L fully-connected (also known as linear) layers can provide a sufficiently accurate prediction of $\mathbf{v}$ as demonstrated in [91]. However, in the multi-antenna reader scenario, due to the higher dimension of the input features, the MLP does not perform as well. Although in general, a deeper neural network (with more layers) is more efficient in parameterizing functions, it requires more computational complexity in term of running time and CPU/GPU memory and sometimes suffers from gradient vanishing and exploding issues [132]. To solve these issues, we added ResNet feature to the convolutional neural network, leading to the design of a Deep Residual Convolutional Neural Network (DRCNN). ResNet is a widely used structure in deep learning aided wireless systems design [133]. Thus, we propose to employ a Deep Residual Convolutional Neural Network (DRCNN) based framework named *BackIRS-Net*.

BackIRS-Net is composed of L residual blocks, with each block comprising one or more residual modules as shown in Fig. 4.2. The formula of a residual module is given as

$$\mathbf{x}_{j+1} = \mathbf{x}_j + g(\mathbf{x}_j, \mathbf{\Theta}_j) \tag{4.21}$$

where $\mathbf{x}_{j+1}$ and $\mathbf{x}_j$ are the output and input of the j^{th} module in each residual block, $g(\cdot)$ is the function performed by the module and $\mathbf{\Theta}_j$ are the parameters of the j^{th} module. In our case, each residual module has a convolutional layer, followed by a non-linear activation function, which in this case is the rectified linear unit (ReLU). It is followed by a batch-normalization (BN) layer to facilitate network learning speed and to lend stability to the network. So in this case, the function $g(\cdot)$ of the block can be given as $g(\cdot) = \text{Conv} + \text{ReLU} + \text{BN}$. The sizes of convolutional layers for different size IRS is given in Table 4.2.

The DRCNN is structured such that the first residual block, has only one residual module of size $[C, 3, 3]$, where $C = 128$, followed by residual blocks $\{2 \dots L-1\}$ with three residual modules per block having convolutional layers of sizes given as $[2^{l-1}C, 3, 3] \times 3$, and the L^{th} block having size $[K, 3, 3] \times 3$ where K depends upon the size of average pooling (h_p, u_p) as $K = \frac{4096}{h_p u_p}$. The size and number of the residual blocks depends on N and M. The details of network sizes based on the values of N and M is given in

Table 4.2: Hyperparameters of *BackIRS-Net* (for notation simplicity, batch dimension is excluded)

N	L	Size of l^{th} Residual Block				FC Layers: $\mathbf{v}$		FC Layers: $\mathbf{w}$	
		$l=1$	$l=2$	$l=3$	$l=4$	${FC_1}^v$	${FC_2}^v$	${FC_1}^w$	${FC_2}^w$
16	2	$[128,3,3]$	$[K,3,3]\times 3$	-	-	256	N	128	$2M$
20	3		$[256,3,3]\times 3$	$[K,3,3]\times 3$	-				
25	3				-				
36	4			$[512,3,3]\times 3$	$[K,3,3]\times 3$				
50	4								

Table 4.2.

The phase of the input channels is extracted, concatenated and normalized to form the network input, as shown in Fig. 4.2 (a). The residual blocks are followed by an adaptive average pooling layer of size (h_p, u_p).[2]. This is followed by two fully-connected (FC) layers of sizes 256 and N. The first fully connected layer is followed by a ReLU activation function and a BN layer. To predict the phase of $\mathbf{v}$, the second FC layer is followed by a Sigmoid activation function and a scaling by a factor of 2π. The *Comp.* block in the figure converts $\mathbf{v}$ from angle to complex form as $\mathbf{v}_{\text{pred}} = \cos(\angle \mathbf{v}_{\text{pred}}) + j\sin(\angle \mathbf{v}_{\text{pred}})$.

Furthermore, for the network to predict $\mathbf{w}$, the input channel information is combined with complex value of $\mathbf{v}_{\text{pred}}$ to form the effective channel as $(\mathbf{h}_{\text{T-R}} + \mathbf{\Phi}_{\text{T-I-R}}\mathbf{v}_{\text{pred}})$, which is then split into real and imaginary parts and then concatenated together to obtain a matrix of dimension $B \times 2M$. The effective channel is then normalized. The operations of combining channel information with $\mathbf{v}_{\text{pred}}$ and normalization is represented by $f(\mathbf{h}_{T-R}, \mathbf{\Phi}_{T-I-R}, \mathbf{v}_{pred})$ and then fed into a 2-layer MLP, with the FC layers of sizes 128 and $2M$ to predict $\mathbf{w}$. The first FC layer is followed by ReLU activation and BN layer, while the last layer is followed by power normalization for $\mathbf{w}$, which is explained in subsection 4.4.4. The *Comp.* block after the power normalization converts $\mathbf{w}$ into its complex form.

4.4.3 Learning Policy

We propose to train the neural network using unsupervised learning. The main reasons for employing unsupervised learning are, i.e.,

- Supervised Learning requires labelled data or in other words, ground truth/optimal solution. The network is then trained to minimize the empirical mean squared error between the output of the neural network and the ground truth/optimal solution.

[2]Through extensive experiments, we determined (h_p, u_p) as $(1, 32)$, as in this scenario the receiving field is over all the weights, which facilitates learning

Algorithm 1 BackIRS-Net Training and Testing

Initialization: $e_t = 0$, ${\mathbf{H}_\mathrm{D}}^{\mathrm{train}}$ as input

Offline Training Phase:

Input: Training dataset: ${\mathbf{H}_\mathrm{D}}^{\mathrm{train}}$
  for $e_t \leq$ maximum number of epochs, **do**
    Update $\boldsymbol{\Theta}$ by backpropagation algorithm to minimize $\mathcal{L}(\boldsymbol{\Theta})$
    Update epoch number $e_t \leftarrow e_t + 1$.
  end while
  Output: Well-trained BackIRS-Net with $\mathcal{F}_{v^*}(\cdot)$ and $\mathcal{F}_{w^*}(\cdot)$

Online Evaluation Phase:

Input: Test dataset: ${\mathbf{H}_\mathrm{D}}^{\mathrm{test}}$ as input
  do Pass the input through the network
  Output: $\mathbf{v}_{\mathrm{test}} = \mathcal{F}_{v^*}({\mathbf{H}_\mathrm{D}}^{\mathrm{test}})$ and $\mathbf{w}_{\mathrm{test}} = \mathcal{F}_{w^*}({\mathbf{H}_\mathrm{D}}^{\mathrm{test}})$

Since we only have a sub-optimal solution in this scenario, it is not practical to train the neural network on sub-optimal data.

- For a model trained using supervised learning, at run time, the test data may not always be in the same distribution as the training data, i.e., the model cannot be well generalized to unseen data, especially under a different data collection environment. In contrast, unsupervised learning models usually benefit from a better generalization to dataset bias because of the learning of implicit structures of unlabelled data.

- Although the constraints in the optimization problem can be implicitly reflected in the ground truth labels for the training data, it is hard for the neural network to learn the constraints in supervised learning.

We design the unsupervised learning framework by defining the loss function of *BackIRS-Net* inspired by the objective function of P_1. To maximize γ_b in P_1, the neural network that minimizes a customized loss function $\mathcal{L}$, which is defined as the negative of the received SNR γ_b at the reader, i.e.,

$$\mathcal{L} = \frac{-1}{|\mathcal{B}|} \sum_{{\mathbf{H}_\mathrm{D}}^b \in \mathcal{B}} \gamma_b({\mathbf{H}_\mathrm{D}}^b, \mathbf{v}, \mathbf{w}, \boldsymbol{\Theta}), \tag{4.22}$$

where $\mathcal{B}$ is the set of all batches of input data, ${\mathbf{H}_\mathrm{D}}^b$ is a single data batch, $\boldsymbol{\Theta}$ are the network parameters and $\mathbf{v}$ and $\mathbf{w}$ are the network outputs for passive and active

beamforming respectively.

An *offline training phase* is first employed to train *BackIRS-Net* in which the network takes input training data and learns to adjust its parameters to minimize the loss function given in (4.22). Afterwards, during the *evaluation phase*, the well trained network is used to proved an approximate solution to P_1. The complete learning paradigm is presented in Algorthim 1.

4.4.4 Meeting the Constraints of P_1

Since the network is trained using unsupervised learning, proper scaling activation functions are required to ensure that the outputs satisfy the constraints in problem P_1. In particular, to satisfy constraint (4.6b), a Sigmoid activation function is used after the last FC layer for producing $\mathbf{v}$ followed by a scaling factor of 2π. Similarly, to meet the constraint (4.6c), power normalization is carried out after the last layer of the network to obtain $\mathbf{w}_{\text{out}}$ as

$$\mathbf{w}_{\text{out}} = \sqrt{P}\frac{\mathbf{w}}{\|\mathbf{w}\|}. \tag{4.23}$$

4.4.5 Network Training

The proposed network is trained offline over a large data set comprising of a variety of channel realizations to obtain a robust estimation performance. The dataset is split into training, validation and test datasets in the ratio 80% : 10% : 10%. To train the network, Adam optimizer is used. The network is trained for several epochs to minimize the loss function described in (4.22).The number of training epochs required depends upon the IRS size.The training data is split into minibatches and is shuffled at the beginning of each epoch to ensure sufficient randomness to avoid overfitting while training. In each epoch, the network minimizes the loss function on each minibatch. After every epoch, the network validates its performance on the validation dataset. A dropout of 20% is used after each FC layer to avoid overfitting. The training parameters are outlined in Table 4.3.

4.5 Results

In this section, we conduct a numerical investigation to evaluate the performance of our proposed scheme presented in Section 4.4 and to compare it with several benchmarks. We present the performance improvement brought about by our proposed scheme in terms

Table 4.3: Values of Parameters used in Section. 4.5

Parameter	**Value**
Minibatch Size	50
Learning Rate	10^{-3}
L2 Regularization	10^{-7}
Dropout	20%
Train/Val/Test Data Split	80%:10%:10%
Size of Training Dataset	10^5

of the enhancement of received effective SNR at the reader. In addition, we quantify the range extension brought about by the assistance of IRS. Lastly, we highlight the complexity analysis of our proposed scheme in comparison to the benchmarks.

We consider a monostatic backscatter communication system with the reader emitting continuous wave at a frequency of $f_c = 915$ MHz, which is the typical EPC Gen 2 frequency [63]. For majority of the results presented in this section, the reader, the IRS and the tag are located at $[5, 0, 0]$, $[6, 5, 2]$ and $[15, 0, 0]$ respectively, with all the 3-D coordinates in meters. For the results highlighting the range extension of the backscatter tag, the coordinates are described in Section 4.5.2. As mentioned before, all the channels are assumed to have Rician fading with a Rician K- factor of 3dB, from the typical range in [134] after conversion from the Nakagami parameter. The path loss exponent is chosen as $a = 2.5$ to account for sparse scatterers in the environment. The SNR requirement for the tag is assumed to be 8 dB [18]. For the optimization carried out in section 4.3, the convergence threshold for the AO-based algorithm is set to $\epsilon = 1e - 4$, which is a stricter version of the one used in [107]. The values of the rest of system parameters are: $\alpha = 0.7$, $P_t = 30$ dBm and $\sigma^2 = -80$ dBm. Unless explicitly stated otherwise, we have used $M = 4$ antennas at the reader.

For the DRCNN training, the size of the data set is $1e5$ which split into training, validation and test data in the ratio of $80 : 10 : 10$.The rest of the training parameters are outlined in Table 4.3. The training is performed on a Nvidia V100 GPU within the National Computational Infrastructure (NCI Australia). The training progress of the DRCNN is shown in Fig. 4.3. Since the network is being trained in unsupervised fashion, the loss function which is based on the negative of SNR, starts with a larger value in the beginning, due to random weights assigned to the network at the start of the training. However, as the training progresses, the network learns the underlying pattern of the training data, and with ample training iterations, the two curves become parallel and the loss is minimized, which in turn means that the SNR is maximized.

The number of iterations of the training process depends upon the DRCNN size, which in turn depends upon the size of IRS, e.g., for the IRS of size $N = 16$, the network took about 50 iterations to train whereas for the IRS of size $N = 25$ the network took close to 80 iterations to train.

After training *BackIRS-Net*, it is tested on the unseen test data set. The effective SNR of the backscatter link at the reader is chosen as a metric to evaluate our proposed DRCNN. For comparison, we consider the following benchmarks,

- Monostatic BackCom system without IRS.
- IRS-assisted monostatic BackCom system with random values for $\mathbf{v}$ and MRT/MRC for $\mathbf{w}$.
- IRS-assisted monostatic BackCom system with $\mathbf{v}$ and $\mathbf{w}$ obtained using the approach presented in Section 4.3.
- IRS-assisted monostatic BackCom system with $\mathbf{v}$ and $\mathbf{w}$ obtained by a trained MLP (5 layers with $20N$ neurons in each and each layer followed by ReLU and BN).

4.5.1 Improvement in Effective SNR

Fig. 4.4 plots the effective SNR of the combined direct and via IRS link traversed by the backscatter signal to arrive at the reader, as function of the IRS size, for $M = 4$. It can be seen that the increase in IRS size improves the SNR at the reader, which is intuitive since a larger IRS enhances the effective gain of the reflecting path in the forward as well as the backscatter link. Moreover, the rate of increase in effective SNR with increasing N slightly levels off as N increases.

Comparing the results of the proposed scheme with the benchmarks we can see that the performance of the system without the IRS is worst, whereas for the system including an IRS with random phase shifts, there is a marginal improvement over the baseline (no IRS) case. However, for the proposed scheme and the benchmarks with an optimized IRS (SDR based approach and MLP), there is a marked improvement.

Comparing the plot for *BackIRS-Net* with the benchmarks optimizing the IRS, we note that the plot for the SDR based approach sits at the highest SNR. The performance of *BackIRS-Net* is close to the SDR based approach with a gap of about 1 dB. However, the computational complexity of of the trained *BackIRS-Net* is orders of magnitude less than the SDR based approach as highlighted in Section 4.5.3. When deploying the system in real time, the computational complexity and time is crucial as the new values of

$\mathbf{v}$ and $\mathbf{w}$ need to be calculated every time the channel information changes. The ease and speed of computation afforded by a trained DRCNN is an important improvement over the conventional optimization based approach in this regard. Moreover, we can see that as N increases the performance gap between the two plots decreases. This further highlights the usefulness of our proposed scheme, i.e., with a larger IRS, we can achieve highly comparable performance to the conventional optimization based approach at much less computational cost.

Furthermore, we note that *BackIRS-Net* performs better than the MLP. This is due to the fact that the input data is in matrix form due to the multi-antenna reader and IRS. The DRCNN is capable of providing a more enriched mapping by having a larger receptive field over neighbouring channels. Even with a 5 layer deep MLP with $20N$ neurons in each layer, we can see that for each value of N, the SNR is limited to a certain value and does improve further. Making the MLP larger can lead to overfitting and also poses the risk of vanishing or exploding gradients. *BackIRS-Net* performs better than the MLP as the convolutional layers are able to extract spatial information better. Moreover, by encapsulating the convolutional layers within residual modules the gradient flow is facilitated, which leads to easier and more robust training, even with larger network size.

Fig. 4.5 illustrates the performance of *BackIRS-Net* for different values of number of receive antennas M at the reader, for $N = 16$. It can be seen that the performance improves for all benchmarks with the increase of M, due to the increased capability of beamforming at the reader. Again, it can be seen that our proposed DRCNN performs better than the MLP. Its performance gap with the SDR based approach is also meager. It is also notable that increasing M by 2 creates a performance improvement in SNR by 2 - 3 dB. Comparing it with Fig. 4.4, we note that going from an IRS of size $N = 16$ to $N = 20$, SNR increases from 23.5 dB 28 dB. Having more antennas at the reader is costly as compared to using a larger passive IRS assisting the system for SNR improvement. Moreover, the IRS aided system has the flexibility of increasing the range of BackCom system by switching to a larger IRS, without any changes to the structure of the reader or the tag.

Next we explore the impact of IRS position on the SNR of backscatter signal at the reader. For this, we fix the reader at $[5, 0, 0]$ and the tag at $[30, 0, 0]$. The y and z coordinates of the IRS are fixed at for three different placements of the IRS is shown in Fig. 4.6. We maintain the y and z- coordinates of the IRS at 5 and 2 respectively, and move the x- coordinate from 0 to 35 in a straight line, parallel to the x-axis, from the reader to the tag and observe the impact on the effective SNR.

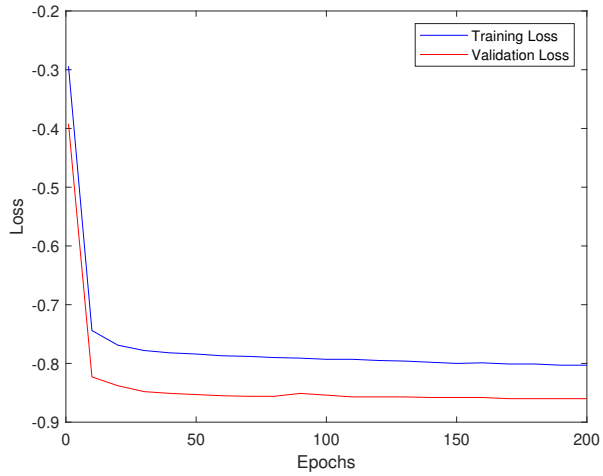

Figure 4.3: Training Progress of *BackIRS-Net* for $N = 16, M = 4$.

From the plot it is evident that the SNR is maximum when the IRS is placed between reader and the tag and when it is either closest to the reader or to the tag, e.g., the curve hits a peak when the IRS is placed at $[6, 5, 2]$ with the reader being at $[5, 0, 0]$. However, when the IRS is moved in either direction parallel to the x-axis, i.e., to $[5, 5, 2]$ or $[7, 5, 2]$, the SNR decreases. Similar behaviour is observed when the IRS is moved to different locations along x-axis close to the tag. The SNR is minimum when the IRS is at $[17.5, 5, 2]$, i.e., halfway between the reader and the tag. e further observe that the plot is fairly symmetrical around the mid-point exhibiting minimum SNR. This indicates that for the IRS aided monostatic BackCom system, best performance in terms of SNR enhancement is achieved when the IRS is placed either close to the reader or to the tag.

The network requires offline training prior to deployment for a certain system configuration/location of system components. However, to demonstrate the generalization of the network to different datasets corresponding to different channel conditions, we have performed simulations using four test datasets with channels corresponding to Rician fading with a K- factor of : 3, 6, 9 , 10. These are processed using the neural network trained on dataset corresponding to K = 9. The average SNR achieved for each of these test datasets is:

For dataset corresponding to K = 9: SNR = 42.7dB

For dataset corresponding to K = 10: SNR = 41.618dB

For dataset corresponding to K = 6: SNR = 40.805dB

For dataset corresponding to K = 3: SNR = 39.066dB

It is notable that as the channel conditions change, there is some degradation but the

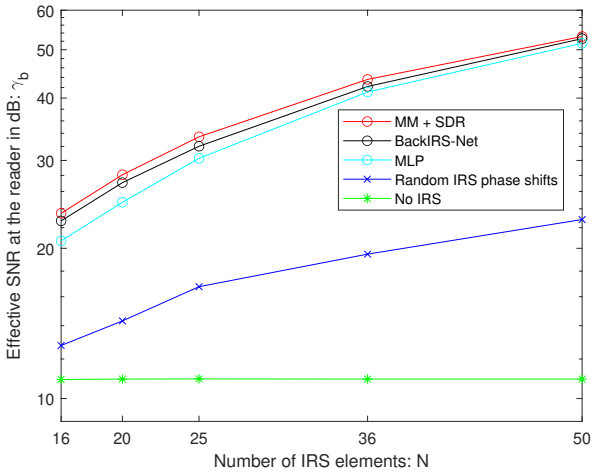

Figure 4.4: Impact of the IRS size on the effective SNR for a fixed M.

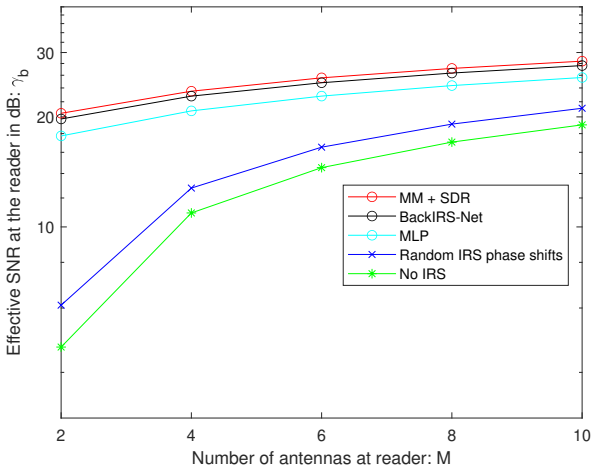

Figure 4.5: Impact of number of antennas at the reader on the effective SNR for a fixed N.

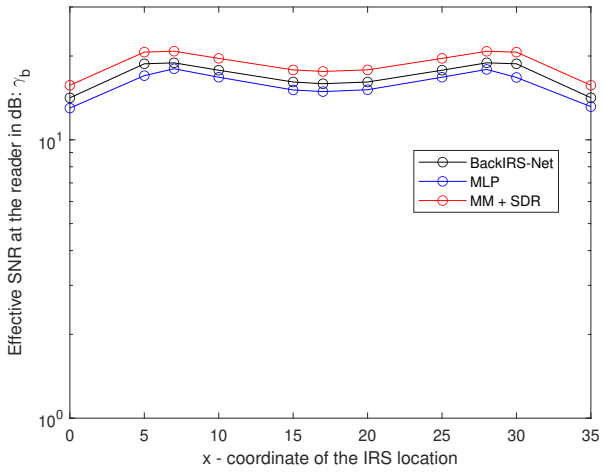

Figure 4.6: Impact of IRS location on the effective SNR for a fixed N.

performance is still acceptable. However, if channel conditions are drastically different, then for best performance, it is expected that *BackIRS-Net* be retrained on a larger dataset covering the highly varied channel conditions.

4.5.2 Range Extension

In this subsection, we investigate the range extension brought about in the BackCom system by the assistance of the IRS. Because of the two-way nature of the backscatter link, the range can be doubled while maintaining the same bit error rate (BER) performance for every 12 dB of SNR improvement [135]. In the previous subsections, we have highlighted the increase in effective SNR received at the reader by the assistance of IRS, while varying different system parameters. Here, we examine and quanitfy the exact range extension in a baseline case.

We first note that in the case of no IRS, when the distance between the reader and the tag is 10m, the effective SNR received at the reader is 10.89 dB as in Fig. 4.4. We consider this value as the baseline case as from literature the received effective SNR of 10 dB at the reader is considered acceptable performance [70, 71]. To illustrate the range extension, we consider the setup in which the reader is kept at $[5, 0, 0]$ and an IRS of size $N = 25$ is kept at $[6, 5, 2]$. The tag is moved from $[15, 0, 0]$ (corresponding to a distance of 10m from the reader as in the baseline case) away from the reader and parallel to the x-axis. In Fig. 4.5.2, plot the effective SNR at the reader as the tag is moved farther from it. It can be seen that the SNR threshold of 10 dB is achieved at a distance of 48

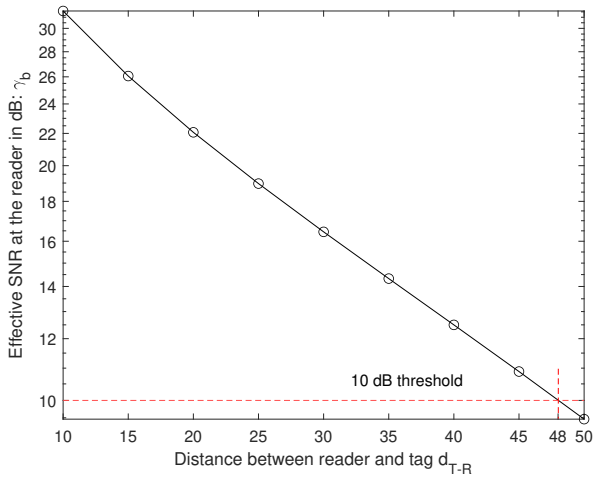

Figure 4.7: Range extension brought about by IRS.

m. Comparing with the baseline case, an SNR of 10.89 dB (which was the received SNR at a distance of 10 m with no IRS), is achieved at a distance of 47 m (increase by a factor of 4.7). Thus, even an IRS of modest size $N = 25$, brings about greater than four-fold increase in the range of the backscatter system.

4.5.3 Complexity Analysis

The SDR based approach presented in section 4.3 incurs a complexity of the order of $O(I(k+2)^{4.5})$, where I is the number MM iterations, and the $(k+1)^{4.5}$ is the SDP complexity [125]. On the other hand, a well-trained *BackIRS-Net* when deployed only has a computational complexity of $O(k^2)$ for the tensor-wise calculation of $\mathbf{v}$ and $\mathbf{w}$.

We have calculated the exact run time of our proposed framework and the SDR based benchmark scheme and present it in the following for N = 50. Both the frameworks were averaged over 10,000 samples. We run the SDR based approach using CPU and the trained *BackIRS-Net* using both CPU and GPU. We show the individual times taken by the part with Residual blocks, the part involving the tensor-wise calculation of $\mathbf{v}$ and $\mathbf{w}$ and the part calculating SNR in Table 4.4. The SDR based approach can only be run on the CPU and as N increases, its run time becomes increasingly large. The proposed neural network, even for N as large as 50, when run on the CPU takes less time (i.e., 9.23 ms) as compared to the SDR based approach. However, the real advantage of neural network comes out when we run it on GPU, i.e., it takes only 2.63 ms. It is important to note that the ResNet block on GPU takes the majority of time , i.e., 70.3% of the total

Table 4.4: Run-time of *BackIRS-Net* and MM-SDR based benchmark

Scheme	**Res Block**	**Linear layers**	**SNR Calc**	**Total Time**
MM-SDR benchmark	-	-	-	62.2 ms
BackIRS-Net CPU	8.52 ms	0.60 ms	0.10 ms	9.23 ms
BackIRS-Net GPU	1.85 ms	0.57 ms	0.21ms	2.63 ms

time. This is irrelevant to the calculation of $\mathbf{v}$ and $\mathbf{w}$ and basically is the time spent in feature extraction. Typically, IRS size used in practice is larger than $N = 50$ and for such large size IRS the SDR approach becomes too slow. However, in such scenarios, the neural network approach is faster as it is parallelizable and is typically run on GPU.

4.6 Conclusion

In this chapter, an IRS-assisted monostatic BackCom system was studied and the problem of maximizing effective SNR of the backscatter at the reader was considered as a means of range extension. This problem of jointly optimizing the passive beamforming at the IRS and the active beamforming at the reader was addressed by proposing a DRCNN named *BackIRS-Net*, which was trained in an unsupervised fashion. The structure of the DRCNN, feature extraction and loss function for training was carefully customized based on the optimization problem and its objective function and constraints. The numerical results demonstrate the effectiveness of using an IRS to enhance BackCom, resulting in substantial range extension. Moreover, the performance of a trained *BackIRS* was shown to be close to the conventional SDR based approach, but with much less computational complexity. Future work can consider extensions of the proposed system to multi-tag configurations.

Chapter 5

Conclusions and Future Research Directions

In this chapter we summarize the key findings of this thesis. In addition, we highlight some potential future research directions related to the work presented in this thesis.

5.1 Summary of Key Findings of Thesis

The work presented in this thesis revolved around examining the potential of synergizing of BackCom with other 6G technologies, with the goal of enhancing the performance and deployment potential of BackCom for future wireless networks. In this regard, we considered the integration of ambient BackCom with retrodirective WPT in chapter 2 and with IRS in chapter 3. In chapter 4, we proposed to address the range extension problem of monostatic BackCom using IRS and leveraging machine learning techniques for joint optimization of the two technologies. A summary of the main findings and contributions from each chapter is presented below.

In chapter 2, we introduced a novel WPT system designed to energize an Energy Receiver (ER). This system combines Retrodirective WPT at the Energy Transmitter (ET) with ambient BackCom at the ER. To address the challenge of direct-link ambient interference, we put forth a unique strategy called "ambient backscatter training." This strategy involves adjusting the reflection coefficient at the ER in a specific pattern to entirely eliminate the formidable direct-link ambient interference. We demonstrated that when the duration of the ambient symbols is known, the switching rate of this pattern becomes inconsequential, and we can switch the backscatter coefficient just twice during each ambient symbol period. However, when the duration of the ambient symbols is

unknown, faster switching proves advantageous in minimizing the impact of uncancelled ambient interference and augmenting harvested power. The most favorable average harvested power is attainable when the interference signal from neighboring ambient sources is notably weaker than the original ambient signal. It is worth noting that our proposed scheme can be extended to accommodate multiple backscatter tags positioned within a designated area.

In Chapter 3 we focused on enhancing the performance of an Ambient BackCom system with the assistance of an Intelligent Reflecting Surface (IRS). We developed a novel approach to improve Bit Error Rate (BER) performance. The primary challenge we addressed was optimizing phase shifts at the IRS to maximize the strength of the backscattered signal received at the RX. This optimization problem was tackled using the semidefinite relaxtion approach within MM algorithm. The outcomes of our research demonstrated a substantial improvement in BER performance when employing a moderately sized IRS to augment the ambient BackCom system. This reduction in BER has the potential to significantly enhance the rate and coverage of such systems. Furthermore, the proposed scheme has the potential for extension to accommodate multiple backscatter devices, allowing for the investigation of the IRS's role in collision avoidance.

In chapter 4, we delved into an IRS-assisted monostatic BackCom system, with a primary focus on extending the communication range by maximizing the effective Signal-to-Noise Ratio (SNR) at the reader. To tackle the intricate challenge of optimizing both passive beamforming at the IRS and active beamforming at the reader simultaneously, we introduced a Deep Residual Convolutional Neural Network (DRCNN) known as BackIRS-Net. This network was trained in an unsupervised manner. The architecture of the DRCNN, along with feature extraction and the loss function used during training, was meticulously tailored to align with the optimization problem's objectives and constraints. Our numerical findings underscore the remarkable effectiveness of employing an IRS to augment BackCom, leading to a substantial extension of the communication range. Furthermore, our trained BackIRS system exhibited performance closely aligned with the conventional Software-Defined Radio (SDR)-based approach but with significantly reduced computational complexity. Future research endeavors could explore the extension of this proposed system to accommodate multi-tag configurations, thereby broadening its applicability and impact in diverse communication scenarios.

5.2 Future Research Directions

This thesis delves into the examination of innovative applications of BackCom integrated with other 6G technologies to provide an overall enhanced performance. Given the exploratory nature of these investigations, a range of potential research directions naturally emerge.

5.2.1 Extending Ambient BackCom Training for WPT to multi-user scenario

The system model presented in Chapter 2 studied the baseline case with only one ER receiving retrodirective WPT from the ET. An important future research direction is to extend that system model to suit a multi-user scenario. Multi-user BackCom is essential for supporting the ever-expanding number of IoT devices and ensuring reliable connectivity in crowded environments. Furthermore, it can ensure that IoT networks can efficiently scale up to accommodate numerous interconnected devices, which is vital for smart cities, industrial automation, and other IoT deployments.

Since BackCom inherently relies on reflecting signals, in multi-user scenarios, managing interference becomes critical to maintain reliable and efficient communication. In this regard, for the multi-user extension of the scheme proposed in Chapter 2, orthogonal training sequences can be used (similar to Hadamard codes), to avoid collision between multiple ERs. Thus, a coordinated multi-user Ambient BackCom training assisted WPT protocol can be investigated.

5.2.2 IRS-aided BackCom Sytems

In this thesis, we investigated the integration of IRS into monostatic and ambient BackCom systems in chapters 3 and 4, aiming to expand their practical applications. In this regard, we considered the use of IRS to enhance the BackCom signal strength. However, with the inclusion of IRS in the systems model, several interesting research questions arise, which are worth investigating:

- **Expanding to multi-user scenario:** In chapters 2 and 3, we considered baseline system models with only one BackCom device to establish the viability of such systems. Extending the system model to multi-user scenario is requisite for actual employability in IoT systems. However, due to the multi-reflection nature of the IRS-aided BackCom systems, the signal model becomes interesting as different

combinations of reflected signals from the IRS and the BackCom devices arise and is worth investigating.

- **Channel Estimation for IRS-aided BackCom Systems:** To reap the benefits of IRS-aided BackCom systems, channel state information acquisition is essential. CSI acquisition for IRS is a fast progressing research direction and the the CSI acquisition schemes being developed solely for IRS can be adapted to suit the IRS-aided BackCom systems. In general, conventional channel estimation schemes can be adapted for IRS -aided BackCom system by turning only two nodes in the system model ON at a time and estimating the relevant channels. Thus, CSI is acquired by going pair-wise among all the nodes in the system till all of the available channels are learnt. In addition, machine learning techniques can be leveraged for channel estimation in IRS-aided BackCom systems.

- **Performance Enhancement:** Achieving optimal system performance involves maximizing data rates, signal-to-noise ratios (SNR), and communication range. This optimization necessitates careful consideration of reader, tag, and IRS parameters. In the research conducted in this thesis, we have considered the problem of BER minimization for IRS-aided ambient BackCom and the problem of range extension in IRS-aided monostatic BackCom. Other aspects of system performance enhancement in all three BackCom architectures aided by IRS are interesting future research directions.

- **Interference Mitigation:** Random access protocols employed by RFID systems often lead to tag collisions. Given IRS's potential to significantly enhance received signal strength at the reader, it raises the question of whether inter-tag interference or collision behavior is positively or negatively affected in this system configuration and is an area worth investigating.

- **Multiple Access:** IRS can be leveraged to assist BackCom in multiple access scenarios, e.g., IRS can be programmed to enable Time division or frequency division multiple access in IRS aided BackCom systems.

- **Adaptive Joint Optimization of IRS and BackCom:** Another important direction for future research is to explore dynamic and reconfigurable IRS surfaces that can adapt in real-time to changing channel conditions and user requirements. This would involve developing algorithms and control mechanisms for dynamic phase tuning and repositioning of IRS elements.

- **Security and Privacy:** Addressing security and privacy concerns in IRS-aided backscatter systems is another significant research area. This would entail investigating secure key exchange, authentication, and encryption techniques tailored to the unique characteristics of these systems.

- **Machine Learning Integration:** Investigating the integration of machine learning and AI algorithms into IRS-aided BackCom systems for adaptive and intelligent control is highly desirable and an interesting research direction. Chapter 4 of this thesis touched upon this topic in the context of monostatic BackCom systems. Developing learning-based approaches for optimizing IRS configuration and to deal with all the aforementioned research challenges is an interesting future research direction based on the ability of machine learning techniques to provide data driven solutions to a variety of research challenges and enhance the overall efficiency and effectiveness of IoT networks.

Appendix A

Appendix A

This appendix contains the proof needed in Chapter 2.

A.1 Proof of Proposition 2.1

We derive the formula for instantaneous energy harvested at the ER during the power transfer phase as given in (2.14). We consider the following two cases:
Case 1: $N_s \leq N_c$ In this case, we have $T_s \geq T_c$. Substituting (2.1) in (2.8) we have

$$\mathbf{x}_s = \frac{\sqrt{\gamma_1\gamma_2 P_s}g\mathbf{f}}{N_c T_c} \int_0^{N_c T_c} \sum_{n=0}^{N_c-1} c_n^2 {p_c}^2(t-nT_c) \sum_{i=1}^{N_s} s_i p_s(t-iT_s)dt, \tag{A.1a}$$

$$= \frac{\sqrt{\gamma_1\gamma_2 P_s}g\mathbf{f}}{N_c T_c} \sum_{i=1}^{N_s} s_i \sum_{n=\frac{N_c}{N_s}(i-1)}^{\frac{N_c}{N_s}i-1} c_n^2 \int_{nT_c}^{(n+1)T_c} {p_c}^2(t-nT_c)dt, \tag{A.1b}$$

$$= \sqrt{\gamma_1\gamma_2 P_s}\frac{g\mathbf{f}}{N_c T_c} \sum_{i=1}^{N_s} \sum_{n=\frac{N_c}{N_s}(i-1)+1}^{\frac{N_c}{N_s}i} c_n^2 s_i T_c, \tag{A.1c}$$

$$= \sqrt{\gamma_1\gamma_2 P_s}\frac{g\mathbf{f}}{N_c}\frac{N_c}{N_s} \sum_{i=1}^{N_s} s_i, \tag{A.1d}$$

$$= \sqrt{\gamma_1\gamma_2 P_s}\frac{g\mathbf{f}}{N_s} \sum_{i=1}^{N_s} s_i, \tag{A.1e}$$

where the integration in (A.1b) comes from the fact that the integration in (A.1a) is being performed for the product of two aligned rectangular pulses $p_c(t)$ and $p_s(t)$ where $T_s \geq T_c$ and the duration of integration is $N_c T_c$. Also, (A.1d) follows from the fact that $c_n^2 = 1$ and $\sum_{n=\frac{N_c}{N_s}(i-1)}^{\frac{N_c}{N_s}i-1} = \frac{N_c}{N_s}$ for any given i.

Next, substituting (2.1) in (2.9) we get

$$\mathbf{x}_i = \frac{\sqrt{\gamma_3 P_s}\mathbf{h}}{N_c T_c} \int_0^{N_c T_c} \sum_{i=1}^{N_s} s_i p_s(t - iT_s) \sum_{n=1}^{N_c} c_n p_c(t - nT_c) dt, \tag{A.2a}$$

$$= \sqrt{\gamma_3 P_s} \frac{\mathbf{h}}{N_c T_c} \sum_{i=1}^{N_s} s_i \sum_{n=\frac{N_c}{N_s}(i-1)}^{\frac{N_c}{N_s}i-1} c_n \int_{nT_c}^{(n+1)T_c} p_c(t - nT_c) dt, \tag{A.2b}$$

$$\mathbf{x}_i = \sqrt{\gamma_3 P_s} \frac{\mathbf{h}}{N_c T_c} \sum_{i=1}^{N_s} \sum_{n=\frac{N_c}{N_s}(i-1)}^{\frac{N_c}{N_s}i-1} c_n s_i T_c, \tag{A.2c}$$

$$= \sqrt{\gamma_3 P_s} \frac{\mathbf{h}}{N_c} \sum_{i=1}^{N_s} \sum_{n=\frac{N_c}{N_s}(i-1)}^{\frac{N_c}{N_s}i-1} c_n s_i, \tag{A.2d}$$

where again the integration in (A.2a) becomes the summation in (A.2c) as mentioned above. Substituting (A.1e) and (A.2d) into (2.11), we get:

$$r_{\mathrm{ER}} = \sqrt{\gamma_2 P_t} \frac{\left(\frac{\sqrt{\gamma_1\gamma_2 P_s} g^*}{N_s} \sum_{i=1}^{N_s} s_i^* \mathbf{f}^T \mathbf{f}^* + \frac{\sqrt{\gamma_3 P_s}}{N_c} \sum_{i=1}^{N_s} \sum_{n=\frac{N_c}{N_s}(i-1)+1}^{\frac{N_c}{N_s}i} c_n s_i^* \mathbf{f}^T \mathbf{h}^* + \mathbf{f}^T \mathbf{n}^*\right)}{\left\| \frac{\sqrt{\gamma_1\gamma_2 P_s} g^*}{N_s} \sum_{i=1}^{N_s} s_i \mathbf{f} + \frac{\sqrt{\gamma_3 P_s}}{N_c} \sum_{i=1}^{N_s} \sum_{n=\frac{N_c}{N_s}(i-1)+1}^{\frac{N_c}{N_s}i} c_n s_i \mathbf{h} + \mathbf{n} \right\|}, \tag{A.3}$$

which simplifies to

$$r_{\mathrm{ER}} = \sqrt{\gamma_2 P_t} \frac{\left(\frac{\sqrt{\gamma_1\gamma_2 P_s} g}{N_s} \sum_{i=1}^{N_s} s_i^* \mathbf{f}^H \mathbf{f} + \frac{\sqrt{\gamma_3 P_s}}{N_c} \sum_{i=1}^{N_s} \sum_{n=\frac{N_c}{N_s}(i-1)+1}^{\frac{N_c}{N_s}i} c_n s_i^* \mathbf{f}^H \mathbf{h} + \mathbf{f}^H \mathbf{n}\right)}{\left\| \frac{\sqrt{\gamma_1\gamma_2 P_s} g}{N_s} \sum_{i=1}^{N_s} s_i \mathbf{f} + \frac{\sqrt{\gamma_3 P_s}}{N_c} \sum_{i=1}^{N_s} \sum_{n=\frac{N_c}{N_s}(i-1)+1}^{\frac{N_c}{N_s}i} c_n s_i \mathbf{h} + \mathbf{n} \right\|}, \tag{A.4}$$

since $\mathbf{f}^T \mathbf{f}^* = \mathbf{f}^H \mathbf{f}$ and $\mathbf{f}^T \mathbf{h}^* = \mathbf{f}^H \mathbf{h}$.
From (A.4) the incident RF power on the ER can be found as,

$$Q_{RF} = |r_{\mathrm{ER}}|^2$$
$$= \left(\frac{\frac{\gamma_1 {\gamma_2}^2 P_s P_t |g|^2}{N_s^2} \left| \sum_{i=1}^{N_s} s_i \right|^2 \|\mathbf{f}\|^4 + \frac{\gamma_3 P_s P_t}{N_c^2} \left| \sum_{i=1}^{N_s} \sum_{n=\frac{N_c}{N_s}(i-1)+1}^{\frac{N_c}{N_s} i} c_n s_i \right|^2 \left\| \mathbf{f}^H \mathbf{h} \right\|^2 + \gamma_2 P_t \left\| \mathbf{f}^H \mathbf{n} \right\|^2}{\frac{\gamma_1 \gamma_2 P_s |g|^2}{N_s^2} \left| \sum_{i=1}^{N_s} s_i^* \right|^2 \|\mathbf{f}\|^2 + \frac{\gamma_3 P_s}{N_c^2} \left| \sum_{i=1}^{N_s} \sum_{n=\frac{N_c}{N_s}(i-1)+1}^{\frac{N_c}{N_s} i} c_n s_i^* \right|^2 \|\mathbf{h}\|^2 + \|\mathbf{n}\|^2} \right). \tag{A.5}$$

Let

$$\mu = \left| \sum_{i=1}^{N_s} s_i \right|^2 = \left| \sum_{i=1}^{N_s} s_i^* \right|^2,$$
$$\nu = \left| \sum_{i=1}^{N_s} \sum_{n=\frac{N_c}{N_s}(i-1)}^{\frac{N_c}{N_s} i-1} c_n s_i^* \right|^2 = \left| \sum_{i=1}^{N_s} \sum_{n=\frac{N_c}{N_s}(i-1)}^{\frac{N_c}{N_s} i-1} c_n s_i \right|^2. \tag{A.6}$$

Asymptotic massive MIMO expressions for Rayleigh fading channels have been presented in [136]. Following a similar procedure for Nakagami-m fading channels, we can show that $\frac{1}{M}\|\mathbf{f}_i\|^4 \rightarrow M + \frac{1}{m_f}$, $\frac{1}{M}\|\mathbf{f}_i\|^2 \rightarrow 1$, $\frac{1}{M}\left\|{\mathbf{f}_k}^H \mathbf{f}_i\right\|^2 \rightarrow 1$, $\frac{1}{M}{\mathbf{f}_k}^H \mathbf{f}_i \rightarrow 0$ (for $k \neq i$), $\frac{1}{M}{\mathbf{f}_k}^H \widetilde{\mathbf{n}} \rightarrow 0$, $\frac{1}{M}\left\|{\mathbf{f}_i}^H \widetilde{\mathbf{n}}\right\|^2 \rightarrow \frac{{\sigma_n}^2}{NT_c}$ and $\frac{1}{M}\|\widetilde{\mathbf{n}}\|^2 \rightarrow \frac{{\sigma_n}^2}{NT_c}$. Note that only the expression for $\|\mathbf{f}_i\|^4$ is different for Nakagami-m channels as compared to Rayleigh fading, while the others remain the same. Also, only m_f appears in the expression and m_g and m_h do not impact the results. Substituting these asymptotic results in (A.5) gives us the result in (2.14) for $N_s \leq N_c$ and is reproduced below

$$Q \approx \gamma_2 P_t \left(\frac{\gamma_1 \gamma_2 |g|^2 \mu \left(M + \frac{1}{m_f} \right) + \gamma_3 \nu \left(\frac{N_s}{N_c} \right)^2 + \frac{\sigma_n^2 N_s}{T_s P_s}}{\gamma_1 \gamma_2 |g|^2 \mu + \gamma_3 \nu \left(\frac{N_s}{N_c} \right)^2 + \frac{\sigma_n^2 N_s}{T_s P_s}} \right).$$

When $N_s = N_c$, (2.14) simplifies to

$$Q \approx \gamma_2 P_t \left(\frac{\gamma_1 \gamma_2 |g|^2 \mu \left(M + \frac{1}{m_f} \right) + \gamma_3 \nu + \frac{\sigma_n^2 N_s}{T_s P_s}}{\gamma_1 \gamma_2 |g|^2 \mu + \gamma_3 \nu + \frac{\sigma_n^2 N_s}{T_s P_s}} \right).$$

Case 2: $N_s \geq N_c$ In this case, $T_s < T_c$. Substituting (2.1) in (2.8), we have

$$\mathbf{x}_s = \frac{\sqrt{\gamma_1 \gamma_2 P_s} g^* \mathbf{f}^*}{N_c T_c} \int_0^{N_c T_c} \sum_{n=1}^{N_c} c_n^2 {p_c}^2 (t - nT_c) \sum_{i=1}^{N_s} s_i p_s (t - iT_s) dt, \tag{A.7a}$$

$$= \sqrt{\gamma_1\gamma_2 P_s}\frac{g^*\mathbf{f}^*}{N_cT_c}\sum_{n=1}^{N_c}\sum_{i=\frac{N_s}{N_c}(n-1)}^{\frac{N_s}{N_c}n-1} s_i \int_{iT_s}^{(i+1)T_s} p_s(t-iT_s)dt, \tag{A.7b}$$

$$= \sqrt{\gamma_1\gamma_2 P_s}\frac{g^*\mathbf{f}^*}{N_cT_c}\sum_{n=1}^{N_c}\sum_{i=\frac{N_s}{N_c}(n-1)}^{\frac{N_s}{N_c}n-1} s_iT_s, \tag{A.7c}$$

$$= \sqrt{\gamma_1\gamma_2 P_s}\frac{g^*\mathbf{f}^*}{N_s}\sum_{i=1}^{N_s} s_i, \tag{A.7d}$$

where the (A.7c) comes from the fact that $\int_{iT_s}^{(i+1)T_s} p_s(t-iT_s)dt = T_s$ and (A.7d) is obtained using $N_cT_c = N_sT_s$. Substituting (2.1) in (2.9), we obtain

$$\mathbf{x}_i = \frac{\sqrt{\gamma_3 P_s}\mathbf{h}^H}{N_cT_c}\int_0^{N_cT_c}\sum_{i=1}^{N_s} s_ip_s(t-iT_s)\sum_{n=1}^{N_c} c_np_c(t-nT_c)dt, \tag{A.8a}$$

$$= \sqrt{\gamma_3 P_s}\frac{\mathbf{h}^H}{N_cT_c}\sum_{n=1}^{N_c}\sum_{i=\frac{N_s}{N_c}(n-1)}^{\frac{N_s}{N_c}n-1} c_ns_i\int_{iT_s}^{(i+1)T_s} p_s(t-iT_s)dt, \tag{A.8b}$$

$$\mathbf{x}_i = \sqrt{\gamma_3 P_s}\frac{\mathbf{h}^H}{N_cT_c}\sum_{n=1}^{N_c}\sum_{i=\frac{N_s}{N_c}(n-1)}^{\frac{N_s}{N_c}n-1} c_ns_iT_s, \tag{A.8c}$$

$$= \sqrt{\gamma_3 P_s}\frac{\mathbf{h}^H}{N_s}\sum_{n=1}^{N_c}\sum_{i=\frac{N_s}{N_c}(n-1)}^{\frac{N_s}{N_c}n-1} c_ns_i, \tag{A.8d}$$

where (A.8c) and (A.8d) follow from the same reasoning as in (A.7c) and (A.7d).

Substituting (A.7d) and (A.8d) into (2.11), we get:

$$r_{\mathrm{ER}} = \sqrt{\gamma_2 P_t}\frac{\left(\frac{\sqrt{\gamma_1\gamma_2 P_s}g}{N_s}\sum_{i=1}^{N_s} s_i\mathbf{f}^H\mathbf{f} + \frac{\sqrt{\gamma_3 P_s}}{N_s}\sum_{n=1}^{N_c}\sum_{i=\frac{N_s}{N_c}(n-1)+1}^{\frac{N_s}{N_c}n} c_ns_i\mathbf{f}^H\mathbf{h} + \mathbf{f}^H\mathbf{n}\right)}{\left\|\frac{\sqrt{\gamma_1\gamma_2 P_s}g^*}{N_s}\sum_{i=1}^{N_s} s_i^*\mathbf{f} + \frac{\sqrt{\gamma_3 P_s}}{N_s}\sum_{n=1}^{N_c}\sum_{i=\frac{N_s}{N_c}(n-1)+1}^{\frac{N_s}{N_c}n} c_ns_i^*\mathbf{h} + \mathbf{n}\right\|}, \tag{A.9}$$

from which the incident RF power can be found as:

$$Q_{RF} = |r_{\mathrm{ER}}|^2 \tag{A.10}$$

$$\approx \left(\frac{\frac{\gamma_1 {\gamma_2}^2 P_s P_t |g|^2}{N_s^2} \left| \sum_{i=1}^{N_s} s_i \right|^2 \|\mathbf{f}\|^4 + \frac{\gamma_3 P_s P_t}{N_s^2} \left| \sum_{n=1}^{N_c} \sum_{i=\frac{N_s}{N_c}(n-1)+1}^{\frac{N_s}{N_c}n} c_n s_i \right|^2 \left\| \mathbf{f}^H \mathbf{h} \right\|^2 + \gamma_2 P_t \left\| \mathbf{f}^H \mathbf{n} \right\|^2}{\frac{\gamma_1 \gamma_2 P_s |g|^2}{N_s^2} \left| \sum_{i=1}^{N_s} s_i^* \right|^2 \|\mathbf{f}\|^2 + \gamma_3 P_s \frac{1}{N_s^2} \left| \sum_{n=1}^{N_c} \sum_{i=\frac{N_s}{N_c}(n-1)+1}^{\frac{N_s}{N_c}n} c_n s_i^* \right|^2 \|\mathbf{h}\|^2 + \|\mathbf{n}\|^2} \right). \tag{A.11}$$

(A.10) when simplified using the asymptotic massive MIMO expressions [136], gives the result for $N_s \geq N_c$ in (2.14), reproduced below:

$$Q \approx \gamma_2 P_t \left(\frac{\gamma_1 \gamma_2 |g|^2 \mu \left(M + \frac{1}{m_f} \right) + \gamma_3 \nu + \frac{\sigma_n^2 N_s}{T_s P_s}}{\gamma_1 \gamma_2 |g|^2 \mu + \gamma_3 \nu + \frac{\sigma_n^2 N_s}{T_s P_s}} \right), \tag{A.12}$$

where μ and ν are as defined in (A.6).

Bibliography

[1] N. Van Huynh, D. T. Hoang, X. Lu, D. Niyato, P. Wang, and D. I. Kim, "Ambient backscatter communications: A contemporary survey," *IEEE Commun. Surveys Tuts.*, vol. 20, no. 4, pp. 2889–2922, May 2018.

[2] Q. Wu and R. Zhang, "Towards smart and reconfigurable environment: Intelligent Reflecting Surface aided Wireless Network," *IEEE Commun. Mag.*, vol. 58, no. 1, pp. 106–112, Jan. 2020.

[3] D. Nguyen, M. Ding, P. Pathirana, A. Seneviratne, J. Li, D. Niyato, O. Dobre, and H. Poor, "6G Internet of Things: A Comprehensive Survey," *IEEE Internet Things J.*, vol. 9, no. 1, pp. 359–383, Jan. 2022.

[4] A. Al-Fuqaha, M. Guizani, M. Mohammadi, M. Aledhari, and M. Ayyash, "Internet of things: A survey on enabling technologies, protocols, and applications," *IEEE Commun. Surveys Tuts.*, vol. 17, no. 4, pp. 2347–2376, June 2015.

[5] X. You, C.-X. Wang, J. Huang, X. Gao, Z. Zhang, M. Wang, Y. Huang, C. Zhang, Y. Jiang, J. Wang *et al.*, "Towards 6G wireless communication networks: Vision, enabling technologies, and new paradigm shifts," *Science China Information Sciences*, vol. 64, pp. 1–74, 2021.

[6] S. J. Nawaz, S. K. Sharma, B. Mansoor, M. N. Patwary, and N. M. Khan, "Non-coherent and backscatter communications: Enabling ultra-massive connectivity in 6g wireless networks," *IEEE Access*, vol. 9, pp. 38 144–38 186, 2021.

[7] S. Ali, W. Saad, N. Rajatheva, K. Chang, D. Steinbach, B. Sliwa, C. Wietfeld, K. Mei, H. Shiri *et al.*, "6G White Paper on Machine Learning in Wireless Communication Networks," *CoRR*, vol. abs/2004.13875, 2020. [Online]. Available: https://arxiv.org/abs/2004.13875

[8] V. Liu, A. Parks, V. Talla, S. Gollakota, D. Wetherall, and J. R. Smith, "Ambient backscatter: wireless communication out of thin air," in *Proc. ACM SIGCOMM*, vol. 43, no. 4, Aug. 2013, pp. 39–50.

[9] J. Qian, F. Gao, G. Wang, S. Jin, and H. Zhu, "Noncoherent Detections for Ambient Backscatter System," *IEEE Trans. Wireless Commun.*, vol. 16, no. 3, pp. 1412–1422, Mar. 2017.

[10] M. Di Renzo, A. Zappone, M. Debbah, M.-S. Alouini, C. Yuen, J. de Rosny, and S. Tretyakov, "Smart Radio Environments Empowered by Reconfigurable Intelligent Surfaces: How It works, State of Research, and the Road Ahead," *IEEE J. Sel. Areas Commun.*, vol. 38, no. 11, pp. 2450–2525, July 2020.

[11] S. Gong, X. Lu, D. T. Hoang, D. Niyato, L. Shu, D. I. Kim, and Y.-C. Liang, "Toward Smart Wireless Communications via Intelligent Reflecting Surfaces: A Contemporary Survey," *IEEE Commun. Surv. Tutor.*, vol. 22, no. 4, pp. 2283–2314, June 2020.

[12] M. A. ElMossallamy, H. Zhang, L. Song, K. G. Seddik, Z. Han, and G. Y. Li, "Reconfigurable intelligent surfaces for wireless communications: Principles, challenges, and opportunities," *IEEE Trans. Cog. Commun. Netw.*, vol. 6, no. 3, pp. 990–1002, Sept. 2020.

[13] Y. Liu, X. Liu, X. Mu, T. Hou, J. Xu, M. Di Renzo, and N. Al-Dhahir, "Reconfigurable intelligent surfaces: Principles and opportunities," *IEEE Commun. Surveys Tuts.*, vol. 23, no. 3, pp. 1546–1577, May 2021.

[14] Q. Wu, S. Zhang, B. Zheng, C. You, and R. Zhang, "Intelligent Reflecting Surface Aided Wireless Communications: A Tutorial," *IEEE Trans. Commun.*, pp. 1–1, Jan. 2021.

[15] O. Özdogan, E. Björnson, and E. G. Larsson, "Intelligent Reflecting Surfaces: Physics, Propagation, and Pathloss Modeling," *IEEE Wireless Commun. Lett.*, vol. 9, no. 5, pp. 581–585, May 2020.

[16] R. Alghamdi, R. Alhadrami, D. Alhothali, H. Almorad, A. Faisal, S. Helal, R. Shalabi, R. Asfour, N. Hammad, A. Shams, N. Saeed, H. Dahrouj, T. Y. Al-Naffouri, and M.-S. Alouini, "Intelligent surfaces for 6g wireless networks: A survey of optimization and performance analysis techniques," *IEEE Access*, vol. 8, pp. 202 795–202 818, 2020.

[17] A. N. Parks, A. Liu, S. Gollakota, and J. R. Smith, "Turbocharging ambient backscatter communication," in *Proc. ACM SIGCOMM*, vol. 44, no. 4, Aug. 2015, pp. 619–630.

[18] J. Kimionis, A. Bletsas, and J. N. Sahalos, "Increased range bistatic scatter radio," *IEEE Trans. Commun.*, vol. 62, no. 3, pp. 1091–1104, Mar. 2014.

[19] A. Wang, V. Iyer, V. Talla, J. R. Smith, and S. Gollakota, "FM Backscatter: Enabling connected cities and smart fabrics," in *14th USENIX Symposium on Networked Systems Design and Implementation (NSDI 17)*, 2017, pp. 243–258.

[20] V. Talla, M. Hessar, B. Kellogg, A. Najafi, J. R. Smith, and S. Gollakota, "Lora backscatter: Enabling the vision of ubiquitous connectivity," *Proceedings of the ACM on interactive, mobile, wearable and ubiquitous technologies*, vol. 1, no. 3, pp. 1–24, 2017.

[21] D. Bharadia, K. R. Joshi, M. Kotaru, and S. Katti, "BackFi: High throughput Wi-Fi backscatter," *ACM SIGCOMM Comput. Commun. Review*, vol. 45, no. 4, pp. 283–296, Aug. 2015.

[22] B. Kellogg, V. Talla, S. Gollakota, and J. R. Smith, "Passive WI-FI: Bringing low power to wi-fi transmissions," in *Proc. 13th Symp. Netw. Syst. Design Implementation*, Mar. 2016, pp. 151–164.

[23] P. Zhang, C. Josephson, D. Bharadia, and S. Katti, "Freerider: Backscatter communication using commodity radios," in *Proceedings of the 13th Int. Conf. on emerging Netw. Expt. and Tech.*, 2017, pp. 389–401.

[24] C. Mikeka, H. Arai *et al.*, "Design issues in radio frequency energy harvesting system," *Sustainable Energy Harvesting Technologies-Past, Present and Future*, pp. 235–256, 2011.

[25] V. Talla, B. Kellogg, S. Gollakota, and J. R. Smith, "Battery-free cellphone," *Proceedings of the ACM on Interactive, Mobile, Wearable and Ubiquitous Technologies*, vol. 1, no. 2, pp. 1–20, 2017.

[26] X. Wang, Z. Su, and G. Wang, "Relay selection for secure backscatter wireless communications," *Electronics Letters*, vol. 51, no. 12, pp. 951–952, 2015.

[27] W. Saad, X. Zhou, Z. Han, and H. V. Poor, "On the Physical Layer Security of Backscatter Wireless Systems," *IEEE Trans. Wireless Commun.*, vol. 13, no. 6, pp. 3442–3451, June 2014.

[28] Y. Liu, M. Dong, K. Ota, and A. Liu, "Activetrust: Secure and Trustable Routing in Wireless Sensor Networks," *IEEE Trans. Inf. Forensics Security*, vol. 11, no. 9, pp. 2013–2027, Sept. 2016.

[29] D. N. K. Jayakody, J. Thompson, S. Chatzinotas, and S. Durrani, *Wireless Information and Power Transfer: A New Paradigm for Green Communications*. Springer, 2017.

[30] K. Huang and X. Zhou, "Cutting the last wires for mobile communications by microwave power transfer," *IEEE Commun. Mag.*, vol. 53, no. 6, pp. 86–93, 2015.

[31] S. Bi, C. K. Ho, and R. Zhang, "Wireless powered communication: opportunities and challenges," *IEEE Commun. Mag.*, vol. 53, no. 4, pp. 117–125, Apr. 2015.

[32] Y. Zeng, B. Clerckx, and R. Zhang, "Communications and signals design for wireless power transmission," *IEEE Trans. Commun.*, vol. 65, no. 5, pp. 2264–2290, May 2017.

[33] L. Yang, Y. Zeng, and R. Zhang, "Wireless power transfer with hybrid beamforming: How many RF chains do we need?" *IEEE Trans. Wireless Commun.*, vol. 17, no. 10, pp. 6972–6984, Oct. 2018.

[34] Y. Alsaba, S. K. A. Rahim, and C. Y. Leow, "Beamforming in wireless energy harvesting communications systems: A survey," *IEEE Commun. Survey Tuts.*, vol. 20, no. 2, pp. 1329–1360, Jan. 2018.

[35] L. Liu, R. Zhang, and K. Chua, "Multi-antenna wireless powered communication with energy beamforming," *IEEE Trans. Commun.*, vol. 62, no. 12, pp. 4349–4361, Dec. 2014.

[36] Y. Zeng and R. Zhang, "Optimized training design for wireless energy transfer," *IEEE Trans. Commun.*, vol. 63, no. 2, pp. 536–550, Feb. 2015.

[37] ——, "Optimized training for net energy maximization in multi-antenna wireless energy transfer over frequency-selective channel," *IEEE Trans. Commun.*, vol. 63, no. 6, pp. 2360–2373, June 2015.

[38] G. Yang, C. K. Ho, and Y. L. Guan, "Dynamic resource allocation for multiple-antenna wireless power transfer," *IEEE Trans. Signal Process.*, vol. 62, no. 14, pp. 3565–3577, July 2014.

[39] X. Chen, C. Yuen, and Z. Zhang, "Wireless energy and information transfer tradeoff for limited-feedback multiantenna systems with energy beamforming," *IEEE Trans. Veh. Technol.*, vol. 63, no. 1, pp. 407–412, Jan. 2014.

[40] H. Son and B. Clerckx, "Joint beamforming design for multi-user wireless information and power transfer," *IEEE Trans. Wireless Commun.*, vol. 13, no. 11, pp. 6397–6409, Nov. 2014.

[41] J. Park and B. Clerckx, "Joint wireless information and energy transfer with reduced feedback in MIMO interference channels," *IEEE J. Sel. Areas Commun.*, vol. 33, no. 8, pp. 1563–1577, Aug. 2015.

[42] J. Xu and R. Zhang, "Energy beamforming with one-bit feedback," *IEEE Trans. Signal Process.*, vol. 62, no. 20, pp. 5370–5381, Oct. 2014.

[43] Y. Zeng and R. Zhang, "Optimized training design for wireless energy transfer," *IEEE Trans. Commun.*, vol. 63, no. 2, pp. 536–550, Feb. 2015.

[44] A. Massa, G. Oliveri, F. Viani, and P. Rocca, "Array designs for long-distance wireless power transmission: State-of-the-art and innovative solutions," *Proc. IEEE*, vol. 101, no. 6, pp. 1464–1481, Jun. 2013.

[45] E. Sharp and M. Diab, "Van atta reflector array," *IRE Transactions on Antennas and Propagation*, vol. 8, no. 4, pp. 436–438, Jul. 1960.

[46] C. Pon, "Retrodirective array using the heterodyne technique," *IEEE Trans. Antennas Propag.*, vol. 12, no. 2, pp. 176–180, Mar. 1964.

[47] Y. Li and V. Jandhyala, "Design of retrodirective antenna arrays for short-range wireless power transmission," *IEEE Trans. Antennas Propag.*, vol. 60, no. 1, pp. 206–211, Jan. 2012.

[48] C. T. Rodenbeck, Ming-yi Li, and Kai Chang, "A phased-array architecture for retrodirective microwave power transmission from the space solar power satellite," in *Proc. IEEE MTT*, vol. 3, Jun. 2004, pp. 1679–1682.

[49] L. H. Hsieh, B. H. Strassner, S. J. Kokel, C. T. Rodenbeck, M. Y. Li, K. Chang, F. E. Little, G. D. Arndt, and P. H. Ngo, "Development of a retrodirective wireless microwave power transmission system," in *Proc. IEEE APS*, vol. 2, Jun. 2003, pp. 393–396 vol.2.

[50] C. T. Rodenbeck and K. Chang, "A limitation on the small-scale demonstration of retrodirective microwave power transmission from the solar power satellite," *IEEE Antennas Propag. Mag.*, vol. 47, no. 4, pp. 67–72, Aug. 2005.

[51] S. Lee, Y. Zeng, and R. Zhang, "Retrodirective multi-user wireless power transfer with massive mimo," *IEEE Wireless Commun. Letters*, vol. 7, no. 1, pp. 54–57, Feb. 2018.

[52] G. Yang, C. K. Ho, and Y. L. Guan, "Multi-antenna wireless energy transfer for backscatter communication systems," *IEEE J. Sel. Areas Commun.*, vol. 33, no. 12, pp. 2974–2987, Dec. 2015.

[53] I. Krikidis, "Retrodirective large antenna energy beamforming in backscatter multi-user networks," *IEEE Wireless Commun. Lett.*, vol. 7, no. 4, pp. 678–681, Feb. 2018.

[54] J. K. Devineni and H. S. Dhillon, "Ambient backscatter systems: Exact average bit error rate under fading channels," *IEEE Trans. Green Commun. Netw.*, vol. 3, no. 1, pp. 11–25, Mar. 2019.

[55] G. Wang, F. Gao, R. Fan, and C. Tellambura, "Ambient Backscatter Communication Systems: Detection and Performance Analysis," *IEEE Trans. Commun.*, vol. 64, no. 11, pp. 4836–4846, Nov. 2016.

[56] J. K. Devineni and H. S. Dhillon, "Non-coherent Detection and Bit Error Rate for an Ambient Backscatter Link in Time-Selective Fading," *IEEE Trans. Commun.*, vol. 69, no. 1, pp. 602–618, Oct. 2021.

[57] G. Yang, Y. Liang, R. Zhang, and Y. Pei, "Modulation in the air: Backscatter communication over ambient ofdm carrier," *IEEE Trans. Commun.*, vol. 66, no. 3, pp. 1219–1233, Mar. 2018.

[58] P. Zhang, M. Rostami, P. Hu, and D. Ganesan, "Enabling Practical Backscatter Communication for on-body Sensors," in *Proc. ACM SIGCOMM*, Aug. 2016, pp. 370–383.

[59] V. Iyer, V. Talla, B. Kellogg, S. Gollakota, and J. Smith, "Inter-technology Backscatter: Towards internet connectivity for Implanted Devices," in *Proc. ACM SIGCOMM*, Aug. 2016, pp. 356–369.

[60] "Hitchhike: Practical Backscatter using Commodity WI-FI, author=Zhang, Pengyu and Bharadia, Dinesh and Joshi, Kiran and Katti, Sachin, booktitle=Proc. ACM Conf. Embedded Netw. Sensor Syst., pages=259–271, year=2016, organization=ACM, month=Nov.,."

[61] R. Fara, D.-T. Phan-Huy, and M. D. Renzo, "Ambient Backscatter-friendly 5G Networks: Creating hot spots for tags and good spots for readers," in *2020 IEEE Wireless Commun. Netw. Conf. (WCNC)*, 2020, pp. 1–7.

[62] H. Guo, Q. Zhang, S. Xiao, and Y. Liang, "Exploiting Multiple Atennas for Cognitive Ambient Backscatter Communication," *IEEE Internet Things J.*, vol. 6, no. 1, pp. 765–775, Feb. 2019.

[63] E. Global, "Specification for RFID air interface EPC™ radio-frequency identity protocols class-1 generation-2 UHF RFID protocol for communications at 860 MHz-960 MHz," *Technical report, GS1, Tech. Rep.*, 2008.

[64] C.-C. Yen, A. E. Gutierrez, D. Veeramani, and D. van der Weide, "Radar Cross-Section Analysis of Backscattering RFID Tags," *IEEE Antennas Wireless Propag. Lett.*, vol. 6, pp. 279–281, 2007.

[65] G. Marrocco and S. Caizzone, "Electromagnetic models for passive tag-to-tag communications," *IEEE Transactions on Antennas and Propagation*, vol. 60, no. 11, pp. 5381–5389, 2012.

[66] J. Griffin and G. Durgin, "Complete Link Budgets for Backscatter-Radio and RFID Systems," *IEEE Antennas Propag. Mag.*, vol. 51, no. 2, pp. 11–25, 2009.

[67] A. Bletsas, S. Siachalou, and J. N. Sahalos, "Anti-collision backscatter sensor networks," *IEEE Trans. Wireless Commun.*, vol. 8, no. 10, pp. 5018–5029, Oct. 2009.

[68] C. Boyer and S. Roy, "— invited paper — backscatter communication and rfid: Coding, energy, and mimo analysis," *IEEE Transactions on Communications*, vol. 62, no. 3, pp. 770–785, 2014.

[69] C. He, Z. Wang, and V. Leung, "Unitary Query for the $M \times L \times N$ MIMO Backscatter RFID Channel," *IEEE Trans. Wireless Commun.*, vol. 14, no. 5, pp. 2613–2625, Jan. 2015.

[70] D. Mishra and E. G. Larsson, "Optimal channel estimation for reciprocity-based backscattering with a full-duplex MIMO reader," *IEEE Trans. Sig. Process.*, vol. 67, no. 6, pp. 1662–1677, Jan. 2019.

[71] D. Mishra and E. Larsson, "Monostatic Backscattering Detection by Multiantenna Reader," in *2019 53rd Asilomar Conf. on Sig., Sys., and Comp.*, Nov. 2019, pp. 697–701.

[72] V. Talla, J. Smith, and S. Gollakota, "Advances and Open Problems in Backscatter Networking," *GetMobile: Mobile Comp. and Comm.*, vol. 24, no. 4, p. 32–38, Mar 2021.

[73] R. Chakraborty, S. Roy, and V. Jandhyala, "Revisiting RFID Link Budgets for Technology Scaling: Range Maximization of RFID Tags," *IEEE Trans Microw. Theory Tech.*, vol. 59, no. 2, pp. 496–503, 2011.

[74] J. D. Griffin and G. D. Durgin, "Gains for RF tags using multiple antennas," *IEEE Trans. Antennas Propag.*, vol. 56, no. 2, pp. 563–570, Feb. 2008.

[75] P. Wang, J. Fang, X. Yuan, Z. Chen, and H. Li, "Intelligent Reflecting Surface-Assisted Millimeter Wave Communications: Joint Active and Passive Precoding Design," *IEEE Trans. Veh. Tech.*, vol. 69, no. 12, pp. 14 960–14 973, Oct. 2020.

[76] Z. Chen, X. Ma, C. Han, and Q. Wen, "Towards Intelligent Reflecting Surface empowered 6G terahertz Communications: A Survey," *China Commun.*, vol. 18, no. 5, pp. 93–119, 2021.

[77] H. Lu, Y. Zeng, S. Jin, and R. Zhang, "Aerial intelligent reflecting surface: Joint placement and passive beamforming design with 3d beam flattening," *IEEE Trans. Wireless Commun.*, pp. 1–1, 2021.

[78] F. Zhou, C. You, and R. Zhang, "Delay-optimal scheduling for irs-aided mobile edge computing," *IEEE Wireless Commun. Lett.*, vol. 10, no. 4, pp. 740–744, 2021.

[79] S. Basharat, S. Hassan, A. Mahmood, Z. Ding, and M. Gidlund, "Reconfigurable Intelligent Surface-Assisted Backscatter Communication: A New Frontier for Enabling 6G IoT Networks," *IEEE Wireless Commun.*, pp. 1–8, 2022.

[80] W. Zhao, G. Wang, S. Atapattu, T. A. Tsiftsis, and X. Ma, "Performance analysis of large intelligent surface aided backscatter communication systems," *IEEE Wireless Commun. Lett.*, vol. 9, no. 7, pp. 962–966, 2020.

[81] S. Abeywickrama, C. You, R. Zhang, and C. Yuen, "Channel Estimation for Iintelligent Reflecting Surface Assisted Backscatter Communication," *IEEE Wireless Commun. Lett.*, pp. 1–1, Aug. 2021.

[82] X. Jia, X. Zhou, D. Niyato, and J. Zhao, "Intelligent Reflecting Surface-Assisted Bistatic Backscatter networks: Joint Beamforming and Reflection Design," *IEEE Trans. Green Commun. and Netw.*, pp. 1–1, Nov. 2021.

[83] M. Nemati, J. Ding, and J. Choi, "Short-range ambient backscatter communication using reconfigurable intelligent surfaces," in *Proc. IEEE WCNC*, 2020, pp. 1–6.

[84] S. Idrees, X. Jia, S. Durrani, and X. Zhou, "Design of Intelligent Reflecting Surface (IRS)-Boosted Ambient Backscatter Systems," *IEEE Access*, vol. 10, pp. 65 000–65 010, 2022.

[85] Y.-C. Liang, Q. Zhang, E. G. Larsson, and G. Y. Li, "Symbiotic Radio: Cognitive Backscattering Communications for Future Wireless Networks," *IEEE Trans. Cogn. Commun. Netw.*, vol. 6, no. 4, pp. 1242–1255, 2020.

[86] H. Ma, H. Zhang, N. Zhang, J. Wang, N. Wang, and V. Leung, "Reconfigurable Intelligent Surface with Energy Harvesting Assisted Cooperative Ambient Backscatter Communications," *IEEE Wireless Commun. Lett.*, vol. 11, no. 6, pp. 1283–1287, Apr. 2022.

[87] P. Ramezani and A. Jamalipour, "Backscatter-Assisted Wireless Powered Communication Networks Empowered by Intelligent Reflecting Surface," *IEEE Trans. Veh. Tech.*, vol. 70, no. 11, pp. 11 908–11 922, Sept. 2021.

[88] Y. Zhao and B. Clerckx, "RIScatter: Unifying Backscatter Communication and Reconfigurable Intelligent Surface," *arXiv preprint arXiv:2212.09121*, 2023.

[89] R. Fara, P. Ratajczak, D. Phan-Huy, A. Ourir, M. Di Renzo, and J. de Rosny, "Reconfigurable Intelligent Surface-Assisted Ambient Backscatter Communications – Experimental Assessment," in *2021 IEEE Intl Conf. Commun. Workshops (ICC Workshops)*, Jun. 2021, pp. 1–7.

[90] X. Jia and X. Zhou, "IRS-Assisted Ambient Backscatter Communications Utilizing Deep Reinforcement Learning," *IEEE Wireless Commun. Lett.*, vol. PP, pp. 1–1, July 2021.

[91] S. Idrees, X. Jia, S. Khan, S. Durrani, and X. Zhou, "Deep Learning Based Passive Beamforming for IRS-Assisted Monostatic Backscatter Systems," in *Proc. IEEE Intl Conf. Acoustics, Speech and Sig. Process. (ICASSP)*, Apr. 2022, pp. 8652–8656.

[92] Q. Wu and R. Zhang, "Intelligent reflecting surface enhanced wireless network via joint active and passive beamforming," *IEEE Trans. Wireless Commun.*, vol. 18, no. 11, pp. 5394–5409, 2019.

[93] J. Gao, M. Khandaker, F. Tariq, K. Wong, and R. Khan, "Deep Neural Network Based Resource Allocation for V2X Communications," in *2019 IEEE 90th Veh. Tech. Conf. (VTC2019-Fall)*, Nov. 2019, pp. 1–5.

[94] L. Dai, R. Jiao, F. Adachi, H. Poor, and L. Hanzo, "Deep Learning for Wireless Communications: An Emerging Interdisciplinary Paradigm," *IEEE Wireless Commun.*, vol. 27, no. 4, pp. 133–139, Aug. 2020.

[95] S. Gong, J. Lin, B. Ding, D. Niyato, D. Kim, and M. Guizani, "When Optimization Meets Machine Learning: The Case of IRS-Assisted Wireless Networks," *IEEE Netw.*, vol. 36, no. 2, pp. 190–198, Apr. 2022.

[96] H. Huang, S. Guo, G. Gui, Z. Yang, J. Zhang, H. Sari, and F. Adachi, "Deep Learning for Physical-Layer 5G Wireless Techniques: Opportunities, Challenges and Solutions," *IEEE Wireless Commun.*, vol. 27, no. 1, pp. 214–222, Aug. 2020.

[97] J. Wang, W. Tang, Y. Han, S. Jin, X. Li, C. Wen, Q. Cheng, and T. Cui, "Interplay Between RIS and AI in Wireless Communications: Fundamentals, Architectures, Applications, and Open Research Problems," *IEEE J. Sel. Areas Commun.*, vol. 39, no. 8, pp. 2271–2288, Aug. 2021.

[98] A. M. Elbir and K. V. Mishra, "A Survey of Deep Learning Architectures for Intelligent Reflecting surfaces," *arXiv preprint arXiv:2009.02540*, 2022.

[99] T. Jiang, H. V. Cheng, and W. Yu, "Learning to Beamform for Intelligent Reflecting Surface with Implicit Channel Estimate," in *Proc. Glob. Commun. Conf. (GLOBECOM),*, Dec. 2020, pp. 1–6.

[100] H. Song, M. Zhang, J. Gao, and C. Zhong, "Unsupervised Learning-Based Joint Active and Passive Beamforming Design for Reconfigurable Intelligent Surfaces Aided Wireless Networks," *IEEE Commun. Lett.*, vol. 25, no. 3, pp. 892–896, Dec. 2021.

[101] J. Gao, C. Zhong, X. Chen, H. Lin, and Z. Zhang, "Unsupervised Learning for Passive Beamforming," *IEEE Commun. Lett.*, vol. 24, no. 5, pp. 1052–1056, May 2020.

[102] M. Sejan, M. Rahman, B. Shin, J. Oh, Y. You, and H. Song, "Machine Learning for Intelligent-Reflecting-Surface-based Wireless Communication towards 6G: A Review," *Sensors*, vol. 22, no. 14, 2022.

[103] K. Rachedi, D.-T. Phan-Huy, N. Selmene, A. Ourir, M. Gautier, A. Gati, A. Galindo-Serrano, R. Fara, and J. de Rosny, "Demo abstract: Real-time ambient backscatter demonstration," in *IEEE INFOCOM 2019 - IEEE Conf. Comp. Commun. Workshops (INFOCOM WKSHPS)*, 2019, pp. 987–988.

[104] C. He, S. Chen, H. Luan, X. Chen, and Z. J. Wang, "Monostatic MIMO Backscatter Communications," *IEEE J. Sel. Areas Commun.*, vol. 38, no. 8, pp. 1896–1909, Aug. 2020.

[105] S. Idrees, X. Zhou, S. Durrani, and D. Niyato, "Design of Ambient Backscatter Training for Wireless Power Transfer," *IEEE Trans. Wireless Commun.*, vol. 19, no. 10, pp. 6316–6330, 2020.

[106] ——, "Ambient backscatter training for retrodirective wireless power transfer," in *Proc. IEEE ICC 2020, Dublin, Ireland*.

[107] Q. Wu and R. Zhang, "Intelligent Reflecting Surface Enhanced Wireless Network via Joint Active and Passive Beamforming," *IEEE Trans. Wireless Commun.*, vol. 18, no. 11, pp. 5394–5409, 2019.

[108] S. Idrees, S. Durrani, Z. Xu, X. Jia, and X. Zhou, "Joint Active and Passive Beamforming for IRS-assisted Monostatic Backscatter Systems: An Unsupervised Learning Approach," *submitted to IEEE Trans. Mach. Learn. Commun.*, 2023.

[109] Q. Tao, C. Zhong, H. Lin, and Z. Zhang, "Symbol detection of ambient backscatter systems with manchester coding," *IEEE Trans. Wireless Commun.*, vol. 17, no. 6, pp. 4028–4038, Jun. 2018.

[110] A. Goldsmith, *Wireless Communications*. Cambridge University Press, 2005.

[111] P. N. Alevizos, G. Vougioukas, and A. Bletsas, "Nonlinear energy harvesting models in wireless information and power transfer," in *Proc. IEEE SPAWC*, Jun. 2018, pp. 1–5.

[112] E. Boshkovska, D. W. K. Ng, N. Zlatanov, A. Koelpin, and R. Schober, "Robust resource allocation for MIMO wireless powered communication networks based on a non-linear eh model," *IEEE Trans. Commun.*, vol. 65, no. 5, pp. 1984–1999, May. 2017.

[113] B. Clerckx, R. Zhang, R. Schober, D. W. K. Ng, D. I. Kim, and H. V. Poor, "Fundamentals of wireless information and power transfer: From RF energy harvester models to signal and system designs," *IEEE J. Sel. Areas in Commun.*, vol. 37, no. 1, pp. 4–33, Jan. 2019.

[114] B. Zheng, C. You, W. Mei, and R. Zhang, "A survey on channel estimation and practical passive beamforming design for intelligent reflecting surface aided wireless communications," *IEEE Commun. Surveys Tuts.*, pp. 1–1, 2022.

[115] D. M. Dobkin, *The RF in RFID: UHF RFID in practice*. Newnes, 2012.

[116] Y. Zhang, F. Gao, L. Fan, X. Lei, and G. K. Karagiannidis, "Backscatter Communications Over Correlated Nakagami- m Fading Channels," *IEEE Trans. on Commun.*, vol. 67, no. 2, pp. 1693–1704, Feb. 2019.

[117] M. Simon and M. Alouini, "Digital communication over fading channels: a unified approach to performance analysis john wiley and sons," *New York, NY, USA: Wiley*, 2000.

[118] X. Lu, H. Jiang, D. Niyato, D. I. Kim, and Z. Han, "Wireless-powered device-to-device communications with ambient backscattering: Performance modeling and analysis," *IEEE Trans. Wireless Commun.*, vol. 17, no. 3, pp. 1528–1544, 2018.

[119] M. Vestakis, P. N. Alevizos, G. Vougioukas, and A. Bletsas, "Multistatic narrowband localization in backscatter sensor networks," in *Proc. Int. Workshop Signal Process. Advances Wireless Commun. (SPAWC)*, Apr. 2018, pp. 1–5.

[120] Y. Cheng, K. H. Li, Y. Liu, K. C. Teh, and H. Vincent Poor, "Downlink and Uplink Intelligent Reflecting Surface Aided Networks: NOMA and OMA," *IEEE Trans. Wireless Commun.*, pp. 1–1, Feb. 2021.

[121] Z.-Q. Luo and S. Zhang, "A semidefinite relaxation scheme for multivariate quartic polynomial optimization with quadratic constraints," *SIAM J. Optim.*, vol. 20, no. 4, pp. 1716–1736, 2010.

[122] Y. Sun, P. Babu, and D. P. Palomar, "Majorization-Minimization Algorithms in Signal Processing, Communications, and Machine Learning," *IEEE Trans. Sig. Process.*, vol. 65, no. 3, pp. 794–816, 2017.

[123] M. Grant and S. Boyd, "CVX: MATLAB software for disciplined convex programming," 2016, available:. [Online]. Available: http://cvxr.com/cvx

[124] N. D. Sidiropoulos, T. N. Davidson, and Zhi-Quan Luo, "Transmit beamforming for physical-layer multicasting," *IEEE Trans. Sig. Process.*, vol. 54, no. 6, pp. 2239–2251, 2006.

[125] X. Yu, D. Xu, and R. Schober, "MISO Wireless Communication Systems via Intelligent Reflecting Surfaces : (invited paper)," in *2019 IEEE/CIC Intl Conf. Commun. in China (ICCC)*, 2019, pp. 735–740.

[126] C. Pan, H. Ren, K. Wang, W. Xu, M. Elkashlan, A. Nallanathan, and L. Hanzo, "Multicell MIMO Communications Relying on Intelligent Reflecting Surfaces," *IEEE Trans. Wireless Commun.*, vol. 19, no. 8, pp. 5218–5233, Aug. 2020.

[127] J. Qian, F. Gao, G. Wang, S. Jin, and H. Zhu, "Semi-Coherent Detection and Performance Analysis for Ambient Backscatter System," *IEEE Trans. Commun.*, vol. 65, no. 12, pp. 5266–5279, Aug. 2017.

[128] S. W. Ellingson, "Path Loss in Reconfigurable Intelligent Surface-Enabled Channels," in *Proc. IEEE Int. Symp. Pers. Indoor Mob. Radio Commun. (PIMRC)*, Oct. 2021, pp. 829–835.

[129] K. Hornik, M. Stinchcombe, and H. White, "Multilayer Feedforward Networks are Universal Approximators," *Neural networks*, vol. 2, no. 5, pp. 359–366, 1989.

[130] D. Tse and P. Viswanath, *Fundamentals of Wireless Communication.* Cambridge university press, 2005.

[131] I. Goodfellow, Y. Bengio, and A. Courville, *Deep Learning.* MIT press, 2016.

[132] D. McNeely-White, J. Beveridge, and B. Draper, "Inception and ResNet Features are (almost) Equivalent," *Cognitive Systems Research*, vol. 59, pp. 312–318, 2020.

[133] K. He, X. Zhang, S. Ren, and J. Sun, "Deep residual learning for image recognition," in *2016 IEEE Conf. Comp. Vision Patt. Recog. (CVPR)*, 2016, pp. 770–778.

[134] P. Alevizos, K. Tountas, and A. Bletsas, "Multistatic Scatter Radio Sensor Networks for Extended Coverage," *IEEE Trans. Wireless Commun.*, vol. 17, no. 7, pp. 4522–4535, 2018.

[135] M. Ingram, M. Demirkol, and D. Kim, "Transmit Diversity and Spatial Multiplexing for RF Links using Modulated backscatter," *Signal*, vol. 10, no. 3, pp. 1–4, Jul. 2001.

[136] Y. Lim, C. Chae, and G. Caire, "Performance Analysis of Massive MIMO for Cell-Boundary Users," *IEEE Trans. Wireless Commun.*, vol. 14, no. 12, pp. 6827–6842, Dec. 2015.